First proton capture reactions on stored radioactive ions

Dissertation
zur Erlangung des Doktorgrades
der Naturwissenschaften vorgelegt beim Fachbereich Physik

der Johann Wolfgang Goethe-Universität
in Frankfurt am Main

von
Sophia Florence Dellmann
aus Solingen

Frankfurt 2023
(D30)

Vom Fachbereich Physik der
Johann Wolfgang Goethe-Universität als Dissertation angenommen.

Dekan:	Prof. Dr. Roger Erb
Gutachter:	Prof. Dr. René Reifarth Prof. Dr. Camilla Juul Hansen
Datum der Disputation:	09.02.2024

Abstract

By combining two unique facilities at the Gesellschaft für Schwerionenforschung (GSI), the Fragment Separator (FRS) and the Experimental Storage Ring (ESR), the first direct measurement of a proton capture reaction of stored radioactive isotopes was accomplished. The combination of well-defined ion energy, an ultra-thin internal gas target, and the ability to adjust the beam energy in the storage ring enables precise, energy-differentiated measurements of the (p,γ) cross sections. The new setup provides a sensitive method for measuring (p,γ) reactions relevant for nucleosynthesis processes in supernovae, which are among the most violent explosions in the universe and are not yet well understood.

The cross sections of the ^{118}Te(p,γ) and ^{124}Xe(p,γ) reactions were measured at energies of astrophysical interest. The heavy ions were stored with energies of 6 MeV/nucleon and 7 MeV/nucleon and interacted with a hydrogen gas-jet target. The produced proton-capture products were detected with a double-sided silicon strip detector. The radiative recombination process of the fully stripped ions and electrons from the hydrogen target was used as a luminosity monitor [1]. These measurements follow a proof-of-principle experiment which was performed in 2016 to validate the method on the stable isotope ^{124}Xe [2].

Additionally, post-processing nucleosynthesis simulations within the NuGrid [3] research platform have been performed. The impact of the new experimental results on the p-process nucleosynthesis around ^{124}Xe and ^{118}Te in a core-collapse supernova was investigated. The successful measurement of the proton capture cross sections of radioactive isotopes rises the motivation to proceed with experiments in lower energy regions.

Kurzfassung

Durch die Kombination zweier außergewöhnlicher Anlagen der Gesellschaft für Schwerionenforschung (GSI), dem Fragmentseparator (FRS) und dem Experimentier-Speicherring (ESR), wurden die ersten direkten Messungen von Protoneneinfangsreaktionen an gespeicherten radioaktiven Isotopen durchgeführt. Die Kombination aus genau bekannter Ionenenergie, einem sehr dünnen Gastarget und der Möglichkeit, die Energie des Strahls im Ring zu regulieren, ermöglicht präzise, energiedifferenzierte Messungen der (p,γ) Wirkungsquerschnitte. Mit dem neuen Aufbau steht eine sensitive Methode zur Messung von (p,γ) Reaktionen zur Verfügung, die für Nukleosyntheseprozesse in Supernovae relevant sind, welche zu den gewaltigsten Explosionen im Universum gehören und noch nicht vollständig verstanden sind.

Im Rahmen dieser Arbeit wurden die Wirkungsquerschnitte der Reaktionen ^{118}Te(p,γ) und ^{124}Xe(p,γ) bei Energien von astrophysikalischem Interesse gemessen. Die schweren Ionen wurden mit Energien von 6 MeV/Nukleon und 7 MeV/Nukleon gespeichert und wechselwirkten mit einem Wasserstoff-Gasjet-Target. Die beim Protoneneinfang entstandenen Ionen wurden mit einem doppelseitigen Siliziumstreifendetektor nachgewiesen. Die nach der Rekombination der ionisierten Atome mit den Elektronen aus dem Wasserstofftarget ausgesendete Strahlung, wurde als Luminositätsmonitor verwendet [1]. Diese Messungen folgen einem im Jahr 2016 durchgeführten Proof-of-Principle-Experiment zur Validierung der Methode an dem stabilen Isotop ^{124}Xe [2].

Zusätzlich wurden post-processing Nukleosynthese Studien, innerhalb der NuGrid [3] Plattform durchgeführt. Der Einfluss der neuen experimentellen Daten auf die Nukleosynthese von ^{118}Te und ^{124}Xe in Kernkollaps Supernovae wurde untersucht. Die erfolgreiche Messung von Protoneneinfangswirkungsquerschnitten an radioaktiven Isotopen motiviert weitere Experimente in niedrigeren Energiebereichen durchzuführen.

Contents

1 Astrophysical motivation

The central question in the field of nuclear astrophysics is the origin of elements. Observational astrophysics provides important information about the abundances of elements in stars. However, especially, when trying to determine the processes that occur inside stars, it has limitations. The chemical composition on the surface of stars is accessible via observations. The products of nuclear processes in the interior of stars are usually covered by the envelope. There are only a few exceptions where observations can provide more information than surface information. At late stages of a star the freshly produced material becomes visible, because strong convection mixes the material to the surface, or the envelope gets lost.

To explain the nuclear processes and properties of atomic nuclei that cannot be explained by observations, nuclear astrophysics becomes necessary. Nuclear astrophysics combines astrophysics and nuclear physics, where a range of experiments and simulations are undertaken with the aim to explore the processes that affect the formation of the elements.

1.1 Nucleosynthesis

Elements are characterized by the number of protons within their atomic nuclei. The number of neutrons defines the isotopes. The study of isotopic abundance variations is important for understanding the production of elements in the universe. The formation of atomic nuclei via nuclear reactions of various kind is called nucleosynthesis. It begins with the lightest element, hydrogen and forms every element up to the heaviest.

To address the question of the origin of elements and correspondingly of their isotopes, observations of the relative abundances of isotopes in for example our solar system, are the natural first step [4]. Figure 1.1 shows the abundance of the isotopes in the solar system over their mass number A. The abundance distribution displays distinct features that hint on the involved nuclear processes. Some features of the structure can already be explained with different production mechanisms.

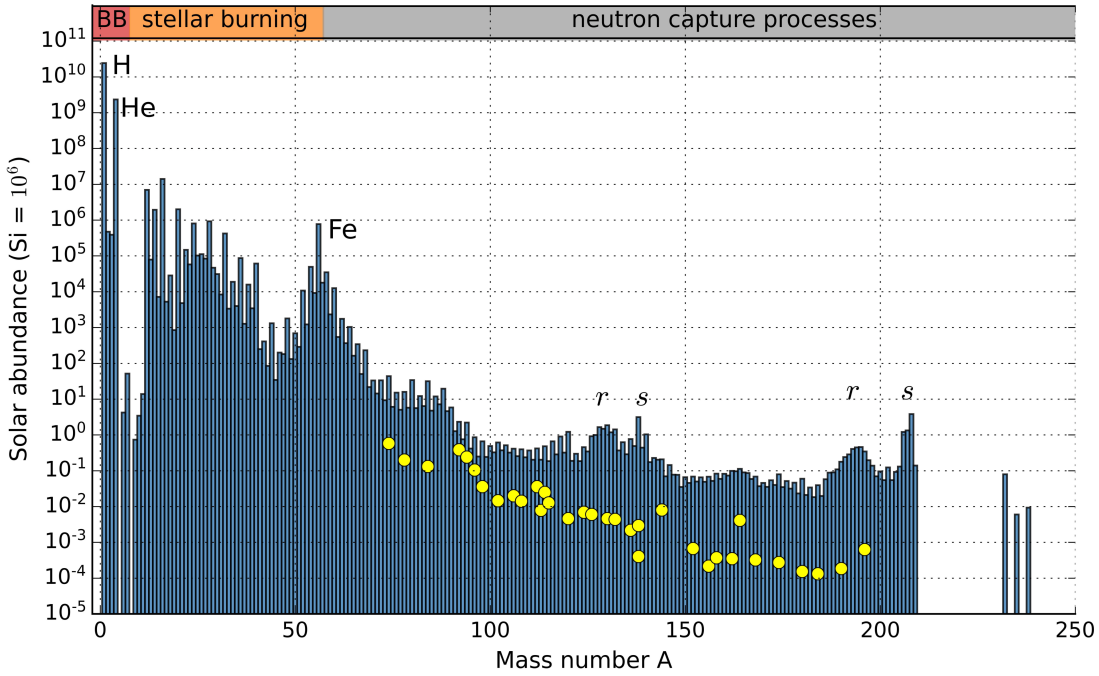

Figure 1.1: Isotopic solar abundance. The data were taken from [4]. The sum of the abundances of the stable Si isotopes has been normalized to 10^6. The slow (s) and the rapid (r) neutron-capture process peaks show a characteristic pattern in the abundance distribution. In yellow the abundances for the p-nuclei are shown. The assignment of what is a p-nuclei was taken from [5].

However, there are still many open questions. For example some abundances can not be reproduced with current models. This work aims at addressing this question for the production of the radioactive Isotope ^{118}Te.

In general, the production of the known isotopes can be attributed to a variety of mechanisms. Current understanding is based on the interplay of various processes, including stellar nucleosynthesis, which occurs in stars during their various evolutionary phases [6].

The production of the lightest elements can be explained by the primordial nucleosynthesis, followed by fusion processes in stars. In the following section this will be explained in more detail. For the elements beyond iron different mechanisms are necessary in order to produce the so-called heavy elements.

Heavy elements

Explosive events such as supernovae and neutron star mergers contribute to the synthesis of elements and isotopes under extreme conditions. They provide the necessary environment to produce elements via neutron capture [7]. These neutron capture processes produce the majority of isotopes heavier than iron. Only in explosive scenarios such as supernovae other reactions such as proton capture can play a role [8]. In the following section an overview of these various production mechanisms, starting with the formation of the lightest elements and progressing toward the origin of the heaviest ones will be given. Figure 1.1 will be the basis of the explanation, which will start from the structures of the lightest elements. The focus of the following chapter is lying on the production of the so-called p-nuclei. These p-nuclei are proton-rich isotopes, that can not be produced via neutron-induced reactions [6]. The production of the p-nuclei is the motivation of this work. Information about the production of these p-nuclei is still rare. The neutron capture processes will only be explained shortly as they can not explain the production of the p-nuclei.

In Figure 1.1 the measured solar abundances of the p-nuclei is represented by yellow data points. The data were taken from [4]. The assignment of what is a p-nuclei was taken from [5]. More information about the production processes is needed, but especially experimental data are missing. This stresses the importance of the experimental data provided with this experiment. An additional view on the production mechanisms is provided with Figure 1.2. The Figure illustrates schematically the chart of nuclides highlighting the p-nuclei and the nuclei that are mainly produced via slow (s) and rapid (r) process [5]. The p-nuclei make up only a few percentages of the abundances. The majority is produced via the neutron capture processes that will be described shortly in the following section.

1.1.1 Big Bang nucleosynthesis and production up to iron

According to our current understanding, the lightest elements are produced in the early stages of the universe. The production of hydrogen, helium, lithium and beryllium took place in around 20 minutes after the origin of the universe [9, 10] during the so-called primordial nucleosynthesis. From the first free quarks, protons and neutrons where formed that could build up the first nuclides. The simplest nuclei is hydrogen. Hydrogen, consisting of only one proton, has the highest abundance in the solar system. It has a mass fraction of 76%, visible in Figure 1.1. Afterwards the following production mechanisms took place [11]:

$$
\begin{aligned}
\mathrm{p} + \mathrm{n} &\rightarrow \mathrm{D} + \gamma \\
{}^{3}\mathrm{H} + {}^{4}\mathrm{He} &\rightarrow {}^{7}\mathrm{Li} + \gamma \\
{}^{4}\mathrm{He} + \mathrm{D} &\rightarrow {}^{6}\mathrm{Li} + \gamma \\
{}^{3}\mathrm{He} + {}^{4}\mathrm{He} &\rightarrow {}^{7}\mathrm{Be} + \gamma \\
{}^{7}\mathrm{Be} + \mathrm{n} &\rightarrow {}^{7}\mathrm{Li} + \mathrm{p}
\end{aligned}
$$

The abundance distribution from primordial nucleosynthesis has changed further since then as a result of stellar nucleosynthesis. The different burning stages of a star lead to the production of elements up to iron. The initial mass of a star is responsible for the evolution of the star. Consequently, also for the change of temperature and density in its center. These factors determine at which rate the fusion processes are possible. Up to iron the nuclei can be created by fusion. The final fusion stage is silicon burning, which produces iron.

The abundance pattern in this mass region shows a decreasing pattern. This is due to the rising Coulomb repulsion between charged nuclei towards higher Z. Thus only in stars with a mass high enough to create temperatures where the particles have enough energy to overcome the Coulomb barrier, fusion can take place. This decrease continues until the iron peak is reached. The nuclides in the region of iron are the most tightly bound isotopes nature [12]. This means that beyond iron the fusion of nuclei consumes energy instead of generating it. Generating energy is necessary for the stability of the star. If energy has to be spent, the star can no longer maintain its hydrostatic equilibrium and collapses as a supernova.

1.1.2 Neutron capture processes

Most nuclei heavier than iron are produced via neutron capture in stars of different evolutionary phases [6]. Two distinctly different processes had to be postulated in order to explain the observed abundance pattern. The slow (s) [13] and the fast (r) [14] neutron capture process, which are essentially responsible for the population of the chart of nuclei beyond iron.

s process

The first descriptions of the slow neutron capture process have already been given in 1957 by Burbidge et al. [6] and Cameron [15]. It takes place at moderate temperature and shows a path along the valley of stability. The process occurs at neutron densities of 10^7 to 10^{13} n/cm^3. In this case the β- decay is usually faster

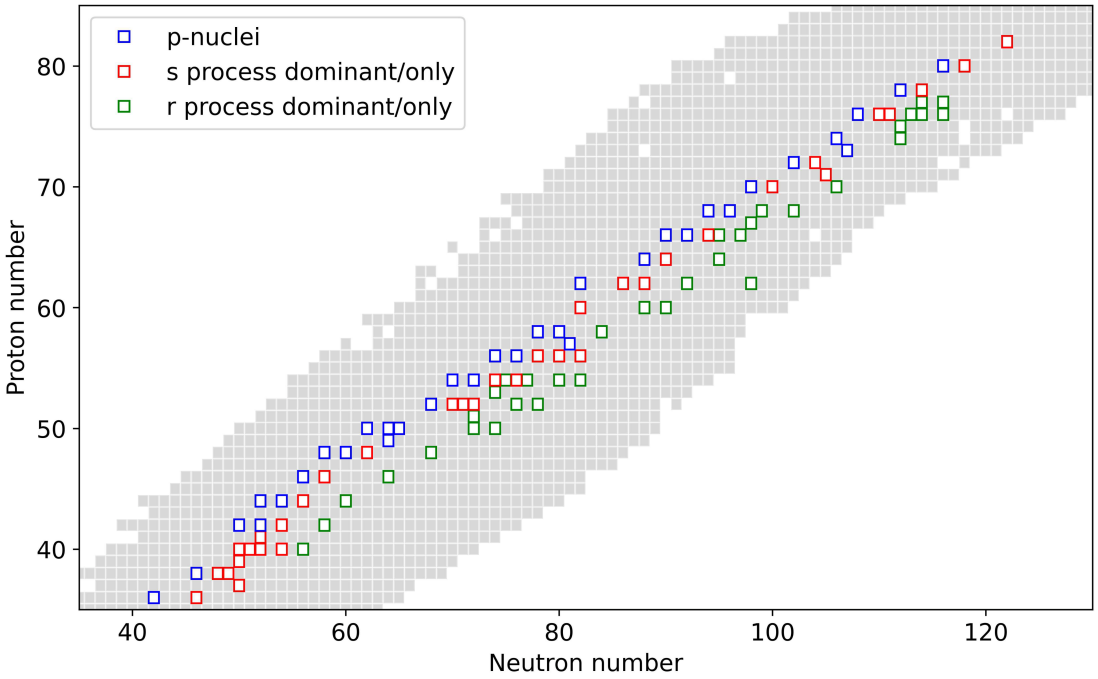

Figure 1.2: Part of the chart of nuclides. The nuclei that are highlighted are assigned to mainly one production process. In blue, the p nuclei are shown and in red and green the nuclei that are produced dominantly in the s and r process, respectively. The assignment of nuclei to the processes is taken from [5].

than the next neutron capture. The classical s process that was assumed to occur at constant temperature and neutron density is not sufficient to explain the details of the abundance distribution [16]. Currently, a distinction is made between the so-called main component, the weak component and the strong component of the s process. They differ by the seed nuclei the star already has at its formation, as well as the temperatures, neutron densities and time-integrated neutron fluxes.

r process

The rapid neutron capture process takes place at a hot explosive site, at extremely high neutron densities, for example neutron star merger. The neutron densities are about 10^{20} n/cm^3 or higher [17]. Thus, it can reach higher mass numbers on the neutron rich site of the chart of nuclides. Because the r process produces nuclei farther from the valley of stability than the s process does, it encounters

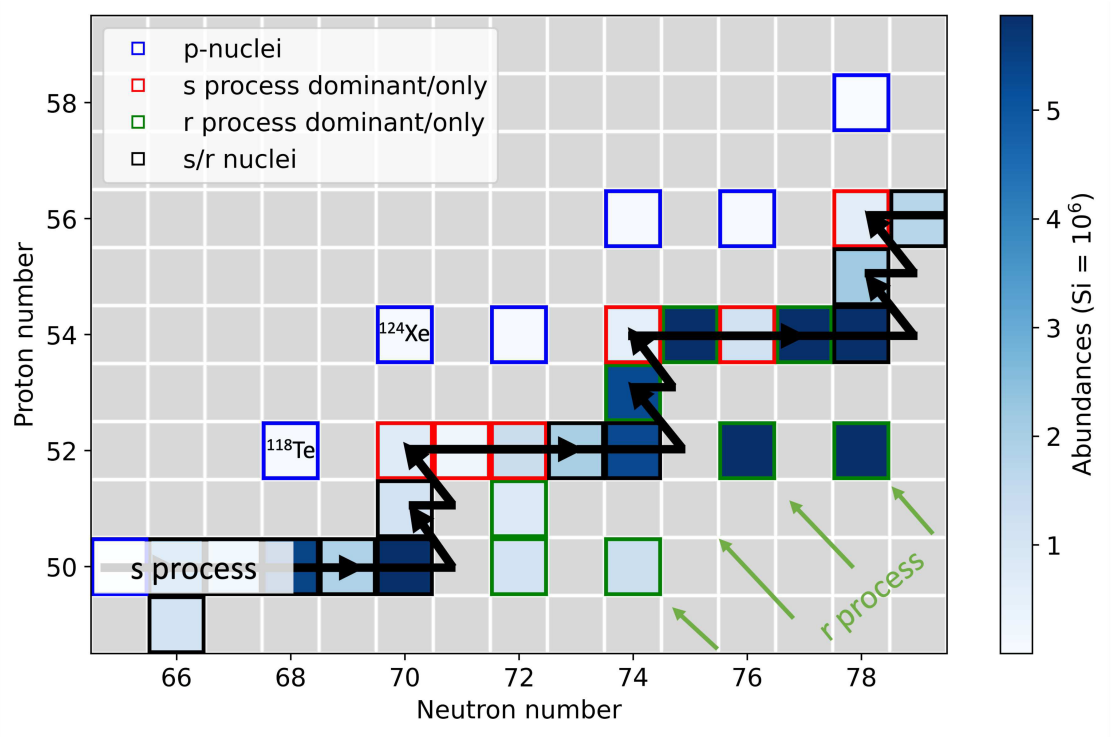

Figure 1.3: Zoom in the chart of nuclides in the region around ^{118}Te. The p-nuclei are shielded from production via neutron capture by their stable isobars.

each closed neutron shell at slightly lower mass number. Hence, the r-process abundance peaks occur at lower A. In Figure 1.1 this is labeled by s and r in the white boxes. The neutron capture processes are producing the majority of the heavy nuclei. Each of the shortly introduced processes make up almost 50% of the heavy elements. This also becomes visible when comparing the abundances shown in Figure 1.2.

1.1.3 Production of p-nuclei

There are about 35 proton-rich nuclei which cannot be produced by either the s process or the r process [6]. There are various explanations under discussions [18, 19, 20, 21], how these so-called p-nuclei are produced. These nuclei have usually low isotopic abundance. Figure 1.3 shows a zoom of the chart of nuclides in the region around ^{118}Te. In addition to the production processes, also the abundances are color coded.

This highlights visibly that p-nuclei make up only a view percentage of the abundances. The p-nuclei can not be produced via neutron captures and following β^--decays, as they are shielded by stable, neutron rich isobars. Their production has to be explained by different models.

Among the models is the γ-process [22]. Currently, this is proposed to be the main production mechanism for the heavy p-nuclei. During the γ-process the p-nuclei are generated in sequences of photo-dissociation processes, that start at the r- and s-process nuclei in combination with β^+-decays. Examples for photo-dissociation reactions are (γ,n), (γ,p) and (γ,α) reactions.

The temperatures required for this are 2.0 to 3.5 $\cdot$ 10^9 K, suggesting explosive conditions. Additionally, also proton captures are a possible production or destruction mechanism. Proton capture reactions are especially of interest for the isotopes in the region of the proton number = 50. The photodisentegration networks underproduce for example the isotopes ^{92,94}Mo and ^{96,98}Ru [19]. Since high temperatures are required for the γ-process, the currently preferred candidates for the p process are the explosively burning O/Ne layers in type II supernovae where the needed temperatures are maintained for about 1 s at densities of $\approx$ 10^6 g/cm^3 [8].

Simulations are currently used to reproduce the nucleosynthesis in this astrophysical environments. This scenario involves several thousand nuclei connected by more than several tens of thousands of reactions. This requires correspondingly large reaction networks to describe the abundance distributions that follow from these scenarios [23]. Figure 1.4 shows a region of the network around the measured isotope ^{118}Te. Given the large number of reactions, p process studies have to rely on theoretical calculations [8, 19, 24, 21].

Thus, it is of utmost importance to base these calculations on experimental data. However, experimental data for charged particle reactions are rare. Especially cross sections in an energy region inside the Gamow window are interesting for nuclear astrophysics [19]. Measurements of this kind in the astrophysical interesting energy range are already very difficult for stable nuclei, especially for isotopes in the p process region. The cross sections at this energy region are expected to be very small and thus increase the experimental challenges. However, a particularly large number of proton capture cross sections on radioactive nuclei are relevant for the production of elements in the p process. There are no experimental data available for the cross sections on radioactive nuclei and thus the theoretical calculations suffer from large uncertainties.

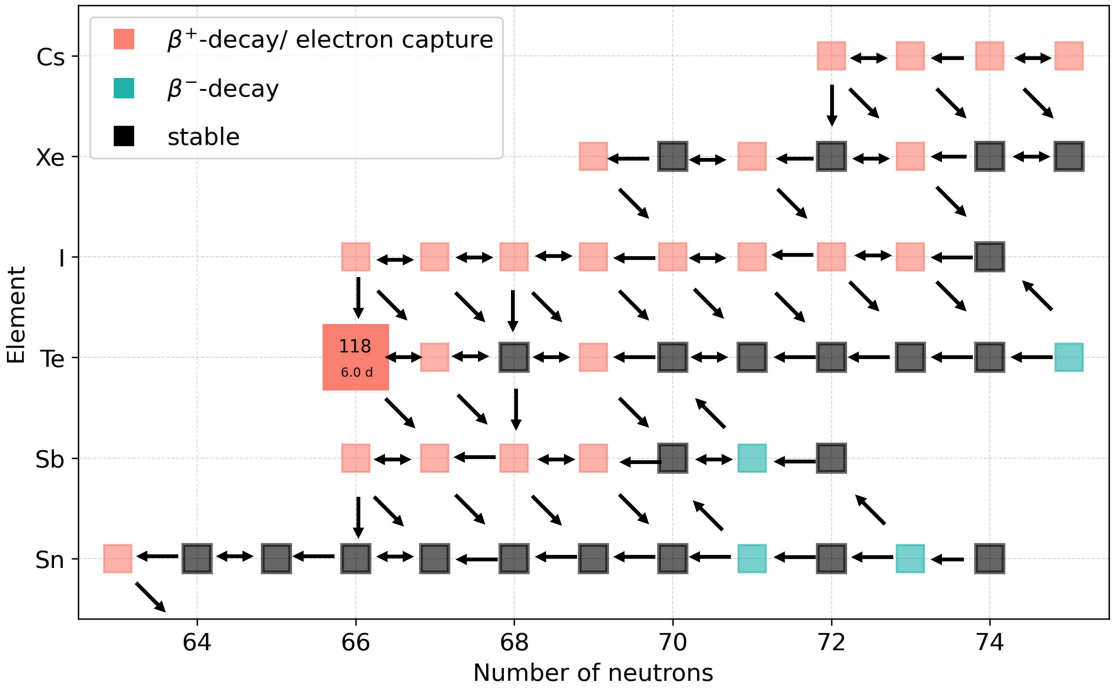

Figure 1.4: Schematic plot of a region of the reaction network around ^{118}Te. The reaction network is dominated by (γ,n) reactions and β^+-decays. Based on nucleosynthesis simulations from [8].

The ^{118}Te(p,γ) experiment improves this situation. Radioactive ^{118}Te ions were confined in a storage ring and the proton capture cross section was measured. ^{118}Te is the γ-process product of ^{119}I(γ,p).

Figure 1.5 shows the mass flow of ^{119}I, based on [24]. The sum of all production fluxes is normalized to 100%. The blue arrows visualize the production fluxes. With red arrows the destruction fluxes are shown. The destruction fluxes are scaled with the same factor, as the production fluxes. Fluxes smaller than 1% are not shown.

The main destruction path of ^{119}I is the reaction ^{119}I(γ,p). This is the time reversed reaction of ^{118}Te(p,γ), that has been measured in this experiment. Thus the ^{118}Te(p,γ) reaction rate enables constraints on the ^{119}I(γ,p) rate.

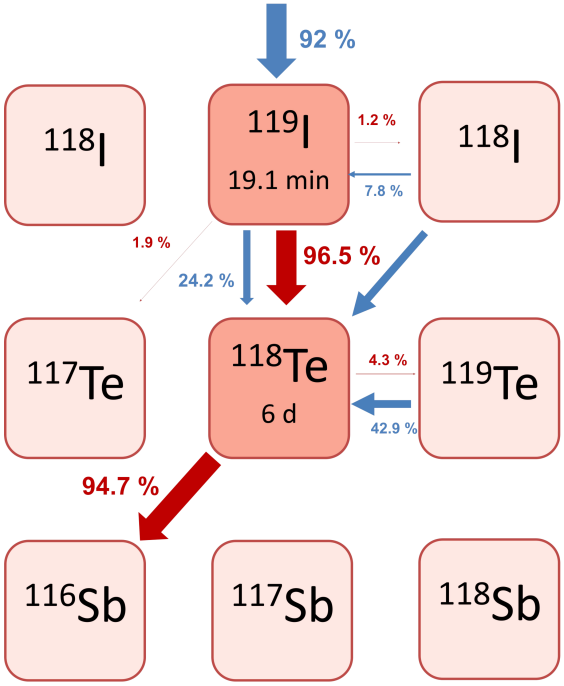

Figure 1.5: Relative time-integrated mass flow of ^{119}I, based on [24]. The blue arrows indicate the production and the red arrows the destruction fluxes.

1.2 Stellar reaction rates and cross sections

Reaction rate

The first introduced variable is the reaction rate r. The reaction rate is defined as the number of reactions per time. The particles involved in the above described scenarios only interact with a certain probability, depending on their amount, the amount of reaction partners and velocity [25].

$$r = N_x \cdot N_y \cdot v \cdot \sigma(v), \tag{1.1}$$

- N_x = Number of projectile per volume,
- N_y = Number of target nuclei per volume,
- v = relative velocity betweenN_x and N_y,
- $\sigma(v)$ = cross section.

The cross section depends on the velocity v between projectile and target. It describes reaction probability in the form of an area in which the projectile interacts

with the target. Each projectile sees this area. Thus, the total amount of reaction depends on the flux of the projectiles Φ. The flux equals the number of projectiles per time passing the area of the sample which equals $N_x v$.

Stellar reaction rate

In the astrophysical scenario, however, the cross-section depends not only on a single velocity, but on the relative velocities v, that follow a distribution function. The probability that the reaction partners are in the same velocity region (v+Δv) can be described by:

$$\int_0^\infty \Phi(v)dv = 1, \tag{1.2}$$

- $\Phi(v)$ = velocity distribution.

For the velocity distribution, a Maxwell Boltzmann distribution can be assumed. In this way, an averaged reaction rate $\langle \sigma v \rangle$ can be obtained for a pair of particles by folding the differential cross section and the distribution of the relative velocity:

$$\langle \sigma v \rangle = \int_0^\infty \sigma(v) v \Phi(v) dv. \tag{1.3}$$

Energy dependence of the cross section

The reactions that are of interest in this experiment are reactions with charged particles. Positively charged nuclei repel each other with a force that is proportional to the product of nuclear charges. They have to get close enough to each other in order to react, as they experience the strong nuclear force, when being close enough. The combination of this attracting potential and the electric repulsion is the so-called Coulomb barrier [25]. Classically the energy has to be high enough to overcome this barrier. The energies in stellar environments however give not enough energy. Only in combination with the quantum mechanical concept of tunneling through the Coulomb barrier the reaction can take place. This probability increases with increasing energy.

Gamow window

The energy dependence of the cross section and the energy distribution of the particle rates are dominating the energy dependence of nuclear reactions between charged particles [25]. Figure 1.6 shows the relative probability of the particles

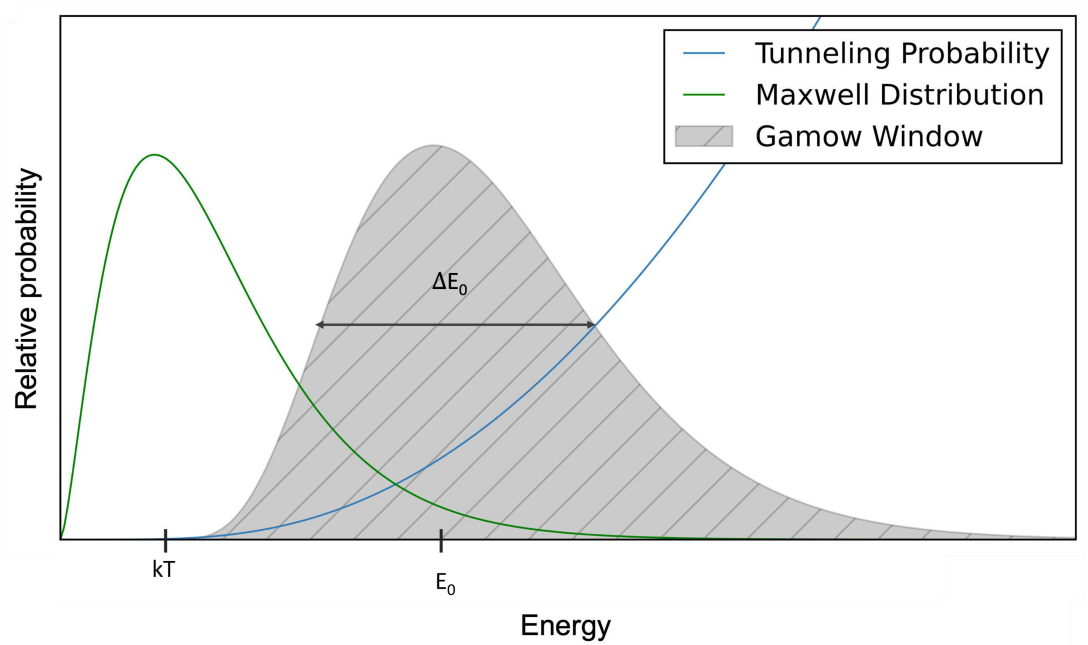

Figure 1.6: Schematic drawing of the Gamow window (grey). It is defined by the Maxwell Boltzmann distribution (green) and the tunneling probability (blue) of the particles, which are the dominant energy dependent functions for charged particle reactions. Based on [25].

that can tunnel through the Coulomb barrier, rising energy and the energy distribution of the particles, which is decreasing for higher energies. This means that the number of available high energy particles is low. The product of these two terms leads to a peak, visible in Figure 1.6. The point at which the product of these two factors reaches its maximum (E_0) is referred to as the Gamow peak. The region around this peak is called Gamow window. The Gamow window thus determines the energy range in which the reactions most likely occur, hence the measurement is astrophysically relevant. The measurements of the cross sections ^{124}Xe(p,γ) and the radioactive isotope ^{118}Te(p,γ) have been performed at energies relevant for nuclear astrophysics, close to the Gamow window.

From this measured cross section, reaction rates can be determined. These reaction rates were obtained in the framework of this thesis and used within network calculations to predict the final abundance distribution.

2 Proton-capture experiment

2.1 Experimental challenges

In this section, a more detailed description of the motivation for choosing an experiment at a storage ring over a classical approach will be given. In a classical approach the target would be a sample, depending on the isotope most likely a solid sample. The light projectile would impinge on the heavy target. As this experiment aimed at measuring a cross-section of a radioactive isotope, the sample would be radioactive and hit by a proton beam.

Depending on the half-life of the radioactive isotope this would already be a major challenge. The target would need to be produced close to the experimental setup, in order not to decay until the experiment is starting, or it has to be produced immediately prior. Depending on the cross section of the isotope the sample would also need to consist of many nuclei in order to reach a reaction rate high enough for determining a cross section, which leads to high activities.

The first step in approaching the problem could be the usage of inverse kinematics. This way the projectile will be the radioactive isotope. The target a proton target. This can be accomplished by using a hydrogen gas-jet target. This, solves the problem of the production of a radioactive target. The ions necessary for the inverse kinematic can be produced in flight, as described later.

As the cross sections of interest for astrophysics are small, the reaction rates with this approach would still be too low. A possibility to achieve a higher number of reactions could be an increase of the size of the hydrogen gas-jet target. However, the ions would lose energy inside the target. This way the cross section would not be measured anymore at a precise energy but integrate over an energy range.

In order to achieve a measurement in the low-energy region, that is interesting for astrophysics, measuring with enough statistics and at a precise energy the storage ring is the right setup. The radioactive ions are stored in the ring and thus pass

multiple times through a thin hydrogen gas-jet target. There is almost no energy loss in the target. The small energy losses that occur when passing the target are compensated in the electron cooler. By recycling the beam, high luminosity of magnitudes of 10^{25} $cm^{-2}\cdot$ s^{-1} can be reached [26]. Compared to single pass experiments with a proton flux of around 10^7 particles per second, target densities of 10^{18} atoms/cm^2 would be needed in order to reach the same luminosity.

2.2 GSI Accelerator facility

This innovative experimental approach has become possible at the research facility GSI (Gesellschaft für Schwerionenforschung) ,Helmholtz Center for Heavy Ion Research, located in Darmstadt, Germany, where two unique facilities, the Fragment Separator (FRS) [27] and the Experimental Storage Ring (ESR) [28] are combined. The FRS enables the production of heavy radioactive nuclei that can be subsequently stored in the ESR.

Figure 2.1 shows a schematic of the accelerator facility at GSI. This facility has the capability to produce and accelerate highly-charged ions from hydrogen up to uranium. The ion source is the starting point for the production of positively charged ions. When these ions enter the following linear accelerator they have been already accelerated up to 0.2% of the speed of light [29]. The ions then enter the Linear Accelerator UNILAC (Universal Linear Accelerator). Within 120 meters they can be accelerated up to 20% of the speed of light [30]. In this experiment the ions get injected from the UNILAC into the ring accelerator SIS18 (Schwerionensynchroton 18). With a circumference of 216 meters the SIS18 can accelerate the ions further on every circulation. Within seconds, they can be accelerated up 90% of the speed of light [31]. The ions can be injected directly into the ESR or into the FRS.

As in this experimental campaign the goal was to determine cross sections for radioactive ions, these need to be produced. By shooting the stable primary ^{124}Xe ions on a Be production target different ions where produced, among them the radioactive isotope ^{118}Te. The fragment separator can separate them by their mass to charge ration from other reaction products in-flight [32]. Afterwards, the ions were stored in the ESR. During this experiment, measurements with the primary ^{124}Xe beam as well as with the secondary ^{118}Te beam were performed.

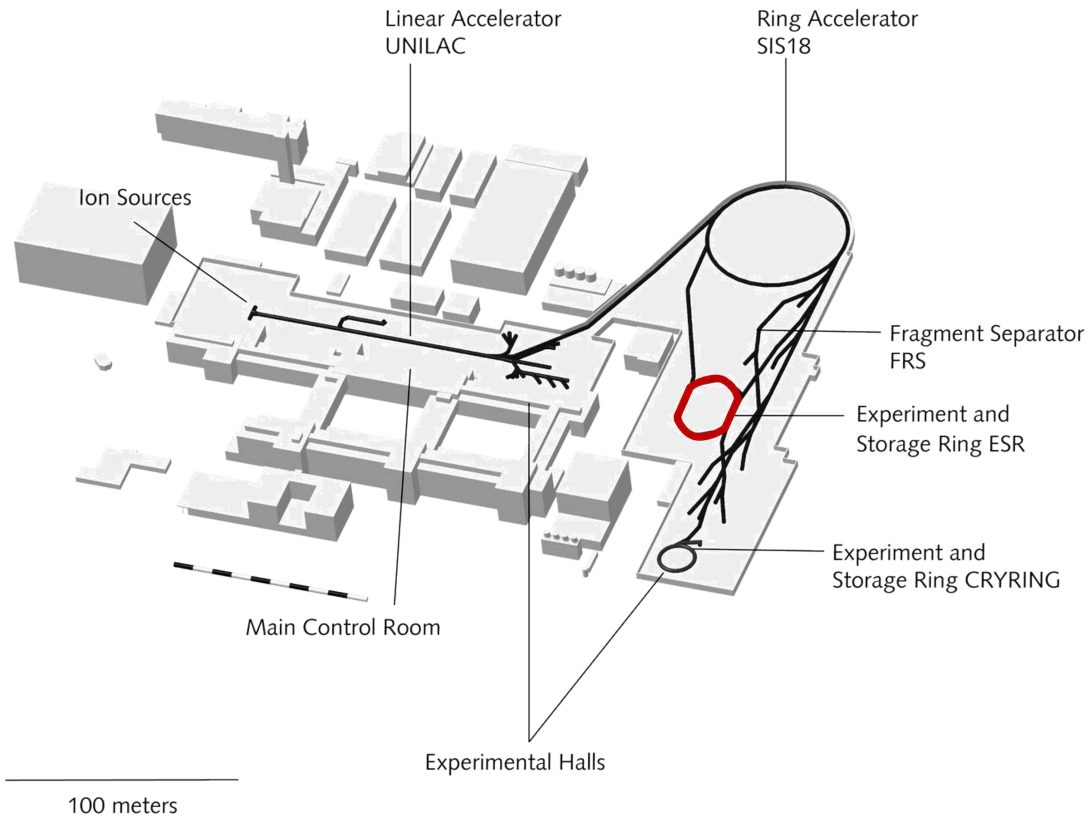

Figure 2.1: Accelerator facility at GSI [33].

2.2.1 The experimental storage ring (ESR)

Figure 2.2 shows a schematic drawing of the ESR. The individual components that modify the beam are labeled and explained in more detail below. The ESR has a circumference of 108.36 m. The red arrow indicates the position of the injection of the beam. For one measurement cycle multiple injections are accumulated in the ESR. The so-called stacking accumulates 20 injections and thus made it possible to reach high beam intensities. The accumulated ions go through different modification phases before the target is turned on and the measurement starts. The ion beam was cooled and decelerated down to 6 and 7 MeV/u providing about 10^6 ions for the measurement.

During each revolution the beam passes through radiofrequency cavities (RF).

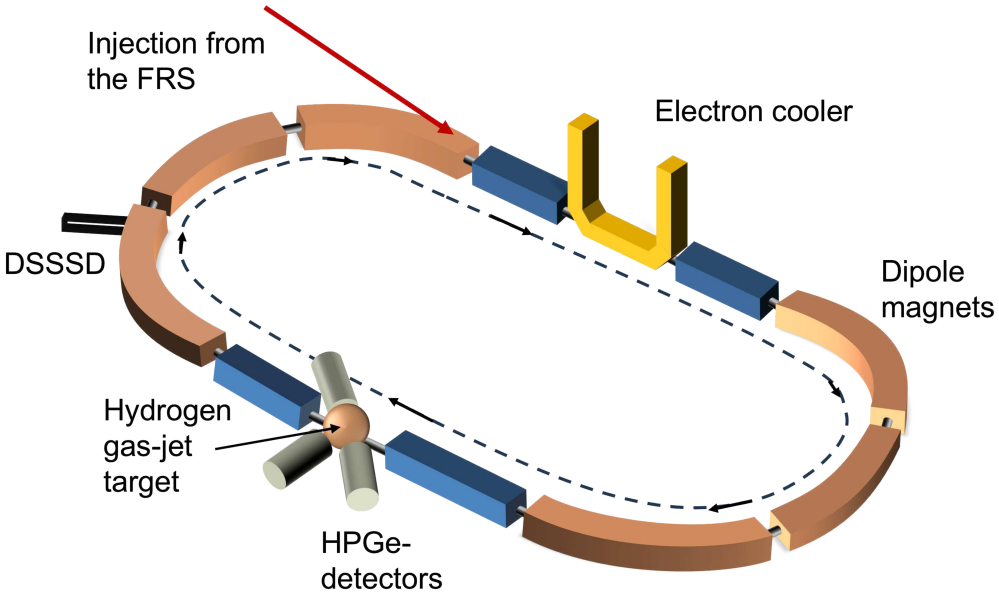

Figure 2.2: Schematic drawing of the ESR.

These RF cavities enable a deceleration of the beam with electromagnetic fields oscillating at radio frequencies. The beam is modified in addition to the radiofrequency cavities by stochastic cooling and electron cooling.

Stochastic cooling

Stochastic cooling was part of the cooling system during this experimental setup. It is designed for rapid cooling. It can reduce the momentum spread of the fragment beam, inserted from the FRS. The ions entering the ESR from the FRS arrive with a momentum spread and emittance for which the electron cooler is too slow [34].

The stochastic cooling is based on a fast-feedback system that measures position and angular mismatch of the ions at one side of the ESR. It applies a suitable correction, using a fast magnet on the opposite side of the ESR. Within a few seconds the fragment beam, which covers the entire momentum spread of the beam ($\Delta p/p = 2\%$) is reduced to a momentum spread of below 0.1%. This pre-cooling of the fragment beam is further increased by the electron cooler [34].

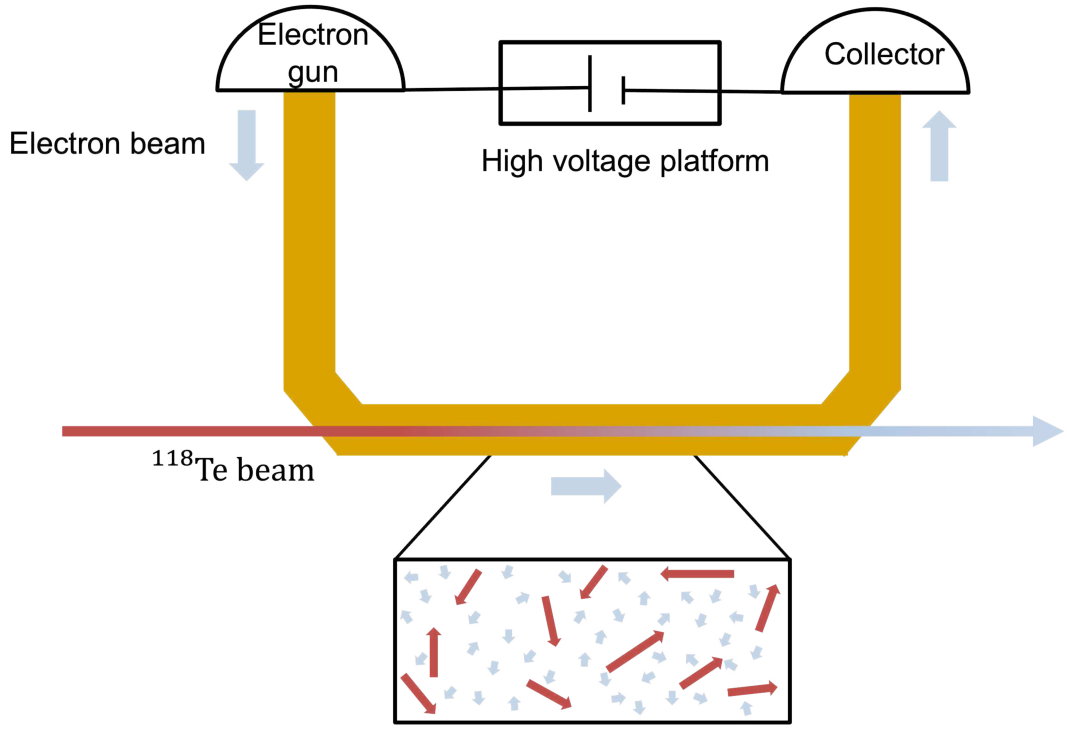

Figure 2.3: Schematic drawing of the electron cooler. With an electron gun, electrons are inserted alongside the recycling beam. The interaction of the cold electrons with the ions leads to a reduction in energy and momentum spread, illustrated by the blue and red arrows. The electrons are stopped by a collector and not recycled like the beam.

Electron cooler

The electron cooler is used to yield the final momentum spread of the ions to about 10^{-5} [35]. This small momentum spread is needed for high resolution experiments. The electron cooler is also used to compensate the small energy losses the ions suffer in the internal target. Without the compensation the ions would get lost very fast. The beam lifetime of the ^{118}Te ions at 7MeV/u resulted to be of about 1.5 seconds [26].

Electron cooling uses the Coulomb interaction of heavy charged particles and a cold electron beam. The interaction between cold electrons and the particles lead to a reduction of energy and momentum spread [36]. Figure 2.3 shows schematically the setup of the electron cooler. The ions are recycled through the electron cooler and thus modified, whereas the electrons well be renewed every time.

2.3 The experiment E127b

The performed experiment was called E127b. It followed the E127 experiment in 2020, that measured the proton capture cross sections of ^{124}Xe at 6.96, 7.92 and 10.06 MeV/u [37]. In the following the details of the E127b will be discussed. It will be given an overview of the whole beam time, about one measurement cycle and about the used detection systems in this setup. Additionally, the normalization of the cross section will be explained.

2.3.1 Beam time schedule

Figure2.4 shows a schematic overview of the beam time schedule. Additionally, the time for the calibration measurements of the X-ray detectors is given. The time of calibration is visualized in grey. A first measurement was performed before the beam time and a second after the beam time. Both measurements were compared for the analysis.

The orange labeled time shows the setup time for the FRS and ESR. Adjustments of the ESR or FRS settings during the beam time are not further visualized as they only covered short time frames. The measurements are displayed in green and red. Red labels the measurements that were not used for analysis. Short interruptions are not labeled.

The measurements were performed under different conditions. In the first part of the beam time ^{124}Xe was measured, with and without the usage of the scraper. In the second part ^{118}Te was measured with the scraper. Within these settings the position of the scraper varied in different data settings. The following setups have been employed during the experiment:

- **Setting 1:** ^{124}Xe beam at 7 MeV/u without the scraper
- **Setting 2:** ^{124}Xe beam at 7 MeV/u with the scraper
- **Setting 3:** ^{118}Te beam at 7 MeV/u with the scraper
- **Setting 4:** ^{118}Te beam at 6 MeV/u with the scraper

The analysis has been performed individually for the different data setting. The measurements without the scraper were mainly used for calibration, due to their high statistics. The data with the scraper was used for the final cross section determination. Within these setups multiple beam cycles were measured. One beam cycle includes accumulation, deceleration and measurement.

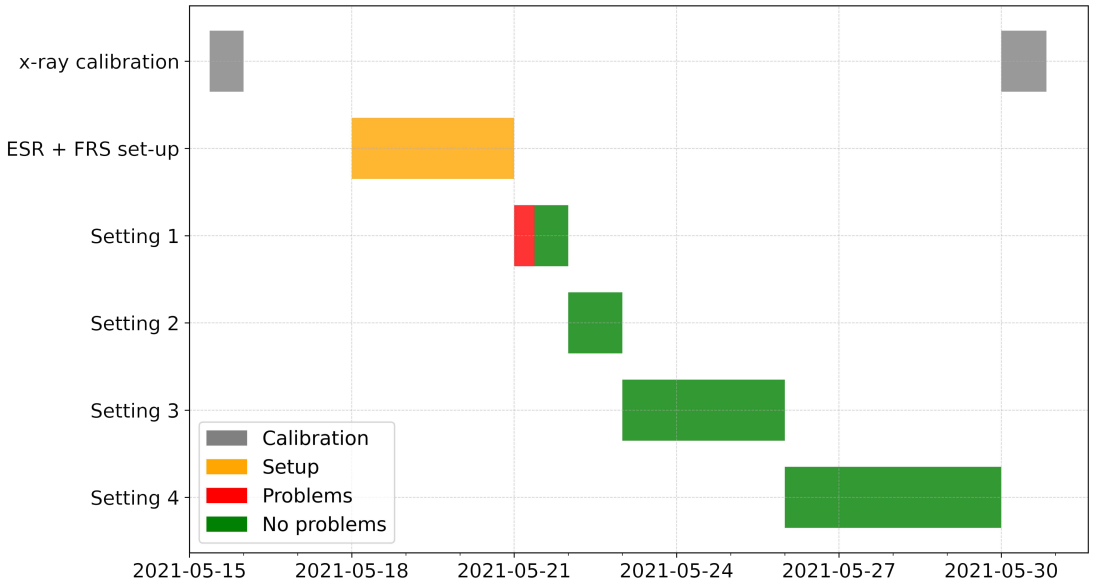

Figure 2.4: Schematic overview of the beam time schedule, including calibration measurements.

2.3.2 Measurement cycle

An overview of the ions in the ESR over time in one beam cycle is illustrated in Figure 2.5. In orange the time of accumulation is marked. From the FRS hot fragments at about 400 MeV/u are inserted into the ESR. These fragments were pre-cooled by stochastic cooling. By accumulating up to 20 injections from the FRS high beam intensities could be achieved [26]. In Figure 2.5 this can be seen by the stepped increase in the number of ions.

The accumulated ions were decelerated to the low energies of the measurement. During this experiment they were decelerated down to 7MeV/u and 6 MeV/u. After the deceleration that is marked in green in Figure 2.5 the electron cooling of the ions continues through the measurement time. The measurement duration in which the data for the analysis is taken, illustrated in red was about 15 seconds [26].

The data during the experiment was recorded by the data acquisition (DAQ). The starting time of a measurement was given by a trigger signal indicated the activation time of the internal gas target. The trigger signal was called target_ON. The measurement stops when another trigger signal is received, that was called target_OFF, indicating that the target is off.

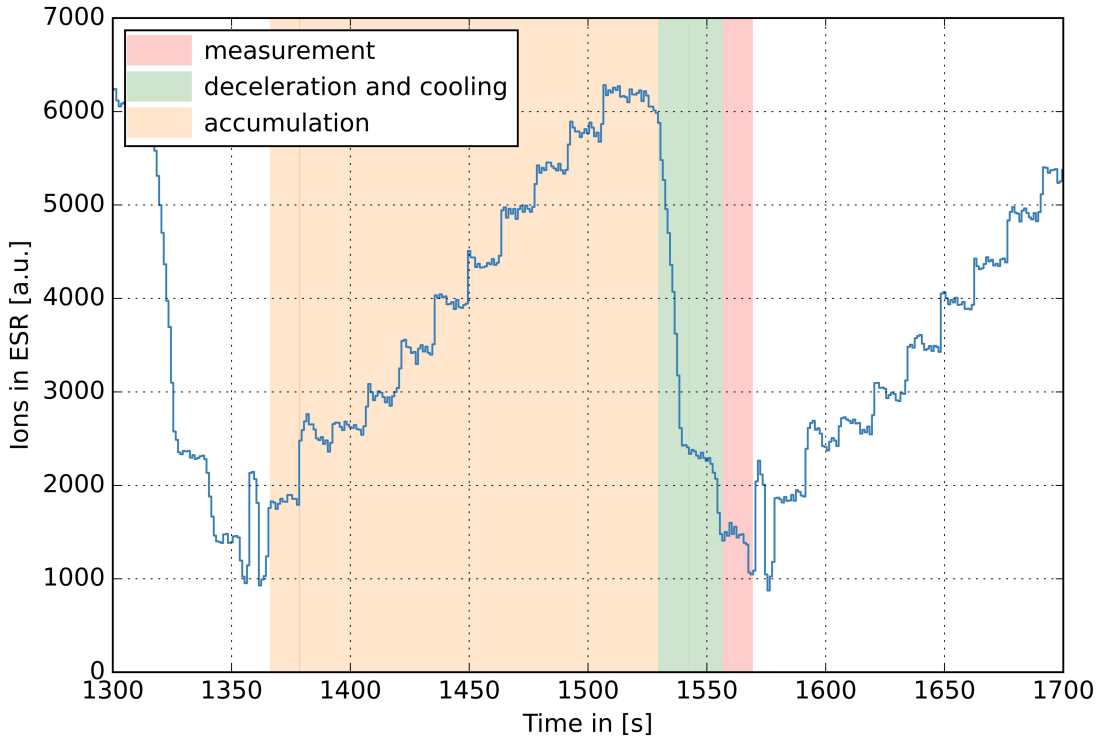

Figure 2.5: Overview of a single beam cycle that includes accumulation, deceleration and measurement of the ions.

2.3.3 Detection systems

The measured data during the experiment has been provided mainly by the HPGe detectors and the Souble-Sided Silicon Strip Detector that will be described in more detail in the following. The data acquisition records the data and modifies it before it is stored in the outputfile for the analysis. The primary input data in the measurement system includes energy and timing signals. The DSSSD provides time and amplitudes of the energy deposition of the heavy recoils after the reaction at the target in its 32 channels. The three HPGe detectors deliver time and amplitudes of the X-rays. This way the relative times between the signals were known. Every DAQ event had a global timestamp.

High Purity Germanium detectors (HPGe)

HPGe detectors are semi-conductor detectors dedicated for photon spectroscopy at high resolution. The detection of a photon is based on its interaction with the

detector material. Photons are absorbed or scattered in matter. Photons that have sufficient energy for ionization, can interact with the electrons of the atomic shell in the material by the photoelectric effect, Compton scattering, and above an energy of 1.022 MeV by pair production [38]. Due to its high atomic number and the resulting good absorption properties, germanium is suitable for the detection of radiation. Semiconductor crystals have a small band gap ($\sim$ 1 eV) between valence and conduction band. Electrons can be excited into the conduction band spontaneously at room temperature. To prevent this, the detectors are cooled. The electrons that are excited into the conduction band leave holes in the valence band. A depletion zone is created in the detector, in which there are no more mobile charge carriers. By applying an external voltage, this zone can be enlarged. This area is used for the detection of photons. When a photon hits this area, electron-hole pairs are generated. These are separated from each other due to the electric field and can then be measured via an anode or cathode. The energy resolution of semiconductor detectors is very good, since the average energy required to produce an electron-hole pair is very low, approximately 1 eV. The pulse is converted to a voltage signal and evaluated by the digital data acquisition and is proportional to the deposited energy.

Double-sided silicon strip detector

To detect the products of the (p,γ) reaction, a Double-Sided Silicon Strip Detector (DSSSD) has been used. The material of this detector, silicon, is a semiconductor. In the case of silicon there is a band gap of 1.1 eV. This means, that electrons in the valence band need to overcome this band gap in order to be lifted into the conduction band. By manipulating the material, the attraction of electrons or holes for the conduction band or the valence band can be increased, by introducing lower energy states within the band gap. These semiconductors are then called n- or p-type semiconductor. By combining these conductor types, a layer is created between them which is called depletion layer. In this layer all free electrons and holes are combined. By applying a voltage across the depletion layer, it can be further expanded. If a charged particle passes through this region it generates electron-hole pairs inside this layer.

Figure 2.6 shows a schematic view of the detector. If the particle enters the depletion layer it creates electron-hole pairs that diffuse to different sides. Due to the electric field, these pairs become separated and can be read out, providing information about the deposited energy of the particle. This information can be obtained from both the n-side and the p-side of the detector. The design of the double-sided silicon strip detector builds up on this principle. The p-side of the detector is divided into 16 strips, while the n-side is similarly divided into 16

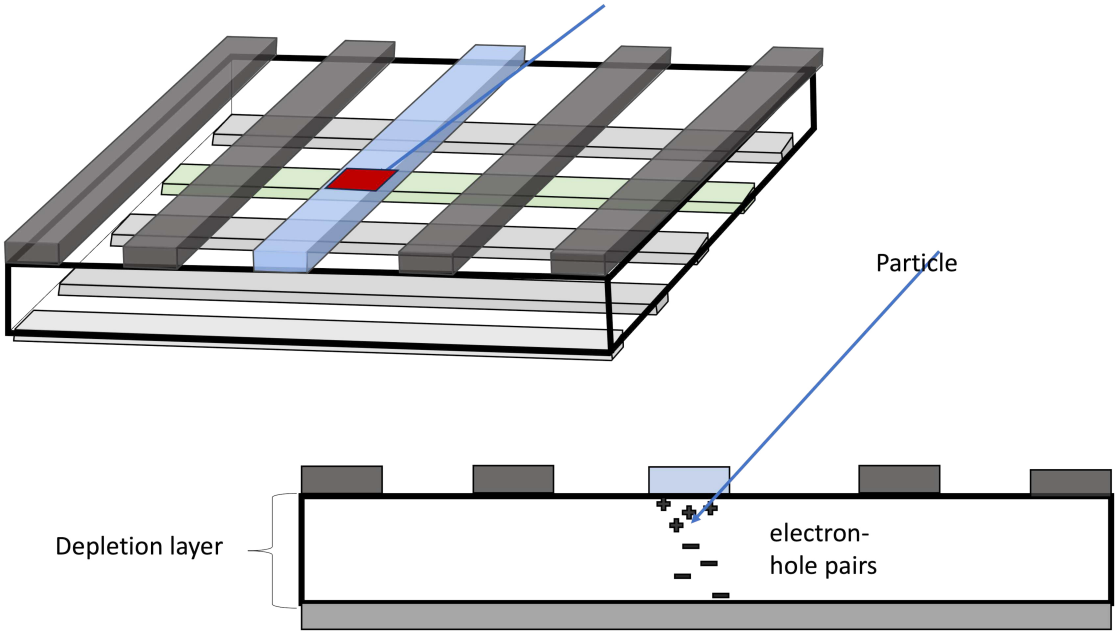

Figure 2.6: Schematic drawing of a Double-Sided Silicon Strip detector (DSSSD). The strips in which energy was deposited by the particle are marked in green and blue. The combination will be called pixel and is defined by the red area.

strips, oriented perpendicularly to the p-side strips. Consequently, when energy is deposited in the depletion layer on the n-side, one of the p-side strips also registers a response. These corresponding strips, that measured a signal in coincidence are marked in blue and green in Figure 2.6. As these strips are oriented orthogonal to each other, the resulting region where the particle deposited energy forms a so-called pixel, visualized in red in Figure 2.6. This allows a localization of the energy deposition. The detector had a size of (49.5 x 49.5)mm^2. With the 16 strips this leads to a resolution of 3.125 mm

2.4 Cross section normalization

This work aims at the determination of a cross section for a proton capture under gamma emission. The cross section describes the probability that a reaction occurs. The measurement requires the determination of the number of reaction products after the proton capture, the number of protons, as well as the number of ions prior to the capture. This would be the number of ^{118}Te ions before capture and the number of ^{119}I ions after capture. To determine this, the number of ions in the ring, as well as the target density has to be known exactly. Alternatively the cross section can also be determined relative to a parallel occurring process. This approach often yields smaller uncertainties. In this experiment the proton capture cross section is determined relative to the electron capture at the hydrogen gas-jet target. A more detailed description of the electron capture process will be given in the following subsection 2.4.

The following formula describes the determination of the (p,γ) cross section relative to the radiative electron capture cross section (K-REC):

$$\sigma_{(p,\gamma)} = \frac{N_{(p,\gamma)}}{N_{\mathrm{K-REC}}} \cdot \sigma_{K_R EC} \tag{2.1}$$

Here $N_{(p,\gamma)}$ describes the number of reaction products of the proton capture under gamma emission. The determination is described in more detail in section 2.5. $\mathrm{N_{K-REC}}$ is the number of emitted photons after electrons from the target atoms are captured in the K-shell of the bare, stored ion. In order to obtain $N_{\mathrm{K-REC}}$ the number of detected events has to be corrected by the efficiency of the detector. The efficiency of the used X-ray detectors is given by $\epsilon_{\mathrm{K-REC}}$ and will be determined in section 2.4.1. A closer description of the X-ray detectors, HPGe-detectors, used is given in subsection 2.3.3.

The efficiency for the DSSSD is assumed to be 1. This is based on the high energies that are deposited in the detector and thus fully stopped and on the experience of previous experiments. In the framework of this thesis one analytical approach was performed that corrects the number of detected events by an efficiency. More details about this approach will follow in section 4.3.2.

The angle dependent cross section $\sigma_{K_R EC} = \int_{\Delta\Omega} \frac{d\sigma_{\mathrm{K-REC}}}{d\Omega} d\Omega$ of the radiative electron-capture into the K-shell can be predicted very accurately, with an uncertainty of 1% by theory [39]. The theoretically predicted cross sections for ^{124}Xe and ^{118}Te at the measured energies can be found in section 2.4.3.

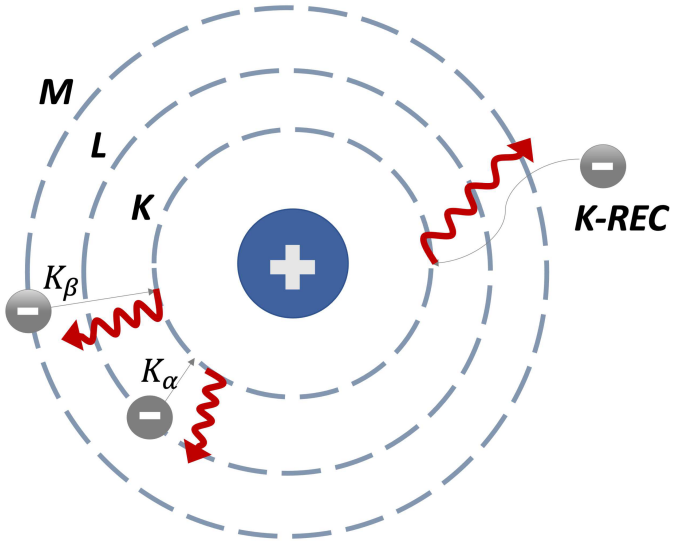

Figure 2.7: Schematic drawing of the radiative electron-capture into the K-shell (K-REC).

Radiative Electron-Capture process (REC)

When a charged ion captures an electron and simultaneously emits a photon, the recombination process is called radiative electron-capture (REC). During this experiment, this process can occur when the stored ions pass through the hydrogen gas-jet target and possibly capture an electron from the target ions. If an X-ray photon ionized an atom by removing an electron, an empty place in one of the shells will occur. Figure 2.7 shows schematically an electron capture-into the K-shell of an atom. This capture is called K-REC. Figure 2.7 illustrates also more of the outer shells of the atom which are labeled as K-, L-, and M- shell. The electrons can be captured into the different shells of the atom. Dependent on the energy further cascades between the shells can take place. The advantage of the capture into the K-shell is, that the cross section is very large, leading to high statistics.the emitted photon has an energy that is clearly differentiable from cascades. The emitted X-rays are detected by three HPGe detectors, positioned under different angles.

The radiative electron capture is the time-reversed process of the photoionization process, in which matter ejects electrons under the influence of electromagnetic radiation. As this process is well understood it is possible to do theoretical calculations with high accuracy and determine the K-REC cross section for any energy [1].

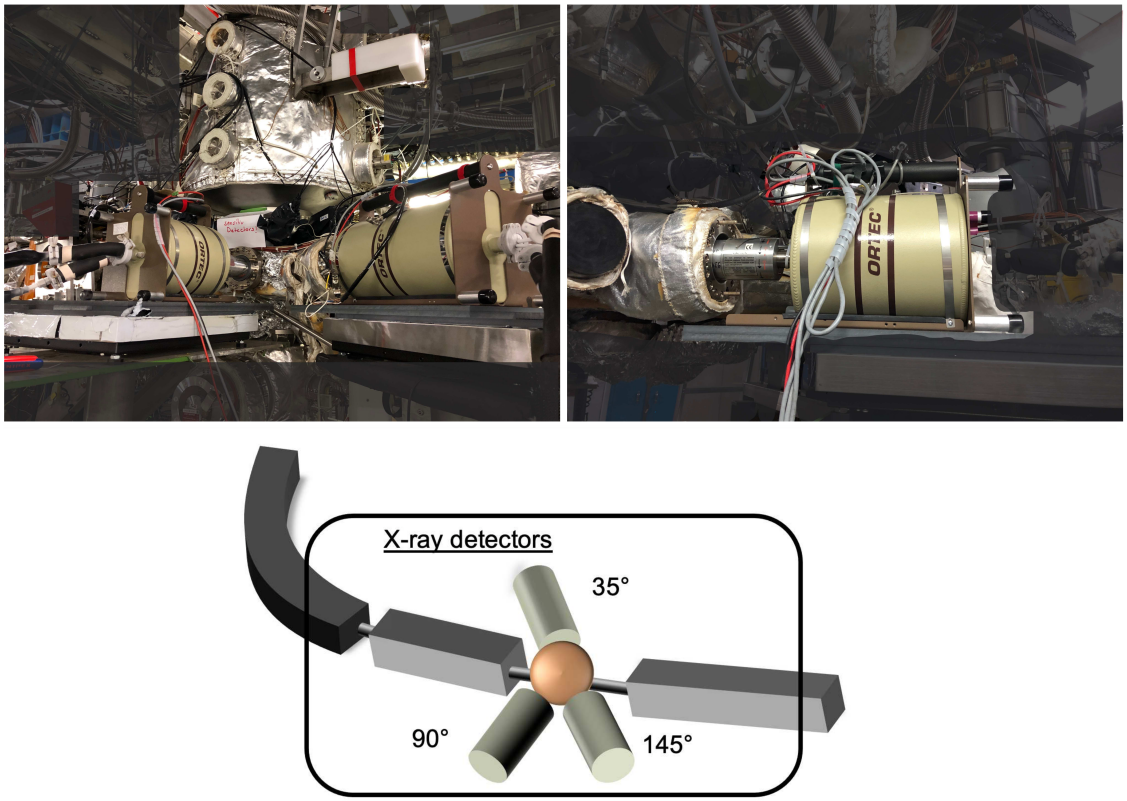

Figure 2.8: Pictures and a schematic drawing of the HPGe-detectors. The detectors are placed around the target at 35°, 90° and 145° and measure the photons that are emitted in the target section.

2.4.1 Calibration of the HPGe-detectors

In order to determine the number of counts ($N_{\mathrm{K-REC}}$) from the electron capture into the K-shell, three detectors where used. The detectors used in this experiment HPGe detectors. They have been positioned under different angles at 35°, 90° and 145° with respect to the gas-jet target. The placement of these detectors at different angles allowed for an analysis of the isotropically emitted radiation, from different positions. Figure 2.8 shows two pictures and a schematic drawing of the three detectors in the target region. It illustrates the positioning and orientation of the HPGe detectors relative to the gas-jet target. To ensure accurate measurements, the HPGe detectors where energy and efficiency calibrated, both prior to and following the experiment. The calibrations will be explained in more detail in the following subsection.

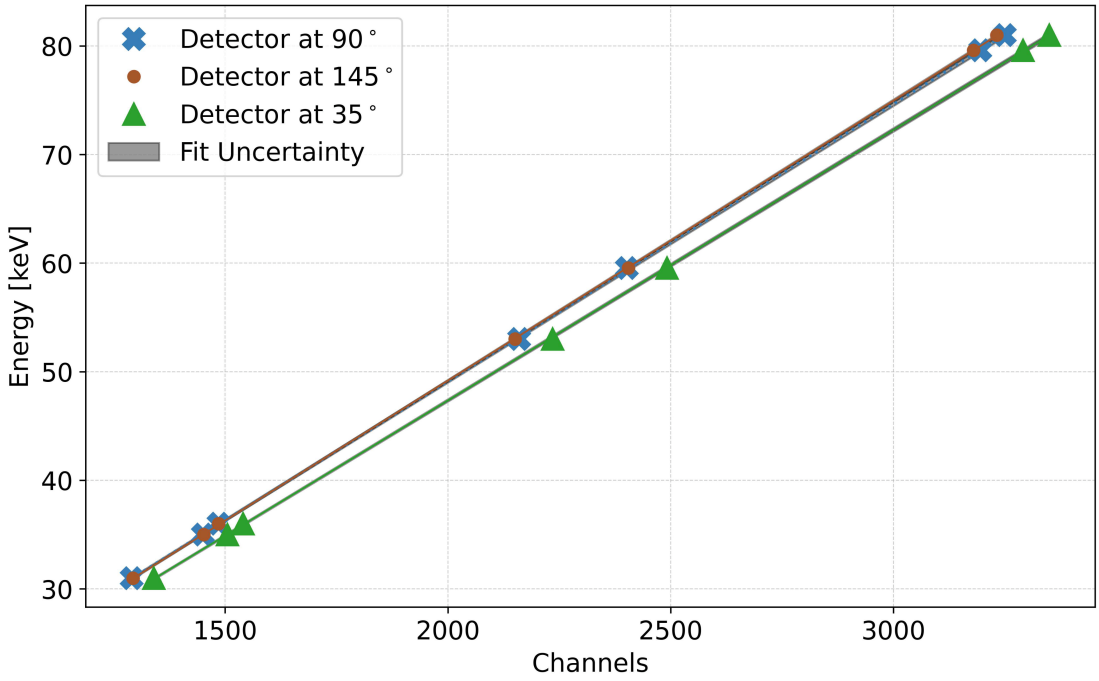

Figure 2.9: Energy calibration of the HPGe-detectors.

Energy calibration

For the energy calibration, γ-ray sources with well known emission properties were used. These calibration sources were ^{210}Pb, ^{241}Am and ^{133}Ba. They are emitting characteristic gammas of energies between 26 and 81 keV. By using the characteristic lines of the sources an energy calibration was performed. Correlating the pulse heights registered by the detector to the expected energy values of these cal-

Detector angle [°]	a [keV/channel]	b [keV]
90	0.0255 ± 0.0002	-1.98 ± 0.14
145	0.0258 ± 0.0001	-2.4 ± 0.9
35	0.0249 ± 0.0002	-2.5 ± 0.1

Table 2.1: Results of the energy calibration of the HPGe detectors, obtained from a linear fit. The coefficient a describes the slope and b the intersection of the fit.

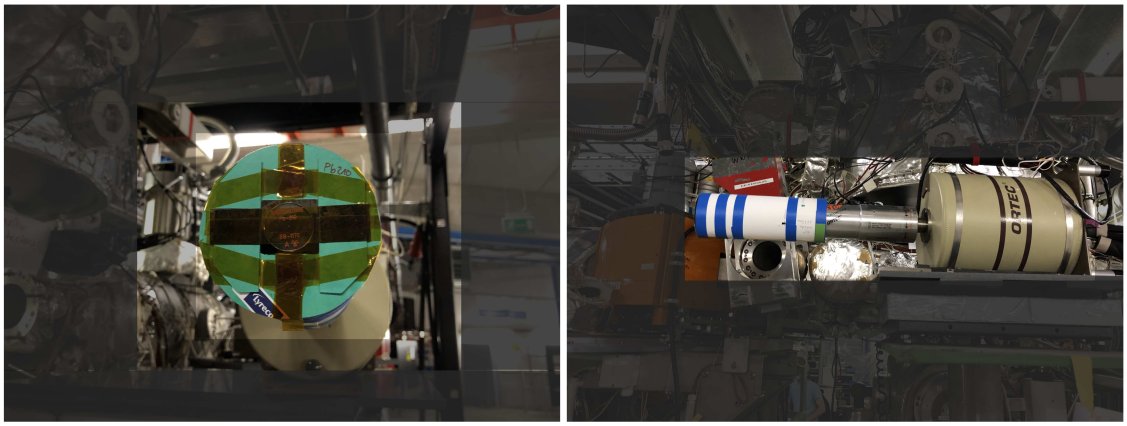

Figure 2.10: Set up for the calibration of the HPGe-detectors, in order to reproduce the geometry during the experiment. The left picture shows a front view with one of the measured calibration sources. On the right picture a side view is given.

ibration sources, a calibration correlation was established. The pulses are assigned to a channel, and they follow a linear relation with the corresponding energy:

$$E(\text{Channel}) = a \cdot \text{Channel} + b \tag{2.2}$$

During the energy calibration, the unknown factors a, b must be determined. Once these factors were determined, the calibration of ^{124}Xe and ^{118}Te spectra was possible. Visualized in Figure 2.9 is the relation between the energy and the corresponding channels, illustrating the linear behaviour. The parameters of the linear fit are shown in Table 2.1.

Efficiency calibration

Part of the radiation emitted by a source is not detected. The rate of photons detected to emitted by the source is referred to as the detector efficiency. This detector efficiency can be measured using calibration sources with known activities and gamma emission intensities. For this purpose, the same sources, ^{210}Pb, ^{241}Am and ^{133}Ba, as for energy calibration were used. In order to acquire an efficiency value that accurately reflects the specific geometry between the target and detectors, for the efficiency calibration the setup had to be reproduced geometrically. Figure 2.10 shows the setup of the calibration of the detectors for one detector. The setup during the efficiency measurement ensured that the solid angle coverage

is the same as during the experiment.

The efficiency of the detectors can be experimentally determined with the following formula:

$$\epsilon = \frac{N_{counts}}{I_\gamma \cdot \tau \cdot A \cdot t_{meas}}. \tag{2.3}$$

The number of detected events at the corresponding energy is N_{counts}, the activity of the calibration sources at the time of the measurement is A, the line intensity of the measured gamma line is I_γ, the measured time is t_{meas} and τ is the dead time of the detector. In order to obtain the activity at the moment of measurement, the activity A_0 at time t_0 has to be corrected by the decay of the source during the waiting time t_w:

$$A = A_0 \cdot \exp\left(-\lambda t_w\right) \tag{2.4}$$

The activities A_0 of the used calibration sources have been taken from the corresponding source certificates. The decay constant of the radioactive source is λ. As the measurement time is much shorter, than the decay constant a correction of the decays during the measurement time can be neglected. The determined efficiencies for the three HPGe-detectors are shown in Figure 2.11. The data were fitted in order to extract the efficiency $\epsilon_{\mathrm{K-REC}}$ at the energy of the electron capture into the K-shell. As an analytic fitting function for the efficiency the following formula was used:

$$\epsilon(E) = a \cdot \exp\left(b \cdot E\right) + c \cdot \exp\left(d \cdot E\right) \tag{2.5}$$

The energy lines for ^{124}Xe and ^{118}Te are expected in the region of 40 to 46 keV for the detector at 90°. In these regions the fit uncertainty is in the order of 4 %.

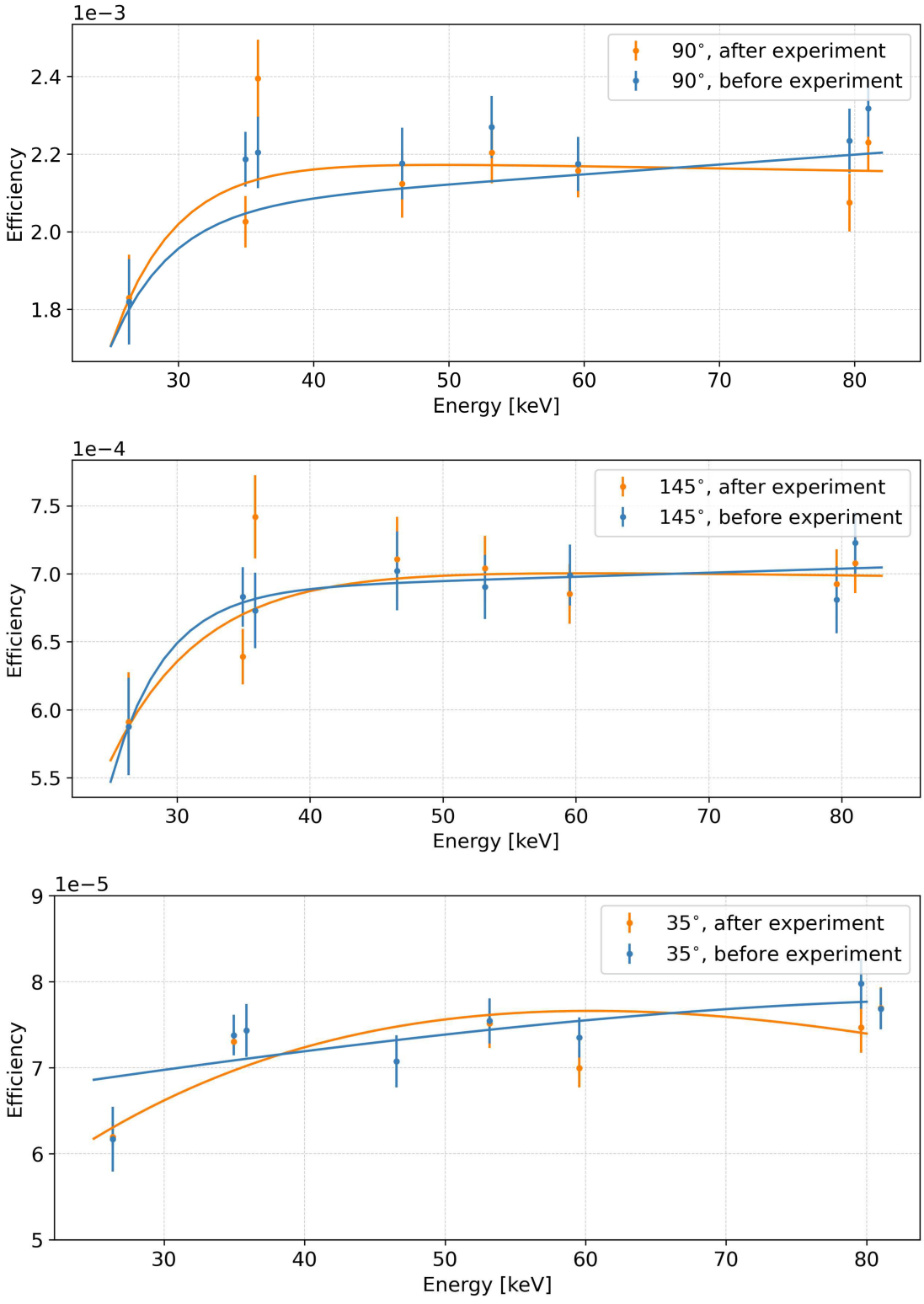

Figure 2.11: Efficiency determination of the HPGe-detectors for 90°, 145°, 35°, starting from the top respectively.

2.4.2 Beam energy reconstruction

In the previous sections the beam energies have been referred to as measurements at 6 and 7 MeV/u. These values are not the exact energies. The electron cooler is responsible to keep the beam at a precise energy. Thus, with the information obtained from the electron cooler the precise energies can be determined [40].

The voltage set at the electron cooler differs from the actual measured voltage. In order to determine the exact voltage an offset has to be subtracted from the set values. The offset in this experimental setup was -95 V. In addition, the space charge potential Φ_0 of the electron beam has to be taken into account. It reduces the effective voltage seen by the electrons and thus reduces their energy. If the density of the electrons is assumed as constant, the space charge potential Φ_0 can be determined with [40]:

$$\Phi(r) = -\frac{I_{\mathrm{set}}}{4\pi\epsilon_0\beta_0 c}\left(1 + 2\ln\frac{R_{\mathrm{tube}}}{R_{\mathrm{e-beam}}}\right). \tag{2.6}$$

In the equation the radius of the electron beam $R_{\mathrm{e-beam}}$ is 2.54 cm. It is smaller than the radius of the tube R_{tube}, with a value of 10 cm. The current of the electrons is I_{set}, its values can be found in Table 2.2. The constant $\epsilon_0 = 8.854 \cdot 10^{-12}\frac{\mathrm{Vm}}{\mathrm{As}}$. Since $\beta_0 = \frac{v}{c}$ it can be determined from the Lorentz factor:

$$\gamma = \frac{1}{\sqrt{1 - \frac{v^2}{c^2}}}. \tag{2.7}$$

Therefore:

$$\beta_0 = \sqrt{1 - \frac{1}{\gamma^2}}. \tag{2.8}$$

For the space charge potential the formula can be reduced to:

$$\Phi_0 = -0.11215 \cdot \frac{I_{\mathrm{el}}}{\beta_0} \tag{2.9}$$

Following, the effective voltage V_{meas} can be determined with:

$$V_{\mathrm{meas}} = V + V_{\mathrm{offset}} + \Phi_0. \tag{2.10}$$

The final values for V_{meas} as well as V_{set} can be found in Table 2.2. The uncertainty of the voltage offset is in the order of around 10 %. With the corrections for the voltage, the energy of the electrons E_{el} can be determined:

$$E_{\mathrm{el}} = e \cdot V_{\mathrm{meas}}, \tag{2.11}$$

where e is the electron charge. Knowing this, also the exact energy of the ions can be calculated. The kinetic energy of the ions is described by:

$$E_{\mathrm{kin}} = mc^2\gamma - mc^2, \tag{2.12}$$

with m being the mass of the ions [41]. Combining with the Lorentz factor γ:

$$(\gamma - 1) = \frac{E_{\mathrm{kin}}}{mc^2} \tag{2.13}$$

In the equilibrium (γ - 1) is the same for electrons and ions. Thus, the energy of these ions can be calculated with: [40]:

$$E_{\mathrm{ion}} = E_{\mathrm{el}} \cdot \frac{M_{\mathrm{ion}}}{M_{\mathrm{el}}} \tag{2.14}$$

In Table 2.2 all final values are given. In general, this calculation is iterative. In this case five iterations have been performed, β_0 is assumed as a good estimate. The uncertainties for the final energy are of around 0.3%. The contribution to this uncertainty is coming from the uncertainty of the measured voltage offset. The uncertainty of the momentum spread of the beam can be neglected.

Ions	E_{nom} [MeV/u]	V_{set} [V]	V_{meas} [V]	I_{set} [mA]	E_{ion} [MeV/u]
^{124}Xe	7	4008.3	3913 ±10	50	7.05 ± 0.02
^{118}Te	6	3460.5	3364 ±10	50	6.044 ± 0.018
	7	4008.3	3913 ±10	50	7.05 ± 0.02

Table 2.2: Beam energies calculated at which the measurements where performed. V_{set} describes the voltage set at the electron cooler and V_{meas} the value under which the measurement was performed. The set current is given by I_{set} and the final energy of the ions by E_{ion}.

2.4.3 Theoretical differential cross section of the electron capture

The cross section of the electron capture can be predicted very accurately by theory [1], as explained in section 2.4. The used cross section was calculated by Prof. Dr. Andrey Surzhykov [42]. The uncertainty of this cross section is estimated to be in the order of 1%. In Table 2.3 the theoretically determined differential cross sections $\frac{d\sigma_{\mathrm{K-REC}}}{d\Omega}$ for the HPGe detectors, positioned at 90°, 145° and 35° are shown. The size of the solid angle of the detector is neglected. The cross-section at the central detector position is used. The effect is covered within the the uncertainty of the cross section [43].The values are shown for the two energies of the ^{118}Te beam, as well as for the ^{124}Xe beam.

2.4.4 Determination of the number of electron captures in the K-shell

After successfully calibrating the energy and efficiency parameters, the spectra obtained during the beam time can be used to determine the number of emitted photons subsequent to electron capture into the K-shell.

E [MeV/u]	$\frac{d\sigma_{\mathrm{K-REC}}}{d\Omega}$ [barn/sr]		
^{118}Te	90°	145°	35°
6.044	206 ± 2	66.9 ± 0.7	70.4 ± 0.7
7.05	176 ± 2	56.8 ± 0.6	59.8 ± 0.6
^{124}Xe			
7.05	190 ± 2	61.1 ± 0.6	65.1 ± 0.7

Table 2.3: Theoretical determined differential cross sections $\frac{d\sigma_{\mathrm{K-REC}}}{d\Omega}$ for the HPGe detectors, positioned at 90°, 145° and 135°.

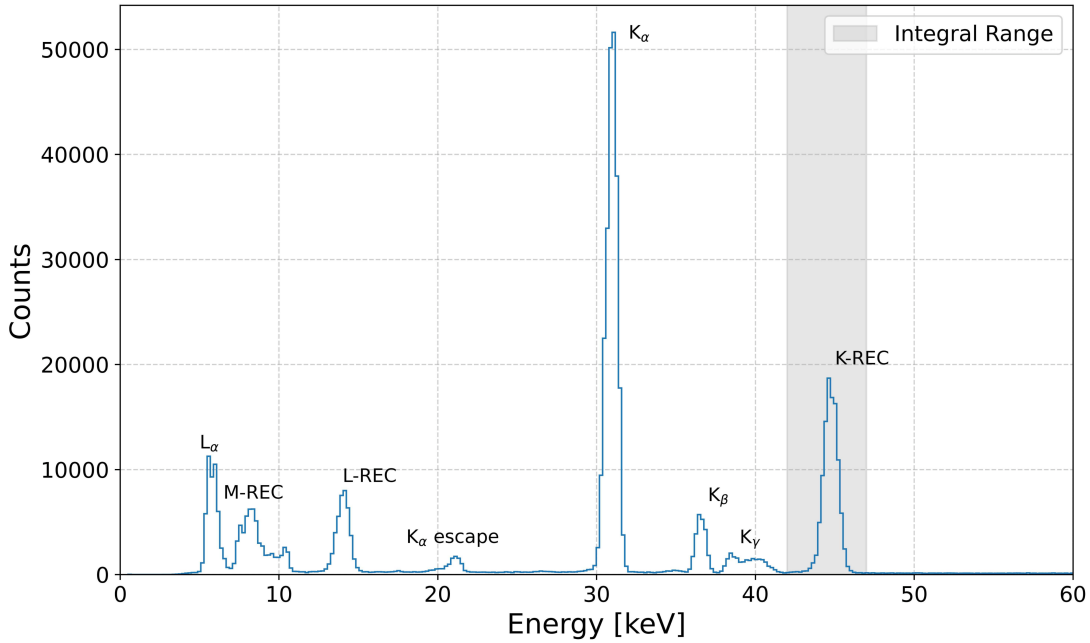

Figure 2.12: Calibrated X-ray spectrum recorded by a HPGe-detector, positioned under an angle of 90° in the target region during the measurement with the ^{124}Xe beam at 7 MeV/u.

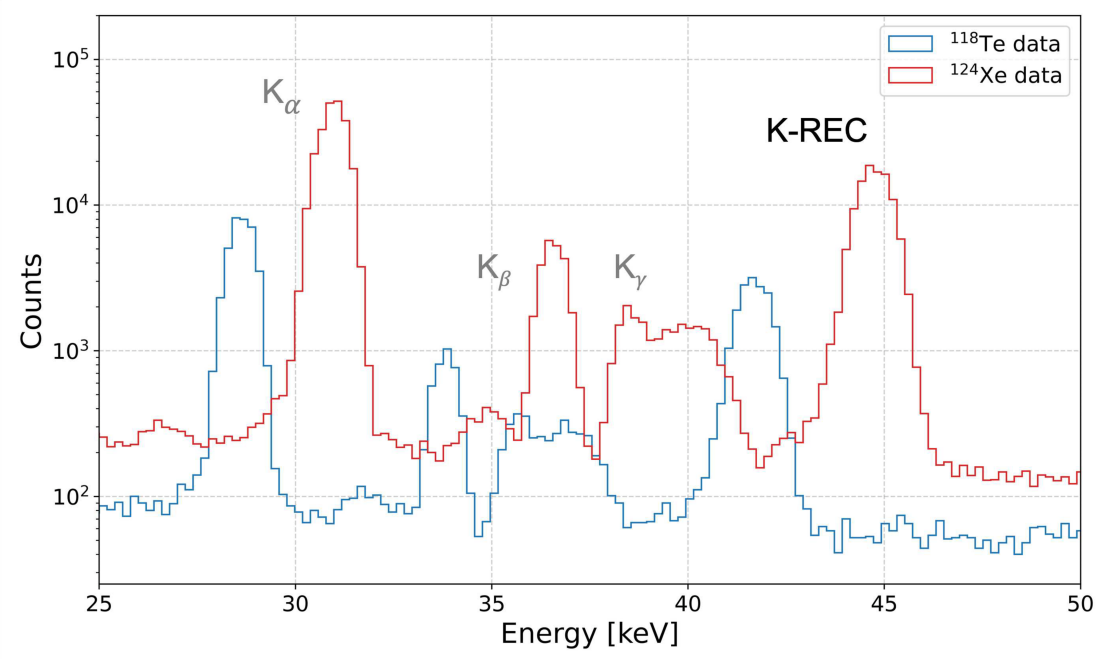

Figure 2.13: Calibrated X-ray spectrum of ^{124}Xe (red) and ^{118}Te (blue) both at 7 MeV/u, measured with the HPGe-detector at 90°.

Figure 2.12 shows an x-ray spectrum that has been taken during the experiment with a HPGe-detector under an angle of 90°. Labeled with K-REC is the corresponding peak for photons emitted after an electron is captured into the K-shell. Moreover, within the spectrum, there exist more peaks corresponding to other captures. The peak denoted as K_β results from the photons emitted after a cascade into the K-shell after a capture of the electron into the M-shell. Similarly, the peak emerging from the capture into the L-shell, cascading to the K-shell is marked with K_α. By integrating over the K-REC peak and subtracting a linear background fit the number of counts in the peak can be determined. The area over which the integration took place is marked in grey. Figure 2.12 shows exemplary the case for an angle of 90°. This spectrum has been measured with the ^{124}Xe beam at 7 MeV/u. For the other angles and energies the determination of counts was done in the same way.

The spectrum is individual for every measured ion. In Figure 2.13 the X-ray spectrum of ^{124}Xe at 7 MeV/u is compared to the spectrum of ^{118}Te at 7 MeV/u. As all peaks can be identified the spectra can also be used to determine, if a contamination of other ions was in the setup [26]. This ensures a clean measurement during this experiment with only ^{124}Xe or ^{118}Te ions.

2.5 Detection of the (p,γ) reaction products

In order to detect the reaction products resulting from proton capture, thex were separated from the stored beam. The challenge lies in identifying and counting the reaction products. The approach for a separated detection is the usage of a dipole magnet. In the experimental setup, the dipole magnet was positioned behind the target section. It provides magnetic separation between the reaction products and the stored beam. Figure 2.14 presents a schematic drawing of this magnetic separation process. The unreacted beam is drawn in blue, showing its trajectory within the dipole magnet. Since the particles are charged the magnetic field (B) forces them onto a circular trajectory within the field. The degree of bending, referred to as the bending radius (ρ), can be derived via Lorentz and centripetal force:

$$B\rho = p/q \tag{2.15}$$

After a proton capture the momentum p remains almost unchanged. Based on the assumption hat the emitted gammas as well as the captured protons have negligible momentum. The charge q of the reaction product increases by one when capturing a proton. This leads to a decreased bending radius. The reaction products thus shift to the inner side of the ring. The shift of the reaction products

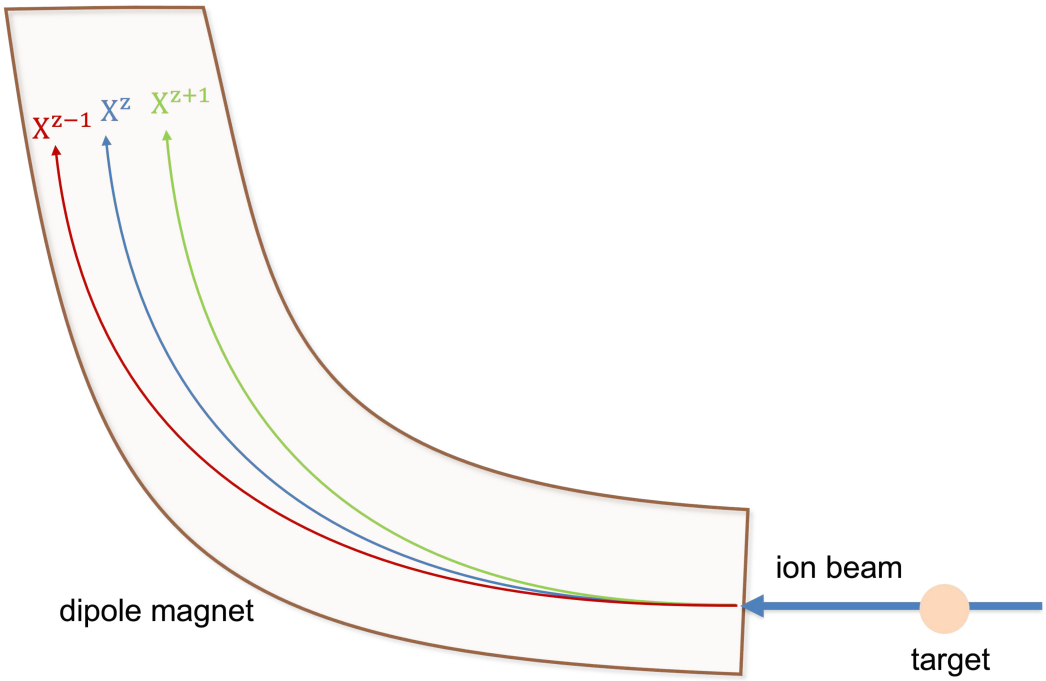

Figure 2.14: Separation of the reaction products inside the dipole magnet.

of the proton capture is illustrated in green. If the charge of the ions would be decreased by one, the reaction products would shift to the outer side of the ring as it is the case for electron capture. In Figure 2.14 this is shown by a red line. In a previous experiment this has been used to detect the down-charged ions produced by electron capture [44]. By placing a detector at the inner side of the ring the reaction products of the proton capture can be observed. Figure 2.15 illustrates a schematic drawing of the used detector at the inner side of the dipole magnet. The used detector is a Double Sided Silicon Strip Detector (DSSSD). It consists of 16 strips in x and 16 strips in y direction. The detector is described in more detail in section 2.3.3. This approach allows an exact determination of the number of the reaction products.

In addition to the reaction products of the proton capture, other reactions are registered by the DSSSD. The ^{118}Te ions can also scatter at the atoms of the hydrogen target. This so-called Rutherford scattering will be described in more detail in the following subsection. The detected scattered particles form a background from which the reaction products must later be distinguished. But already in Figure 2.15 it becomes visible that the Rutherford scattering is influencing the peak to background relation.

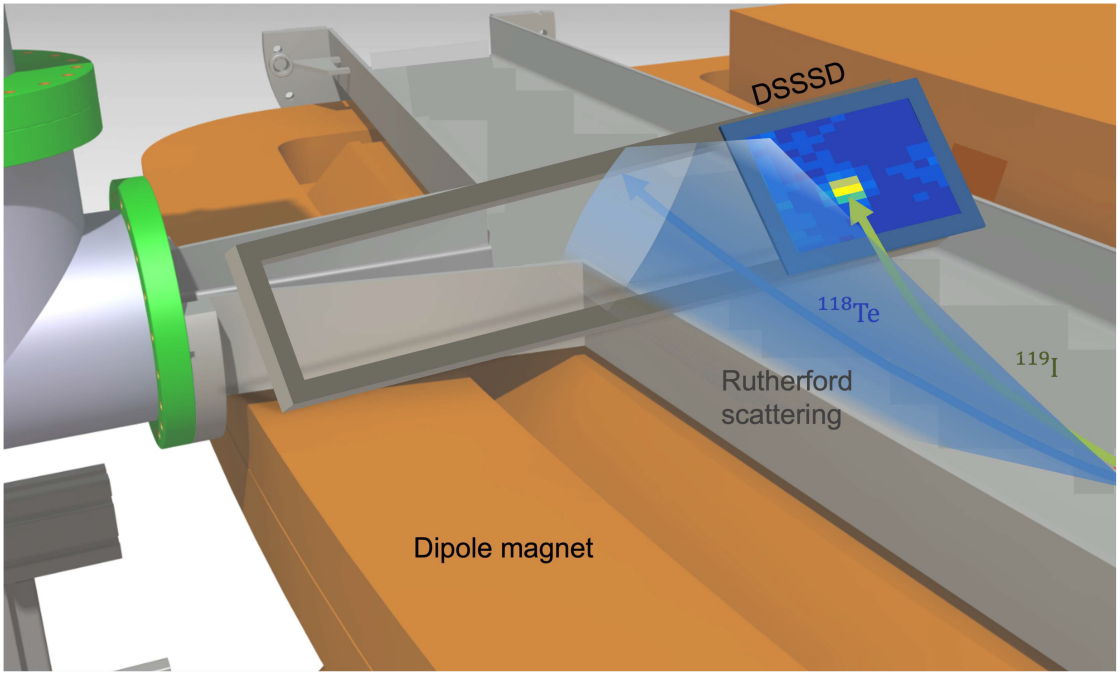

Figure 2.15: Schematic drawing of a DSSSD placed at the inner side of the ring, based on [45].

2.5.1 Rutherford background

As briefly mentioned in the previous subsection in the target region, additional processes occur alongside the proton capture. The proton capture at the target occurs only rarely. In contrast, many ions scatter at the atoms of the target. This scattering, referred to as Rutherford scattering, introduces a significant background contribution [46]. The particles lose energy by scattering at the target. In case of backward scattering more than in the case of forward scattering. Based on the smaller cross sections at lower energies, the peak-to-background relation is significantly worse for low energies. Figure 2.16 shows schematically, the scattering of the ions in all directions. The perspective angle is from above. This makes it possible to determine which scattered particles are going to hit the detector. Connected by a dashed line, two regions are marked, that are supposed to be the forward and backward scattered particles that will hit the detector at the same strip. By analyzing the deposited energy it is possible to distinguish between forward and backward scattering. For small expected (p,γ) cross sections the Rutherford background can hamper the analysis significantly and can introduce large uncertainties. This is the central challenge of the current experiment, since the low energy cross sections, relevant in astrophysics can be very small and

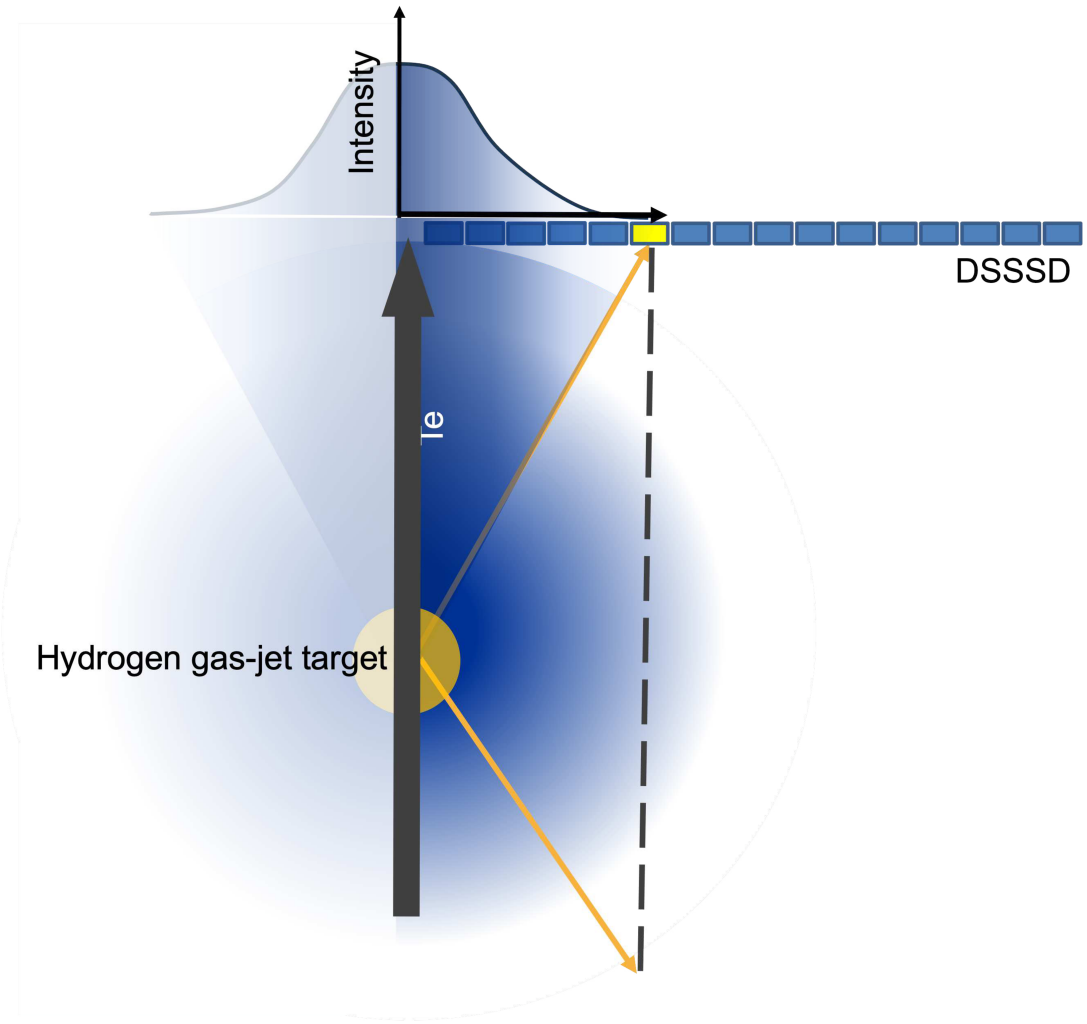

Figure 2.16: Schematic drawing of the Rutherford background formation

radioactive beams have limited intensities. In order to reduce the background contribution by the Rutherford background in a previous PhD thesis a scraping technique has been developed and tested for the first time during this beam time with the ^{124}Xe primary beam [37]. This has made it possible to go to low energies of 6 MeV/u for this experiment.

2.5.2 Scraping technique

The idea behind this scraping technique is the usage of a stainless steel sheet that is positioned in the region of the Rutherford cone, to block the background before

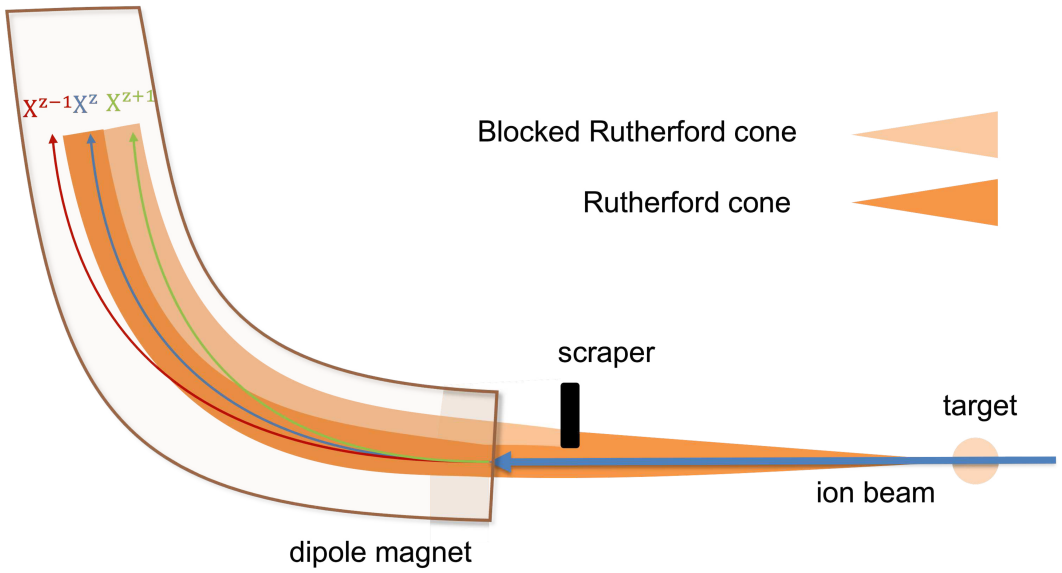

Figure 2.17: Schematic drawing of the scraping technique [37].

entering the dipole-magnet. This device will be called scraper in the following. The development of this scraper was part of a previous PhD thesis from Lazlo Varga, more details on the scraper can thus be found in his thesis [46]. Figure 2.17 shows schematically the usage of the scraper. Right after the target, the (p,γ)-reaction products and the primary beam have the same trajectory. The developing Rutherford cone around this trajectory extends over the flight distance. This results in a separation of the reaction products, that are of interest and the scattered particles. By placing the scraper into the region of the scattered particles the background can be blocked. The particles that are not blocked enter the dipole magnet and the reaction products can be, as described above, magnetically separated.

For a better understanding of the setup, as well as the reactions that took place, simulations were performed. These simulations also predict a background free measurement in the region of the (p,γ)-peak, with the usage of the scraper. In the following chapter, before the recorded data are interpreted, this will be discussed in more detail.

3 MOCADI Simulations

For the simulations of the nuclear reaction and the related two-body kinematics in the storage ring environment, occurring during the experiments, a Monte-Carlo code called MOCADI, developed at GSI was used [47, 48]. The simulations involved modeling the distribution of the reaction products of ^{118}Te(p,x) and ^{124}Xe(p,x) at ion beam energies of 6 MeV/u and 7 MeV/u. Additionally, the new scraping setup that has been tested was included into the simulations.

MOCADI is a tool to simulate trajectories of ions in electromagnetic fields and materials. A key aspect of the simulations was to study the trajectory of the various reaction products in the ring. An external script, performing two body reactions, was used as to generate the reactions. Elastic scattering, proton capture and (p,n) reactions were started at the position of the hydrogen gas jet. The MOCADI code was then used to track the reaction products first through the quadrupol and then through the first part of the dipole to the detector position. The (p,n) reaction was only simulated for the ^{124}Xe runs and not for the ^{118}Te, because the ^{118}Te experiment was only executed below the (p,n) energy threshold of 7.57 MeV.

Each reaction channel was simulated separately, due to the included two-body kinematics. The distribution of the reaction products can be extracted at various positions along its trajectory. In order to obtain a realistic estimate of what can be expected on the detector, the reaction products, that have been simulated individually, can be combined in a final plot.

In Figure 3.1 the spacial distribution of the ^{118}Te(p,γ) reaction products is shown at three different positions. It is at the target region, after passing through the quadrupole magnets and at the position of the detector. The scale is given in centimeters. Negative values are describing positions closer to the center of the ring in x or below the stored beam orbit in y.

Proton capture on ^{118}Te leads to ^{119}I. At the target region, this reaction takes place. The number of reactions was set to 100000. The position of the beam is focused at the center at the beginning of the simulations. After the target section the reaction products drift along the beam axis, which reveals the kinematic

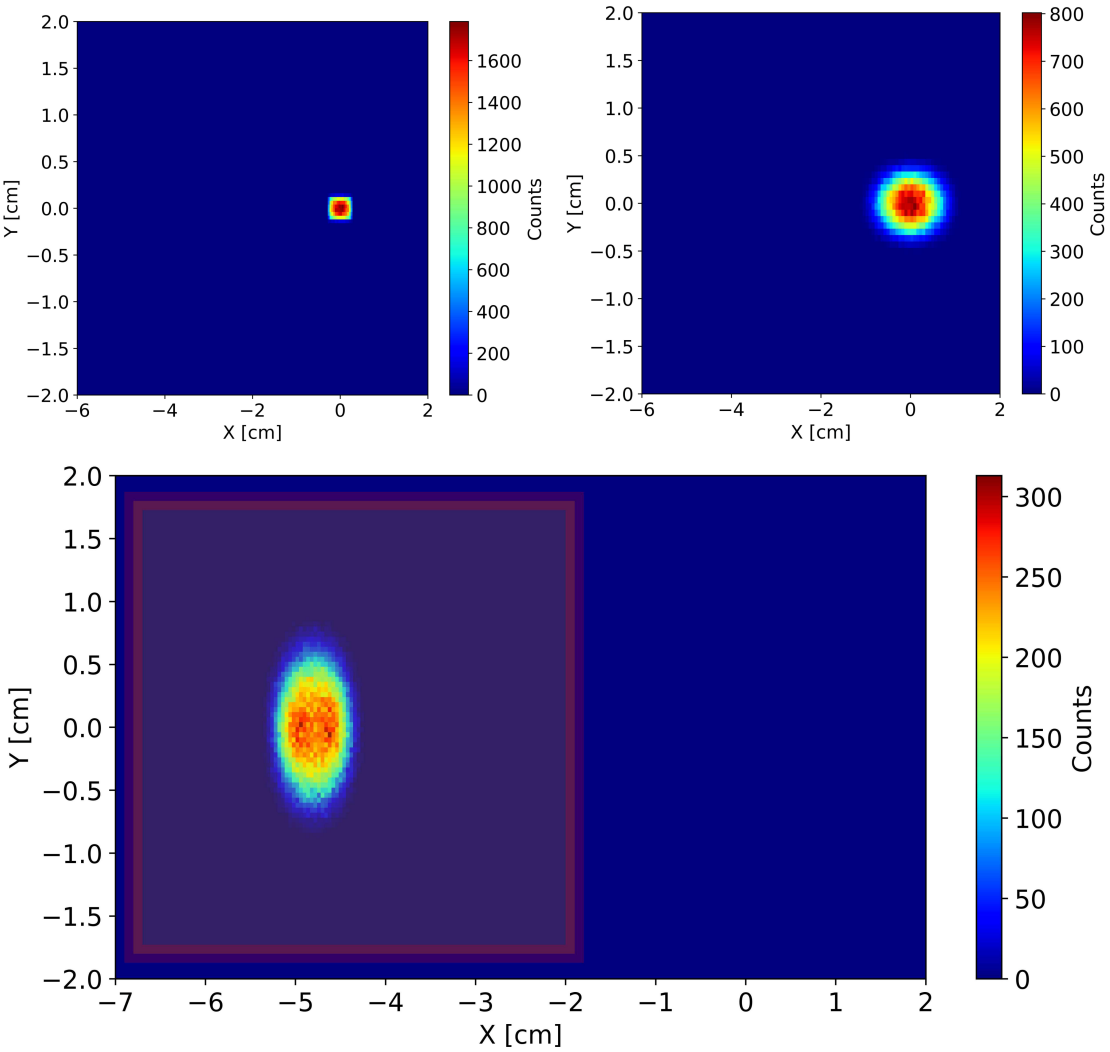

Figure 3.1: Simulations of the (p,γ) peak at the target region, before entering the dipole magnet and at the detector position (clockwise from top left). The detector position is marked in the lower plot by a red frame.

broadening resulting in a cone of reaction products. In the top right image of Figure 3.1, the reaction products have already traveled a distance of around 6.6 m from the target.

The quadrupole magnets alternate between focusing and defocusing of the beam. In the first magnet the focusing takes place in the horizontal direction (x) and in the subsequent magnet in the vertical direction (y). After around 8.15 m the reac-

tion products enter the dipole magnet. They undergo bending towards the inner side, causing their simulated positions to be represented as negative values on the x-axis. The distribution becomes symmetric in both the x- and y-directions upon entering the dipole magnet. However, due to the image scaling in the lower panel of Figure 3.1, this symmetry appears as an elongation in the y-direction. Additionally, the detector has been positioned at a tilt of about 45° within the ESR setup. Thus, the shape of the simulated peaks has to be modified accordingly to match the experimental data. The distribution of the beam profile contains information about its behavior at different stages of the experiment.

In order to establish a connection between the simulations and the analysis of the experiment, particular focus is placed on the simulations at the detector position. Therefore, it is also relevant to identify the position of the detector in the simulation. The lower image in Figure 3.1 shows in red the active area covered by the detector within the simulation. For the following plots only the region of the detector will be shown. To ensure a coherent comparison between the simulation and the experimental data, some adjustments of the simulated spectra where made. First, the values presented in the plots are converted to positive ranges. Moreover, a stretching by a factor of $\sqrt{2}$ of the y-axes is used. This approach is done due to the 45° tilt of the detector.

(p,γ) peak

Figure 3.2 shows the simulated (p, γ) peak in the detector region in 3D. The area of the (p,γ) peak only covers a small region. This is due to the fact, that the emitted γ-rays carry only very small momentum compared to the beam and heavy reaction products.

Image b) in Figure 3.2 shows the (p,γ) peak if the simulation includes only a single ground state transition. The resulting shape of the peak is very different than the experimental data. From the general shape of photon-strength functions it is known that ground state transitions at such high excitation energies as in the present case are unlikely and mainly transitions resulting in two- to three-step γ cascades will occur. Figure 3.2 a) included γ cascades with multiplicity 3. This simulation describes the experimentally observed peak form. The simulations do not include a realistic representation of gamma cascades for ^{119}I, which would need full knowledge of the nuclear structure of ^{119}I. However, this is in this case not necessary as the peak is not sensitive to details of the cascade.

The (p,γ) peak in Figure 3.2 can be described by a two-dimensional Gaussian in good approximation. In order to determine the number of the counts from

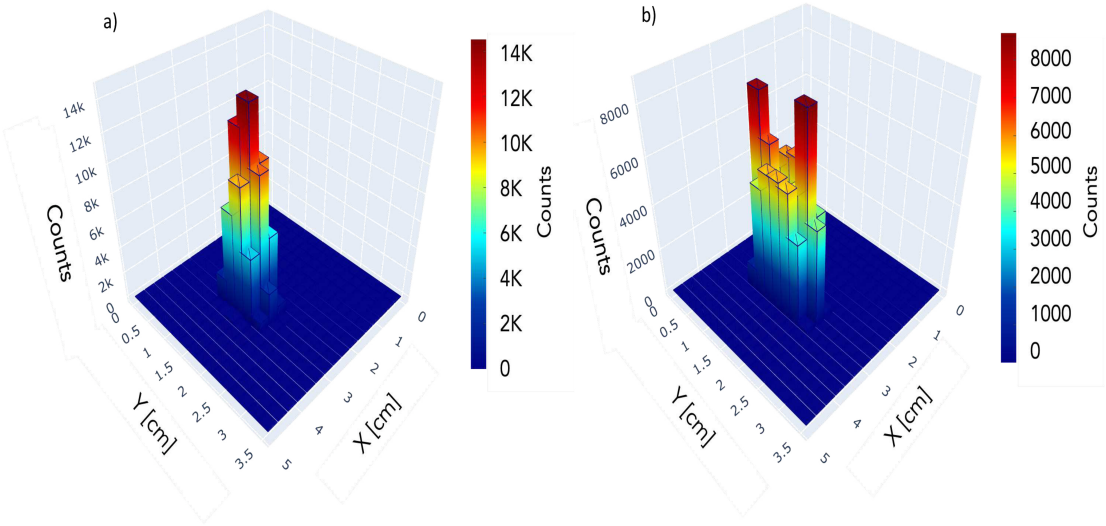

Figure 3.2: Simulation of the (p,γ) peak of a proton capture in ^{118}Te at 7 MeV/u. Image a) shows a simulation of the (p,γ) peak that includes 3 γ cascades. Image b) shows the (p,γ) peak with a transition to the ground state without γ cascades.

experimental data later on the peak will be integrated, but for the description of the background by a fit, the (p,γ) peak will be described by this approximation. The simulations of the peak have been additionally used to determine the relative position and kinematically allowed area of the (p,γ) peak. For the final analysis this region will be used to integrate the data in order to determine the number of counts.

Rutherford scattering

Figure 3.3 shows the simulated Rutherford scattering background in addition to the imulated (p,γ) reaction products for ^{118}Te at 7 MeV/u at the position of the detector. The ions that undergo Rutherford scattering at the target region hit the detector. A more detailed explanation of the formation of the Rutherford background was given in section 2.5.1.

Before combining the two seperately simulated processes the simulation output of the Rutherford background has been weighted. The simulations do not include the angular dependency of the cross section. Thus, this has to be done in a separate

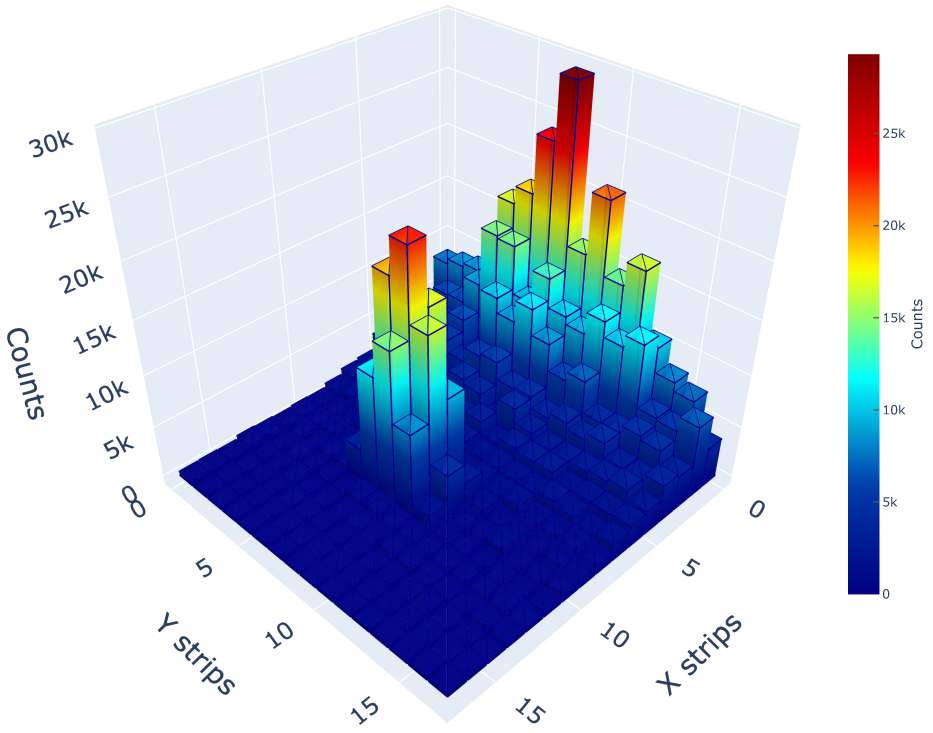

Figure 3.3: Simulation of the Rutherford background combined with the simulated (p,γ) peak for ^{118}Te at 7 MeV/u.

step. The following equation shows the dependence of the Rutherford cross section on the scattering angle and the kinetic energy

$$\sigma_{Rutherford} \propto \frac{1}{E_{kin}^2 \cdot \sin^4(\vartheta/2)} \tag{3.1}$$

- $\sigma_{Rutherford}$ = Rutherford cross section
- E_{kin} = kinetic energy of the ions
- ϑ = scattering angle.

The Rutherford scattering causes a background in the region of the peak. For the analysis this means, that in order to determine the number of counts in the peak it has to be estimated which counts are background and which can be counted as (p,γ) events.

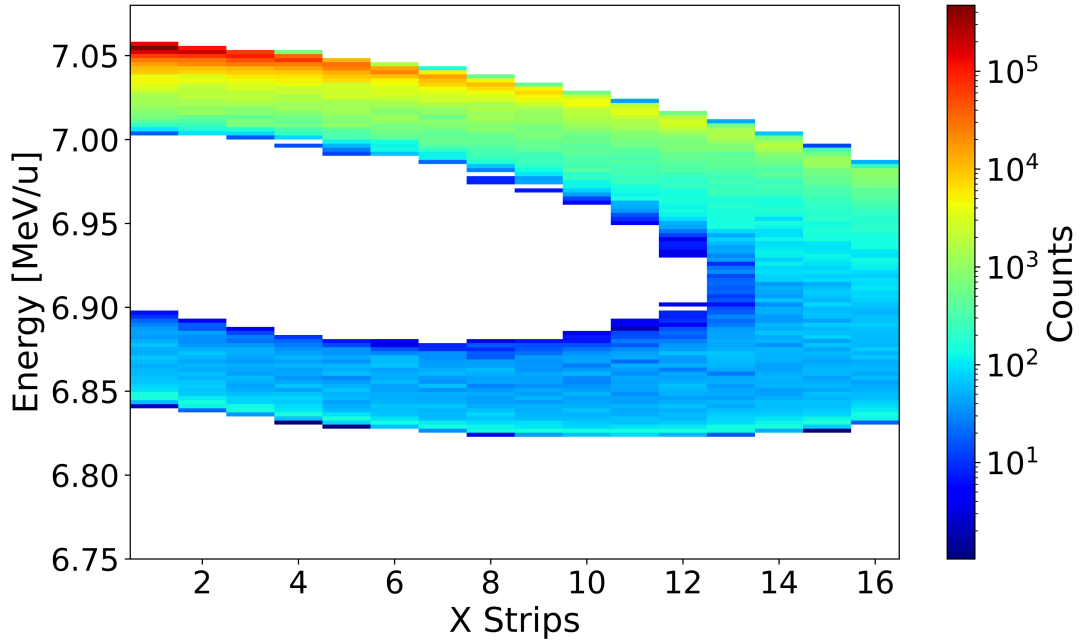

Figure 3.4: Simulation of the Rutherford background, ion energy vs. horizontal position (x).

As introduced in chapter 2.5.1 the background contribution caused by Rutherford scattering at the target consist of events that can be related to forward or backward scattering in the center of mass. To differentiate between the forward and backward scattered ions in one strip of the detector, the deposited energy needs to be considered. The ions that have been scattered forward deposite more energy than the backward scattered ions. Fig. 3.4 displays the forward and backward scattering, by plotting ion energy vs. horizontal position (x).

Following from the explanations in chapter 2.5.1. The distribution of the scattering products can be assumed to be spherical. On the detector, this would mean that a circular filled surface should be visible. However, the simulations show a ring-like structure. This can be explained with the reaction kinematics. The upper and lower parts of the scattered particles from the sphere are cut off and therefore do not land on the detector. This significant structure helps to determine the position of the detector when comparing the experimental data with the simulations. Additionally, it can be used for energy calibration. Image b) of Figure 3.5 shows the measured data from the experiment with the ^{124}Xe beam at 7 MeV/u. Image a) shows the corresponding MOCADI simulations. The image includes the

Rutherford simulation and the (p,γ) and (p,n) reaction products. The simulations describe the experimental data. In the region of the (p,γ) peak a background contribution of the Rutherford scattering is given, which can not be fully discriminated by ion energy and/or position cuts. Thus, it has to be modelled to obtain the pure peak content.

Simulation of the background reduction

To reduce background, induced by Rutherford scattering, a scraper was developed [37]. Images c) and e) of Figure 3.5 show the by MOCADI simulated effect of the scraper. Image c) displays the ion energy over x and image e) shows the position plot. For these simulations, the same setup for the MOCADI simulations has been used as for image a), but after the simulation an extra condition has been applied to the simulation output: Particles that pass the position of the scraper are omitted for analysis of the ion distribution in the detector plane. As a result of this modified simulation, the (p,γ) peak is background free in the energy over x plot in Figure 3.5 c). Additionally, the (p,n) peak can be seen. This means that at the target region a proton was captured but instead of a γ a neutron has been emitted. In the data without the scraper the (p,n) distribution is completely concealed by Rutherford scattering. This shows the benefits of the usage of the scraper. For the measurements with the ^{118}Te beam no (p,n) peak is expected. The energies at which ^{118}Te has been measured are below the (p,n) reaction threshold of 7.57 MeV.

The images d) and f) of Figure 3.5 shows the experimental data of ^{124}Xe at 7 MeV/u with the usage of the scraper, once in ion energy over x and for f) in the position plot. The (p,γ) peak and the (p,n) peak are clearly visible compared to the upper right plot. In contrast to the simulations, the scraper did not remove the background completely. There have to be effects causing this additional background in the region of the peaks that have not been considered in the simulations. One possible explanation is a secondary scattering of the particles at the scraper edge.

Cross section determination

In previous experiments without the scraping technique the background in the region of the peaks has been described successfully with the MOCADI simulations. Thus, it has been used for the final determination of the cross section.

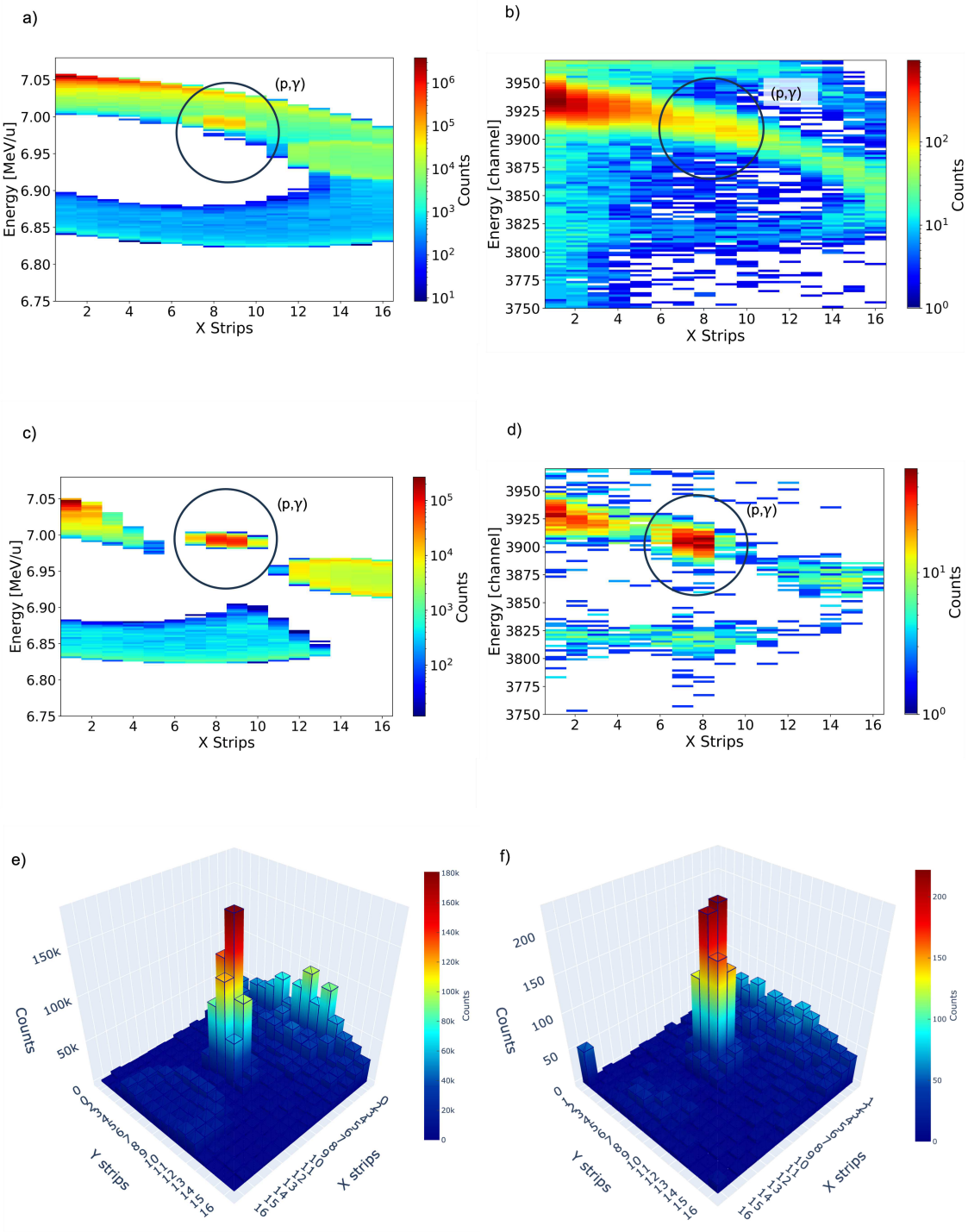

Figure 3.5: Simulations and experimental data of ^{124}Xe at 7 MeV/u with and without the scraper. Image a) shows the simulations of ^{124}Xe (p,γ), (p,n) and Rutherford combined without the scraper. Images c) and e) show the same simulation, but with a scraper. The images b), d) and f) show the experimental data taken with and without the scraper.

This experiment employs the scraper technique for the first time and the comparison of simulation and experimental data shows, that the MOCADI simulations underestimate the background in the region of the (p,γ) peak, see Figure 3.5.

Within the framework of this thesis the cross section has also been estimated based on simulations. The resulting cross sections are higher than the cross sections obtained with different analysis methods. This corresponds to the observation, that the background is underestimated. Thus for the final cross section determination in this thesis the simulations will not be used.

4 Analysis

The focus of the following chapter will be the analysis of the recorded data during the beam time. The previous chapter gave already important information about the expected data in the DSSSD. Based on the simulations, the DSSSD data are going to be interpreted and discussed in more detail.

4.1 Data selection

In order to create the desired conditions for these measurements, a complex setup is required in the ESR. During this measurement campaign, the data have been collected under different sets of experimental conditions. All settings are permanently monitored and mostly stored with the data.

For the selection the stability of the beam current and target density was checked. Additionally, also the electron cooling has to be stable all the time for a setup, as the electron cooling ensures a measurement at a constant energy, as introduced in section 2.2.1. Data that show instabilities within this monitoring have not been included in the analysis. Also, the high voltage and leakage of the DSSSD and of the HPGe-detectors were monitored.

Before the analysis it needs to be examined that the data selected are only from the phase during which the target was on. It should not include parts from the injections, deceleration of the ions or miss relevant parts.

4.2 Silicon detector hits treatment

The DSSSD was used to detect the reaction products of the proton capture with spatial resolution and determine their energy. Each channel of the DSSSD was read out individually. As for each ion hit the deposited energy is measured by one x- and one y-strip of the detector, a linear correlation between the signals on

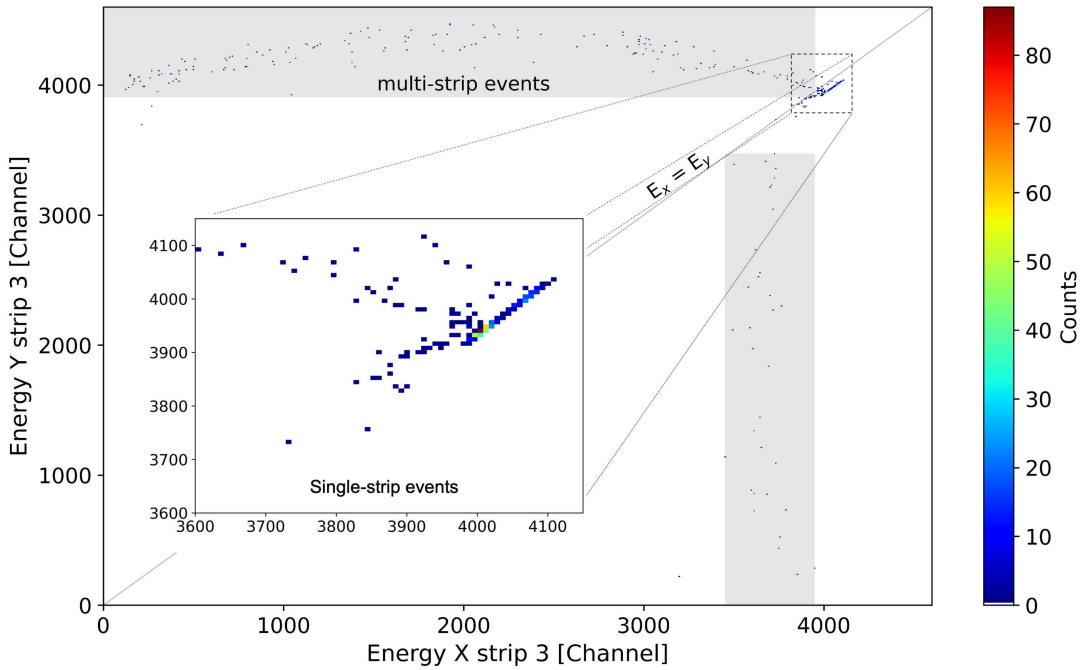

Figure 4.1: Deposited energy of the third x and the third y strip. The events that deposit the same energy on both sides of the detector are placed on the diagonal.

the x and y strips is expected. In chapter 2.3.3 a more detailed description of the detector is provided.

Figure 4.1 shows exemplary the registered ion energies for x strip number 3 vs. y strip number 3. The entries on the diagonal of this plot will be called single strip events. In this case the full energy is deposited coincidentally in only one strip per detector side with a strip on the other side of the detector. The other entries, where more than one strip at least on one side of the detector was hit, will be called multi-strip events. In general the detection efficiency of the particles can be assumed to be 100%, as they are completely stopped in the detector material.

In this analysis two approaches were chosen. For one, all events were used and an efficiency of 100% was assumed. In the second approach, only events that have deposited their entire energy in one pixel of the DSSSD were considered. This means that the x strip and y strip that measured this event have detected the same energy. The likelihood for these events is almost 100%, however if the heavy ions deposit their energy in the small gaps between the strips, their energy is dis-

tributed over several strips. These events will be called multi-strip events.

Figure 4.2 a) shows all strips of the DSSSD. The measured energies do not match with each other. Thus, they can not be compared. Instead, the analysis must be based on an intrinsic calibration matching. This calibration will be discussed in more detail in the following section.

4.2.1 Intrinsic calibration

For the intrinsic matching of the DSSSD a calibration among the individual channels is necessary. The signals appearing in both sides of the detector need to be aligned. If consistency is achieved between the ion energies measured with all strips within the DSSSD, a relative energy calibration is achieved. The intrinsic calibration method used here is applied from reference [49]. It is based on a linear correlation between the responses of the x and y strips, a premise that holds for single strip events but is not applicable to multi-strip interactions. Figure 4.2 a) shows the relation of the deposited energy of all combinations of x and y strips (for all pixels of the detector).

The signal amplitude measured in coincidence between a x- and a y-strip shows an individual linear correlation. These correlations of ion energies differs for each combination of strips. These differences can originate from slight variations in charge collection, signal transport and electronic treatment from strip to strip. The goal of the intrinsic calibration is to be able to compare the energies measured in different strips. For this calibration the single-strip events, lying on the diagonal in Figure 4.1, have been used. Thus, a data set with sufficient statistics and full area detector irradiation is needed. The only data set providing such conditions is the ^{124}Xe measurement at 7 MeV/u without the scraper, as it has the highest statistics for single-strip events and Rutherford scattering facilitates full irradiation of the detector. After a successful calibration it should be possible to describe all single strip events by the same diagonal.

The initial assumption of the calibration is that the deposited energy E measured in channel i can be proportionally assigned to a signal of amplitude A in channel i, where i in this case corresponds to either an x or a y strip:

$$E_i = s_i \cdot A_i \tag{4.1}$$

- E_i = deposited energy in channel i,
- s_i = slope factor for channel i,
- A_i = amplitude in channel i.

The amplitude of this channel has the highest amplitude among all strips on the same side. The slope factor is the calibration coefficient. For each event registered on the x side there is a corresponding event expected on the y side. The corresponding signals are thus correlated and it is assumed that

$$E_x = E_y. \tag{4.2}$$

This corresponds to the signals lying on a diagonal line in Figure 4.1. Consequently, the following relationship exists between the measured amplitudes of the two channels

$$A_x = S_{xy} \cdot A_y. \tag{4.3}$$

The slope S_{xy} can be determined experimentally for each pixel. S_{xy} equals, following the equations before s_x/s_y. Also, the uncertainty, ΔS_{xy}, can be determined experimentally.

For all combinations a best set of measured slopes S_{xy} can be estimated. Chi-square minimization can be used to determine the best set of slopes.

$$\chi^2 = \sum_{x,y} \left(\frac{S_{xy} - s_x/s_y}{\Delta S_{xy}} \right)^2 \tag{4.4}$$

The strips are calibrated relative to each other, thus an arbitrary reference has been chosen, $s_{x=1} = 1$.

After calibration, the comparison of all x and y strips results in Figure 4.2 b), which demonstrates that the matching worked very well.

By subtracting the energy of single-strip events of the x and y strips after the calibration it results in a histogram that provides the energy resolution. The width of the peak gives an energy resolution of ΔE = $\pm$10 channels. With a successful calibration the experimentally determined data can now be analyzed and interpreted in further detail. The parameters resulting from this calibration have been applied to all data sets of ^{124}Xe and ^{118}Te, with and without the scraper.

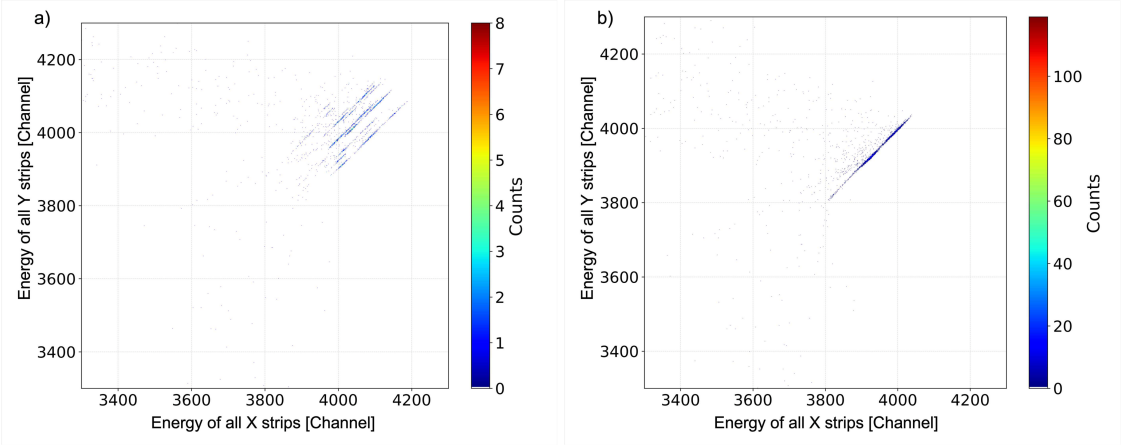

Figure 4.2: Image a) shows the individual energy correlations between front- and back-side signals for single-strip events of each pixel before calibration. Image b) shows how the intrinsic calibration matches these energy correlations and makes them directly comparable.

4.2.2 Energy deposition in the DSSSD

In chapter 3 the different energy depositions of the measured particles in the DSSSD have already been introduced. In the following, the signature of different heavy ion reaction products in one dimensional histograms of individual strips are discussed.

Energy signature of the Rutherford background

As described in chapter 2.5.1 not only proton capture takes place at the target, but also a Rutherford scattering of the ions. This should be visible as two peaks in the energy spectrum of a pixel. One peak at higher energy and a second one, at lower energy, corresponding to forward and backward scattering, respectively. The energy of the reaction products of the proton capture is in the same range as that of the forward scattered particles. In the energy plot, therefore, a distinction between (p,γ) peak and scattering is not straightforward. During the analysis of the spectra of the individual strips of the DSSSD, a third peak appeared in addition to the two expected peaks.

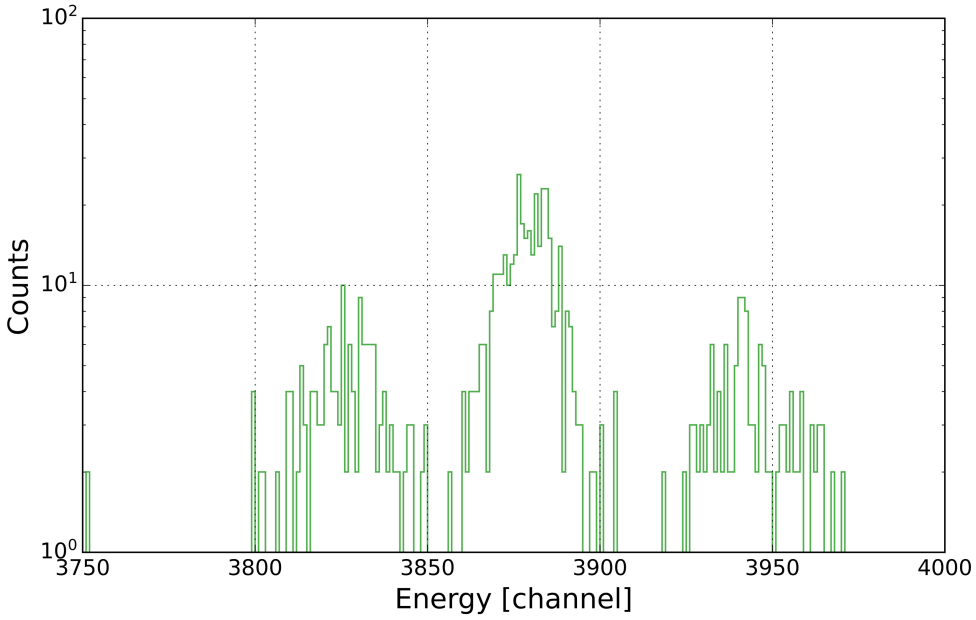

Figure 4.3: Spectrum of the 14$^{\text{th}}$ x strip of the DSSSD for the recorded ^{124}Xe data at 7 MeV/u, showing three peaks.

4.2.3 Triple peak problem

The analysis of the energy spectra recorded for both, the xenon and the tellurium beams have shown the presence of three peaks. The third peak consistently appeared in the spectra regardless of whether the scraper was used in the experimental setup or not. Since the scraper was not used for one set of xenon runs, this measurement provides higher statistics. Consequently, for an analysis with more statistics of the third peak, the xenon data set was chosen.

To illustrate these findings the energy spectra originating from 16 x and 16 y strips within the Double-Sided Silicon Strip Detector can be used. In Appendix A the spectra of the 16 x strips can be found. These spectra are numbered from 1 to 16. This corresponds to the vertical positioning of the strips, starting closest to the particle beam. The intensity distribution of the various peaks within each strip shows considerable variation. Of particular interest is the 14$^{\text{th}}$ spectrum, where the three peaks are particularly clear. This spectrum is shown in Figure 4.3.

Rutherford scattered ions (backward and forward) and proton capture products enter the detector with 3 different energies. However, in particular for the scattered

events, this energy depends also on the position on the detector because of the reaction kinematics. To gain a more precise understanding of the energy distribution and to achieve a statistically robust assessment, the strip numbers in geometric order were plotted against their respective energy values. Figure 4.4a) illustrates this analysis for the y strips, while Figure 4.4b) presents the corresponding plots for the x strips. These plots serve as essential tools for disentangling the reactions that lead to the different energy depositions within the DSSSD. Additionally a projection on the y axis is shown. This projection makes it easier to apply cuts. The differently grey shaded areas in this plot sketch roughly the range of channels that each of these peaks covers.

In Figure 4.4b), an energy distribution over the x axes is obtained, similar to what has been expected from the simulations, except for the unexpected contribution. According to the simulations, in the position-energy phase space a ring-like distribution is expected as a result of the scattering process. However, since the detector only covers a part of the distribution of the scattered particles, only around half of the structure is visible.

The proton-capture events are part of this structure as they cover the same energy range as the forward Rutherford scattering. Thus, by the kinematic relation from the simulation the Rutherford forward and backward scattering can be identified. In addition to this anticipated half-circle structure, a third energy structure is also evident. It shows a similar curve like the forward scattering of the Rutherford but it does not seem to have a backward scattering component in its distribution. Moreover, the distribution lies at energies above the forward scattering distribution of the Rutherford.

These observations raise the question of the origin of the additional distribution. To address this, a preliminary approach is taken to identify the position of the third peak. Instead of filling all events into the position plot, the focus is on filling the counts that can be attributed to the peak. To achieve this, energy cuts were applied to the spectra from Figure 4.4a). Subsequently, the position plots were filled exclusively with the signals within the energy cuts.

Figure 4.5a) presents a position plot that has been filled exclusively with the events of energies originating from the central peak of the three projected peaks on the y axis projection in Figure 4.4a).

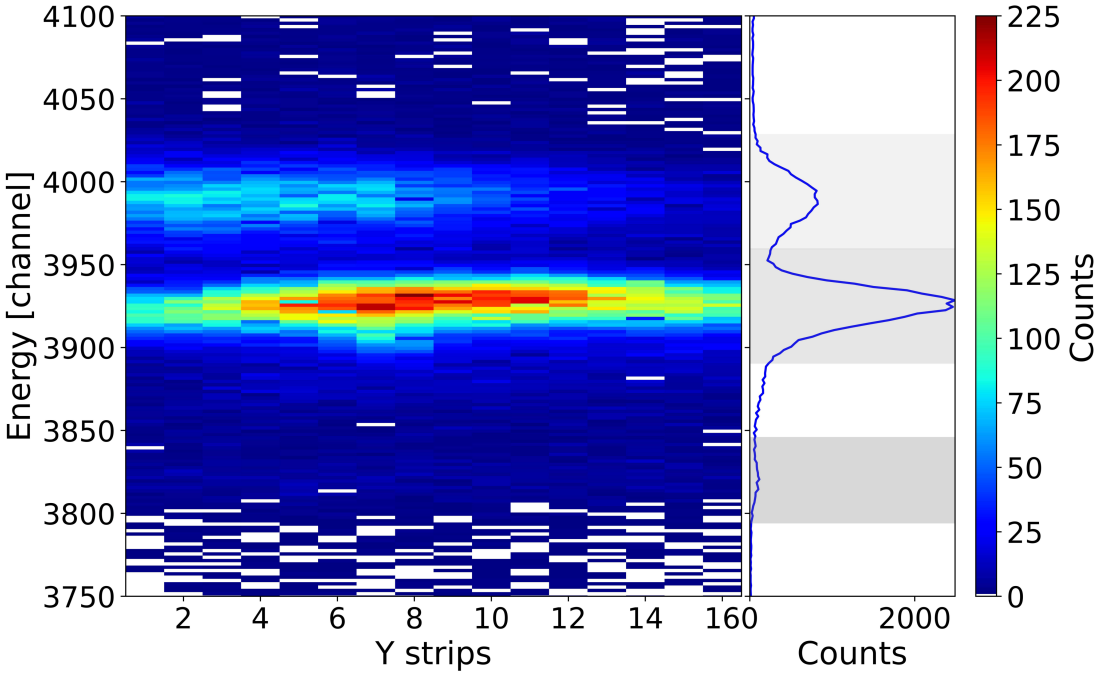

(a) Spectrum of the 16 y strips of the DSSSD, plotted against their energy. The data were obtained with ^{124}Xe at 7 MeV/u.

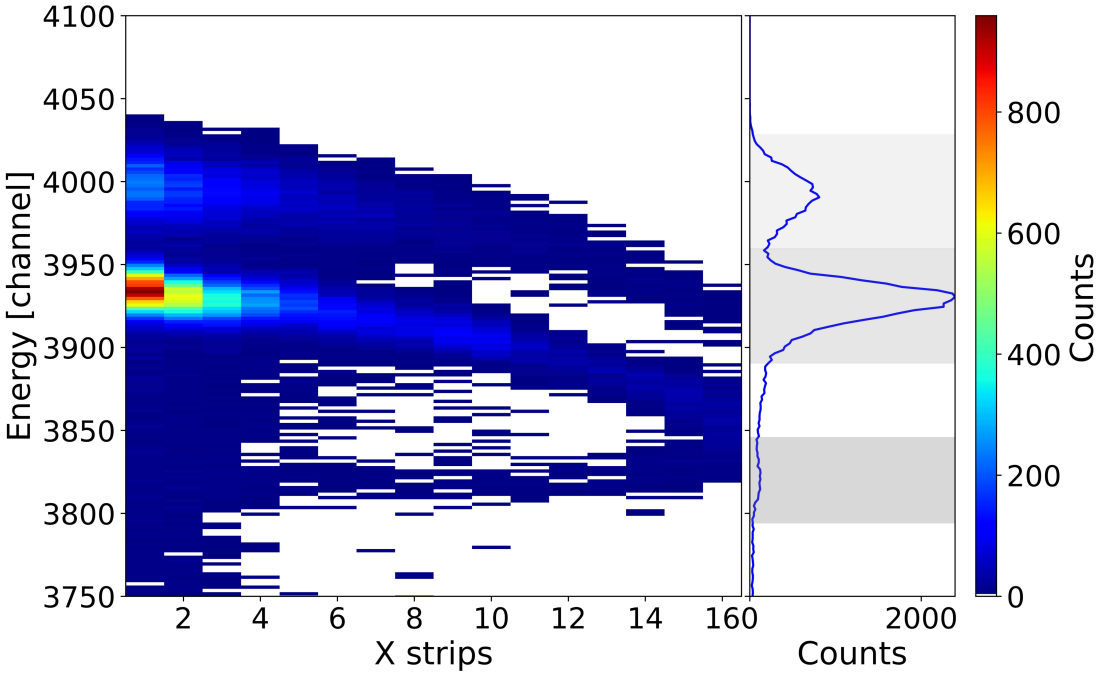

(b) Spectrum of the 16 x strips of the DSSSD, plotted against their energy. The data were obtained with ^{124}Xe at 7 MeV/u.

Figure 4.4: Spectra of the 16 x and y strips plotted over their energy.

Figure 4.5a) shows counts within the region that aligns with the expected characteristics of Rutherford scattering. In addition to forward scattering, this component also contributes to the region of the (p,γ) peak. This agrees with the simulations, as the counts of forward scattering and the (p,γ) peak are expected to be in the same energy region and that they can only be disentangled based on the position plot.

The events of the unknown distribution are visualized in Figure 4.5b. It shows the a simillar behavior associated with scattering. However, no (p,γ) peak is visible in the data. The absence of the (p,γ)-peak suggests that these counts have no influence on the analysis of the (p,γ) peak. Instead, it appears to be an additional background component, outside of the (p,γ) peak. This also excludes the possibility that the distribution is due to an electronic effect that leads to a copy of the known distribution. If this had been the case, the copy would then also contain the (p,γ)-peak. Moreover, the distribution shows a horizontal downward shift on the position plot.

The origin of this background seems to be an independent process. One of the most notable discrepancies is the fact that this unidentified peak appears to have a higher energy than that of the Rutherford forward scattering. This raises a problem due to the fact, that the energy of forward scattering should be close to the energy of the primary beam itself. This means that the counts of the third peak would have a higher energy than the primary beam.

One potential explanation might be considering the presence of another isotope in the ESR that could have this energy. However, the third peak, is not only evident in the tellurium data, but it also appears in the xenon data. It is unlikely that for both beams another isotope was part of the beam, that shows the same energy shift. During the beam time with the usage of the Schottky mass spectrometry it could already been ruled out that another isotope was stored. The cooled ions can be identified by the Schottky mass spectrometry based on their specific mass to charge ratio [50]. Additionally, also the X-ray spectra taken during the beam time, only show X-rays that can be identified to either ^{124}Xe or ^{118}Te, as shown in section 2.4.4.

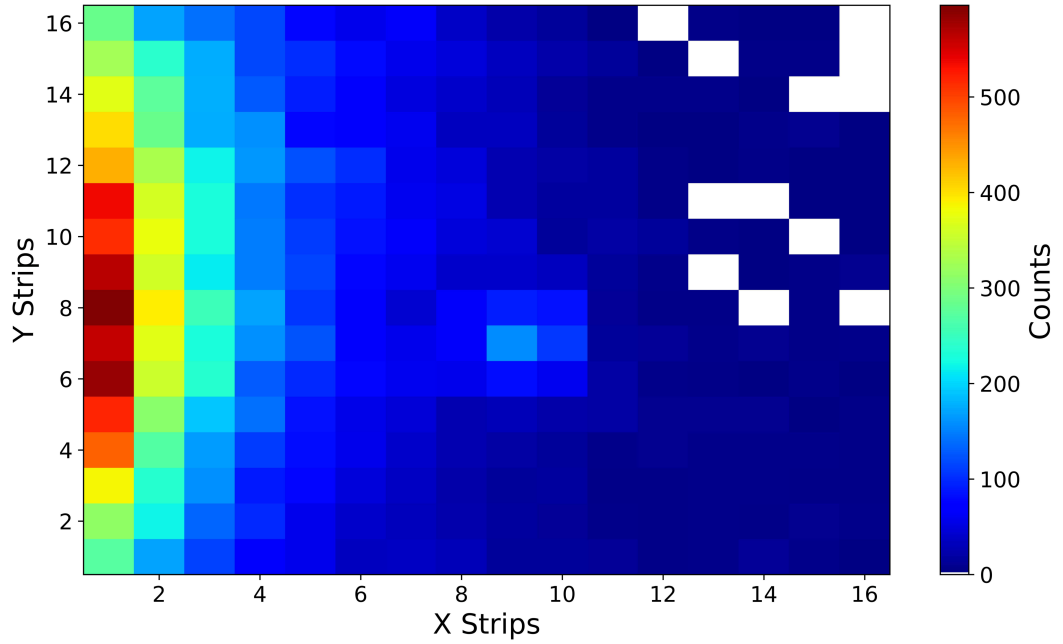

(a) Position plot of the DSSSD filled only with the counts of the energies originating from the central peak. The data were obtained with ^{124}Xe at 7 MeV/u.

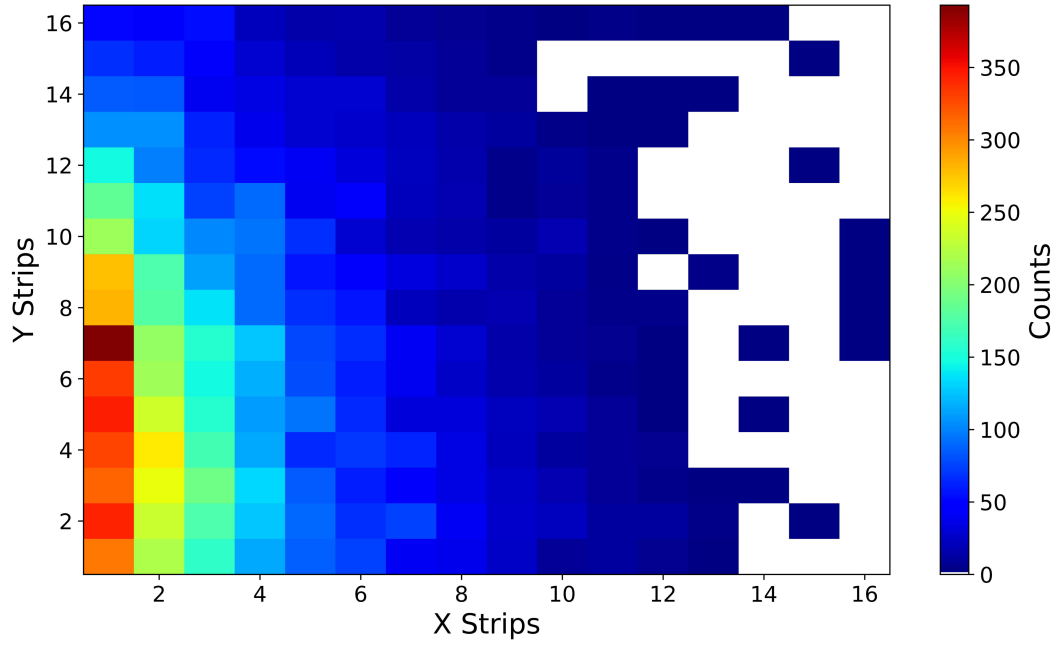

(b) Position plot of the DSSSD filled only with the counts of the highest energy of the three peaks. The data were obtained with ^{124}Xe at 7 MeV/u.

Figure 4.5: Position plots of the DSSSD, filled with events after applying different energy cuts.

Adding to the complexity of the question of the origin of this peak is the deflection towards lower horizontal positions. According to our understanding of the behavior of particles within the ESR, there is no mechansim to deflect particles downwards. The dipole magnets only create a horizontal deflection. The quadrupoles symmetrically focus and defocus around the beam axis.

One possible explanation could be a detection outside the measurement period. Within the measurement period given by the trigger signals, when the target is switched on and off, the measurement conditions are known. Outside this period the beam is strongly modified. Especially at the beginning, after the injection of the radioactive particles, when the beam is not yet cooled, the beam is very large and could therefore hit undefined regions of the detector. For this it is necessary to check that the measurement is done in the time frame set by the triggers. For this purpose the xenon data measured at 7 MeV/u were used again to get sufficient statistics.

In the context of this experimental setup, every recorded event is associated with a timestamp. This timestamp provides temporal information to the data. The whole measurement for this setup extends over several hours, consisting of the sum of measurement cycles that each consists of various measurement phases. Each phase has a distinct purpose in the experiment.

First, there are the initial phases characterized by multiple injections from the Fragment Separator. The injected beam thus reaches a high intensity at high energies. After these phases, the beam is tuned to achieve the desired experimental conditions. After the beam accumulation it is decelerated and continuously cooled by the electron cooler. When the target is turned on the trigger signal target ON is send to the DAQ. The measurement is recorded between this trigger signal and the target OFF signal ensuring the required conditions for the experiment. Measuring the data within these trigger signals ensures that the measurements have been conducted under ideal conditions.

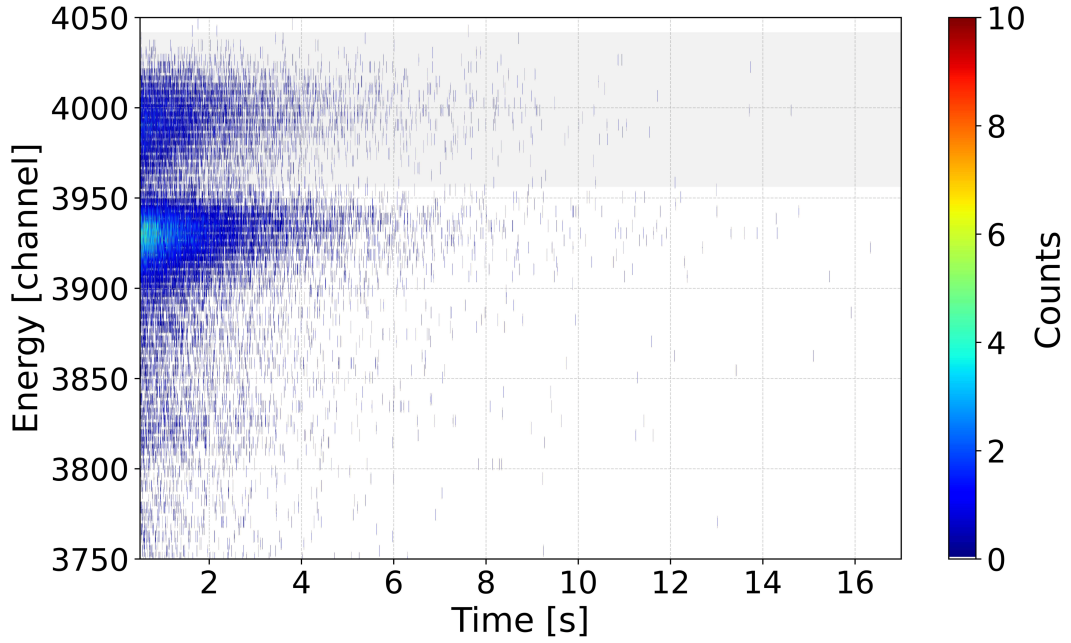

(a) Energy over time, after the trigger signal target On, for the sum of all y strips. The data were taken during the ^{124}Xe at 7 MeV/u measurements. In light gray the region of the unknown component is marked.

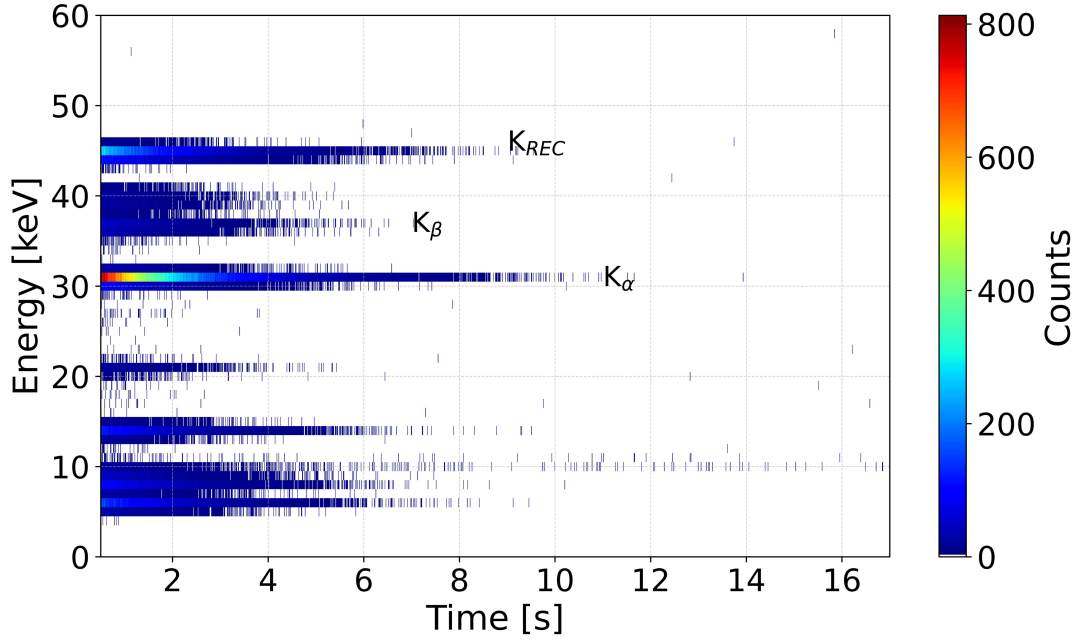

(b) Energy over time, after the trigger signal target On, for the X-ray detector in the first seconds after the target was turned on. The data were taken during the ^{124}Xe at 7 MeV/u measurements.

Figure 4.6: Energy over time for the events in the DSSSD and the X-ray detector at 90°.

Figure 4.6a provides an overview of the distribution of events plotted with their energies over time. The area covered in light gray shows the region of the unknown component. The majority of counts are concentrated at the onset of the measurement period when the target is initially switched on. As time progresses, the count rate gradually decreases. This decrease can be attributed to the diminishing intensity of the beam over time. As reactions take place, fewer particles remain available for further interactions, resulting in a decline in the overall count rate. The three distinct peaks remain separated from each other throughout the duration of the measurement. And most notably, no difference of the three components in time dependence can be observed. All three peaks are decaying with a similar decay constant. There does not seem to be an unexpected time structure underlying the unknown component. It seems to happen continuously, just as the other components.

To verify this decay constant a comparison was made with the time evolution of the recorded X-ray data, as shown in Figure 4.6b. This additional plot serves as a cross-check, confirming that the temporal behavior is consistent. All components follow a nearly identical decay constant at the different energies.

Influence of the deadlayer

The position of the unknown events on the position plot could lead to the assumption that they hit the detector on a different trajectory. If a part of the beam enters under a different angle into the detector it could have a shorter path through the deadlayer of the detector, as the detector is tilted. This could lead to a possible explanation of the higher energy, because of a smaller energy loss inside the deadlayer, as the way through the deadlayer is shorter for particles hitting under an angle perpendicular to the detector, compared to the ones on the beam axis.

The influence of the difference in the way through the deadlayer has been investigated. The maximum difference in distance of the paths of the particle through the deadlayer can be estimated to be around 124 nm which would lead to a difference in energy loss of around 0.02 MeV/u. The difference of energy between the peaks is 0.08 MeV/u. Thus, the energy of the third peak can not be explained by particles with a shorter path through the deadlayer.

Influence on the (p,γ) peak

The unknown componant can be treated as an extra background componant. It seems to have no influence on the (p,γ) peak. In addition there was no identifiable

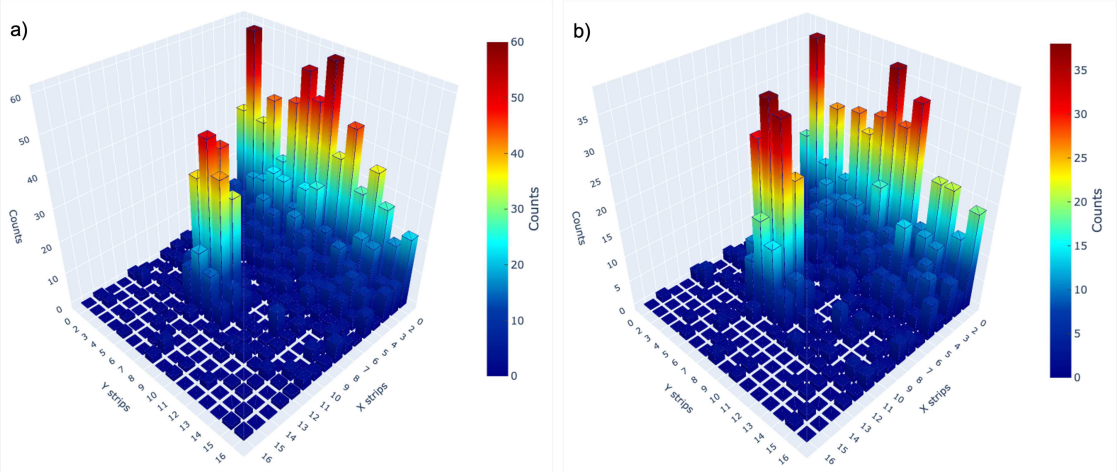

Figure 4.7: 3D position plots of ^{118}Te data at 7 MeV/u without a) and b) with energy cut.

cause or temporal correlation for the unknown component. Although the component is not fully understood it can be described and identfied as a background contribution. Thus, it is reasonable to exclude the counts associated with this energy from the further data analysis. Figure 4.7 shows the influence on the position plot of the Te data at 7 MeV/u. The number of counts within the (p,γ) peak remains consistent even after the exclusion of the counts associated with the unknown component. However, the relation between peak and background changes. This change shows an improvement in the signal background ratio.

The analysis has been performed with and without the cut. The influence on the cross section turns out to be negligible.

4.3 Cross section determination

In this chapter a detailed description of the determination of the number of counts in the (p,γ) peak will be given. This expanded discussion is relevant because of the unexpected shape of the background and the subsequent application of an additional energy cut. Given these challenges, several approaches to accurately determine the number of counts within the (p,γ) peak and to effectively distinguish them from the background were developed and compared. Two approaches will be discussed in the following sections.

4.3.1 Determination with full statistics

The first approach will be illustrated at the example of ^{118}Te at 7 MeV/u as shown in the upper plot of Figure 4.8. The scraper was used in this setup. For the analysis every registered event was included under the condition that every event is just counted once. The events could share their energy between two adjacent strips. The events were therefore assigned to the strip with the highest amplitude. Thus, the hit was always assigned to the strip that registered more than half of the energy.

In order to determine the number of counts in the peak $N_{(p,\gamma)}$ one needs to integrate over the area of the peak and subtract the background. To define the background in the area of the peak a fit for the peak and the background is needed. The statistical error is primarily given by the Poisson distribution, coming from the counting statistics. The systematic error arises from uncertainties related to the position determination and the characterization of the background in the area of the peak.

The lower plot of Figure 4.8 shows the fit for the (p,γ) peak and for the background. Two-dimensional Gaussian fits have been applied to each. From the simulations it is known that the (p,γ) peak can be approximated by a two-dimensional Gaussian fit. In the case of the background, the two-dimensional Gaussian function has its maximum located outside the visible plot. The approach for this fit function is purely phenomenological. It describes the shape of the subsurface in the area of the peak with low residuals. The first three x strips, as well as the last x strip have been excluded for the region of the fit. The strong increase of the background in the first x strips can not be explained by the fit. As this region is not relevant for the peak, it can be excluded. This function describes the background contamination that occurred in the area that should have been removed by the scraper according to the simulations.

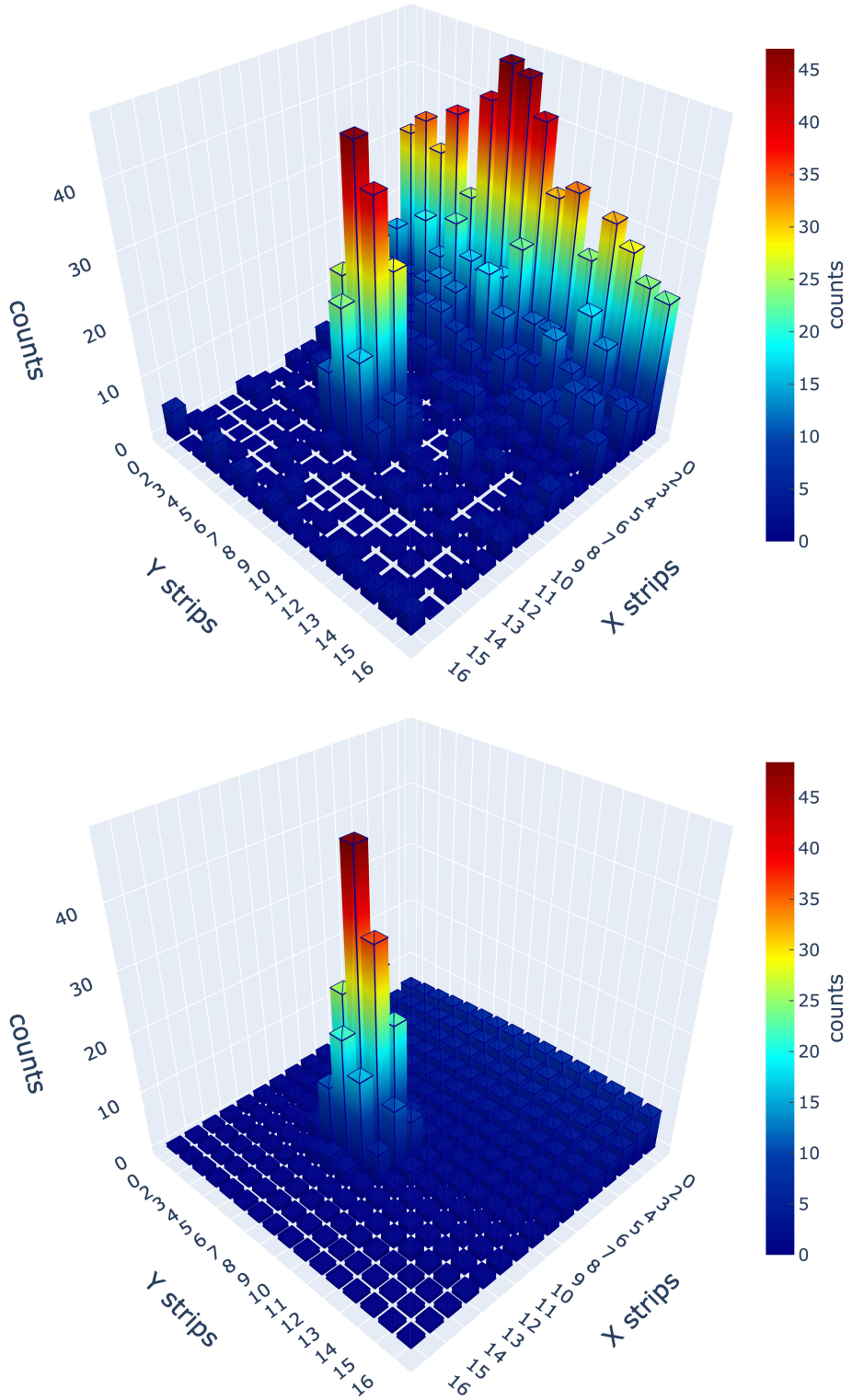

Figure 4.8: The upper figure shows a position plot of the experimental data from ^{118}Te at 7 MeV/u. In the lower figure shows the fit of the peak and the background for the ^{118}Te data.

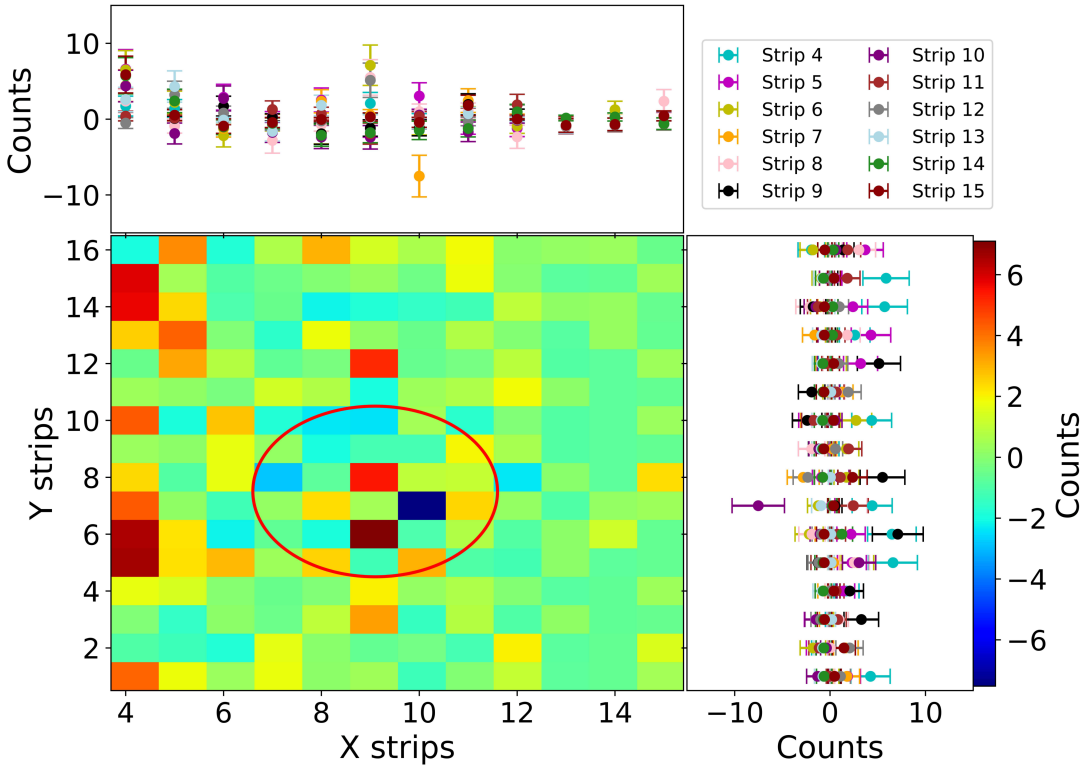

Figure 4.9: Residuals of the fit of the data of ^{118}Te(p,γ) at 7 MeV/u. The region of the (p,γ) peak that was determined with the MOCADI simulations is marked in red.

This fit can describe the shape that cannot be explained by the simulations in this area.

The residual plot displayed in Figure 4.9 shows the difference between the experimental data and the fits for the data of ^{118}Te at 7 MeV/u. With a red circle the region of the (p,γ)peak, that was determined with the MOCADI simulations, is marked. This residual plot illustrates the quality of the fits. The power of this approach can be observed as the residual plot shows fluctuations at the position of the (p,γ) peak of around zero. The projections on the x and y axis show the fluctuation with its uncertainty for every pixel. The pixels at the position of the peak show higher fluctuation as in the region around the peak. The reason for

this is, that the (p,γ) peak is not exactly a two-dimensional Gaussian. That the residual around the peak is close to zero shows that the background fit has a similar structure as the observed data, and thus can be used for a description of the background in order to determine the counts.

The first 3 strips in the residual plot showed a higher discrepancy between experimental data and the fit, because they have been excluded from the fit, as they are not relevant for the area around the peak. By integrating over the area around the peak and subsequently subtracting the fitted background the number of counts in the peak have been determined. With this approach the following cross sections at different energies could be obtained. They have been obtained once for the full energy range and once with the energy cut introduced for the unknown distribution.

In section 2.4 the efficiency, the theoretical cross section and the number of counts in the K_REC peak have been determined. With the before described approch the number of counts in the (p,γ) peak was determined. With equation 2.1 the following cross sections have been calculated:

$$\sigma_{^{124}Xe(p,\gamma)}(E = 7.05MeV) = 71 \pm 7_{stat} \pm 5_{sys}\text{mb}, \tag{4.5}$$

$$\sigma_{^{118}Te(p,\gamma)}(E = 7.05MeV) = 79 \pm 7_{stat} \pm 5_{sys}\text{mb}, \tag{4.6}$$

$$\sigma_{^{118}Te(p,\gamma)}(E = 6.044MeV) = 50 \pm 9_{stat} \pm 6_{sys}\text{mb}. \tag{4.7}$$

4.3.2 Determination with single-strip events

In the previous approach all events have been used. In the second part of the previous approach only the events with energy in the region of the unknown distribution were neglected. The idea in this approach is to analyze only the single strip events instead of all events. This means that the deposited energy has to be the same on x and y side inside the range $\Delta E = \pm$ 10 channel, as used before for the intrinsic calibration.

This approach has the advantage of clearly identifiable hits, based on the deposited energy. Later on, the number of counts will be corrected for the multi-strip events with the known ratio for the relation between single strip events and multi-strip events. The efficiency can be described with the following equation:

$$\epsilon_{ionhit} = \frac{N_{SE}}{N_{SE} + N_{ME}} \tag{4.8}$$

- ϵ_{ionhit} = efficiency of the ionhit ΔE,
- N_{SE} = number of single strip events within ΔE,
- N_{ME} = number of multi strip events.

Figure 4.10 shows the single strip events and the multi-strip events. It shows the deposited energy on the x strips vs the energy deposited on the y strips plotted on the y axis. Is shows the multi-strip events for all pixels, the region of the single-strip evens within ΔE is marked.

By applying the condition that $E_x = E_y$, within the ΔE window, the energy over position plots are better identifiable. Each ion hit should be shown at its full energy and the pure kinematic behaviour of the ion reactions products is revealed without the distortion of interstrip hit effects. This enables the application of energy cuts, which do not interfere with the content of the (p,γ) peak.

This is illustrated in Figure 4.11. The upper plot shows all events that have been detected. The energy of each hit is plotted against its x position. The three distributions are again visible. In the lower distribution the condition $E_x = E_y$, within the ΔE was applied. The three distributions are under this condition better differentiable. Before especially the distribution of the backward scattering of the Rutherford distribution was difficult to identify. This makes it possible to apply

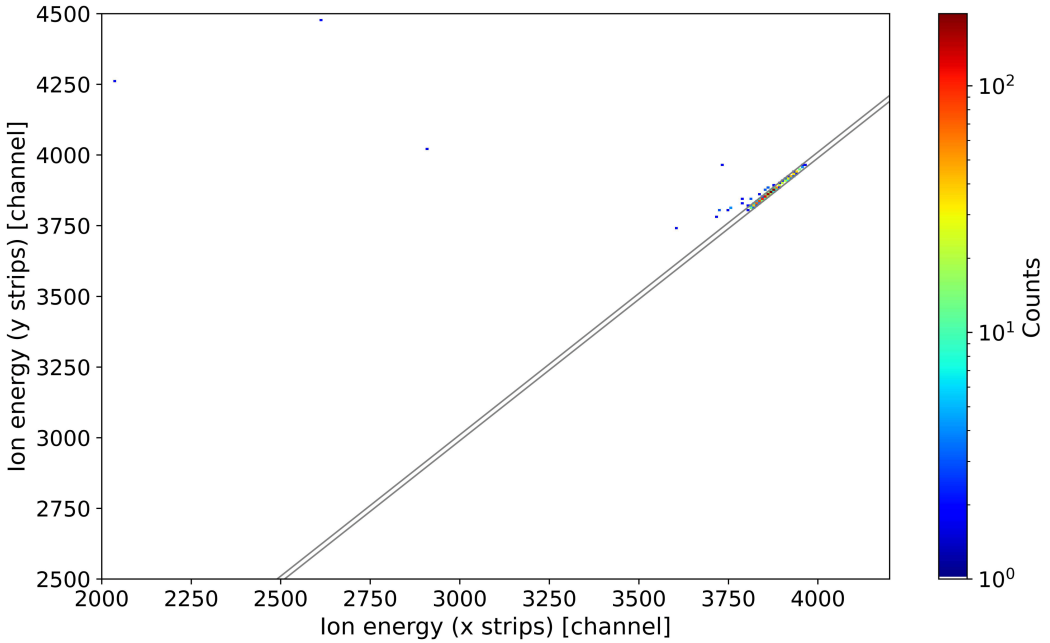

Figure 4.10: Plot of the ion energy detected in the y strips over the ion energy detected in the x strips. The single strip events and multi-strip events on the detector are shown. The region of the single strip events, defined by ΔE is marked with grey lines.

multiple energy cuts in the analysis without effecting the counts inside the (p,γ) peak and thus reducing the background.

As a first step an energy cut is set to energies above the Rutherford forward scattering component and the (p,γ) peak, in order to exclude the counts contributed by the unknown component. As shown before there was no effect on the number of counts in the (p,γ) peak, by disabling this energy region. Additionally, to this upper energy cut a second energy cut to lower energies was set. This cut removes the events related to the backward scattering of the Rutherford. The energy of the cut was chosen such that there is enough distance to the region of the (p,γ) peak to not cut it.

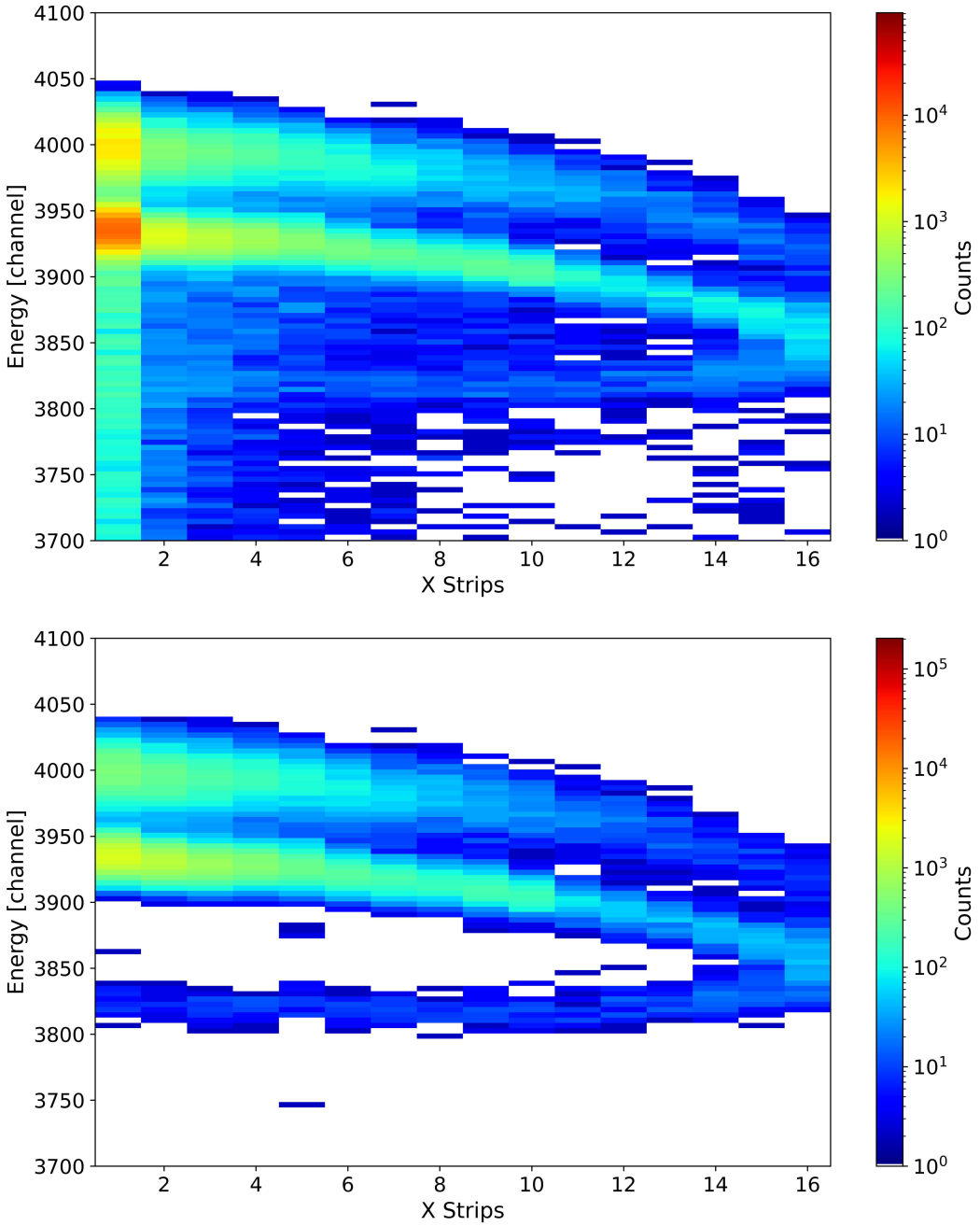

Figure 4.11: Energy over x position for the data of ^{124}Xe without the usage of a scraper. The upper plot includes all the events. The lower plot shows the events to which the condition $E_x = E_y$, within the ΔE, was applied.

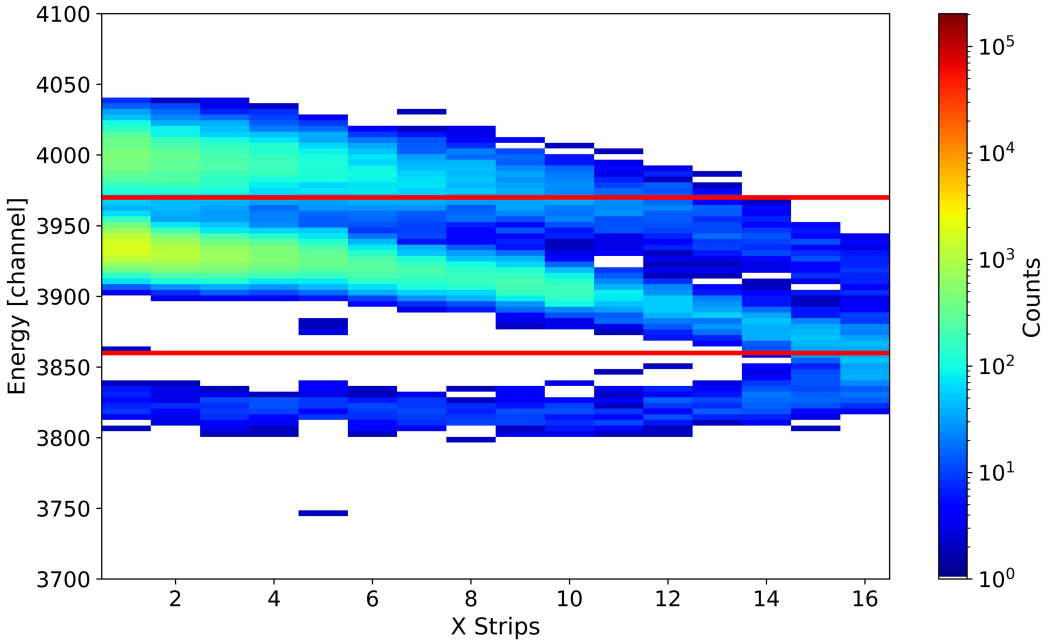

Figure 4.12: Lower and upper energy cut on the analyzed ^{124}Xe data at 7 MeV/u.

Figure 4.12 illustrates the energy cuts that have been set on the ^{124}Xe data at 7 MeV/u. The lower energy cut was set to channel 3860. The upper energy cut to channel 3970. For ^{118}Te at 7 MeV/u the cuts were at channel 3670 for the minimum and 3790 for the maximum. The cuts for ^{118}Te at 6 MeV/u were set to channel number 3120 for the lower cut and channel number 3220 for the upper energy cut. The cuts lead to an improved peak to background relation, visible in Figure 4.13.

After applying these cuts and corrections the data were projected to the x axis.

A one-dimensional fit to these data enables a determination of the background of the peak. The background was described by an exponential function plus a first degree polynomial. That can be subtracted from the integrated number of peaks in the (p,γ) region.

The number of (p,γ) counts still has to be corrected for the efficiency.
In order to determine the efficiency the relation between single strip events and multi-strip events has to be taken into account as described before.

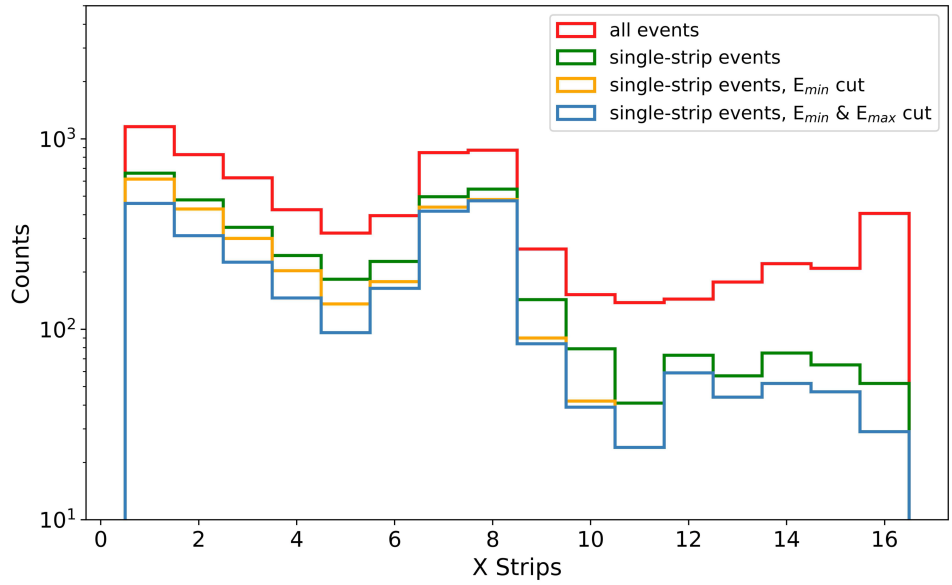

Figure 4.13: Improved peak to background ratio after applying energy cuts.

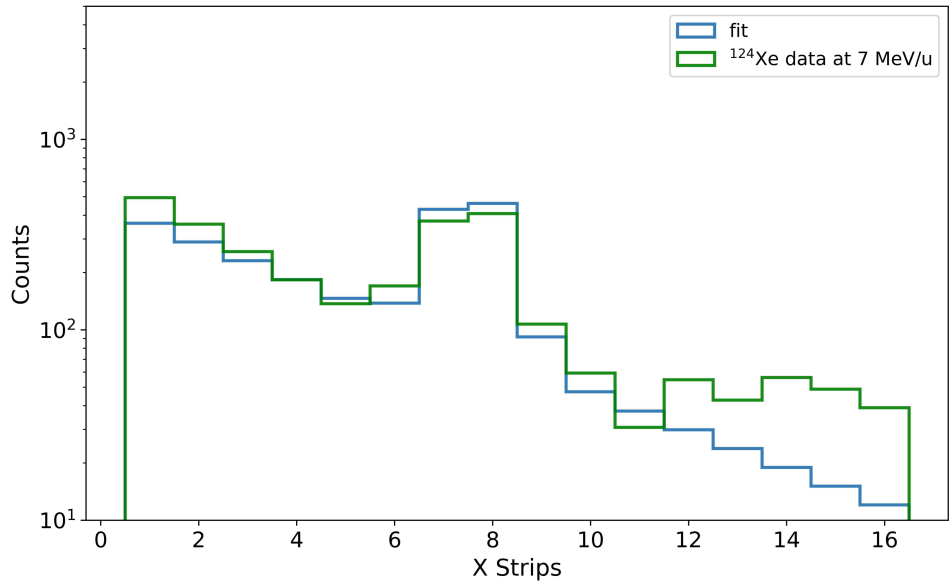

Figure 4.14: Projection of the ^{124}Xe data at 7 MeV/u to the x axis with the applied fit.

As the data for the measurement of ^{124}Xe at 7 MeV/u provide high statistics it has been used to determine the efficiency correction. If the efficiency is averaged over all strips it has a ratio of 77%. Figure 4.15a shows the 16 y strips on the x axis and the correlated efficiency on the y axis. It shows that the 16th x strip has a huge fluctuation and differs from the efficiency of the other strips. The efficiency in this strip is a lot smaller than in the other strips. For the final analysis it can be excluded and only the efficiency in the region of the peak should be considered, as it is not in the region of the (p,γ) peak.

Figure 4.15b shows the efficiency in the x range of the (p,γ) peak. The average efficiency compared to including all strips has increased. Although, it is still visible that the efficiencies between the different strips fluctuate outside of the uncertainties. The statistical uncertainty of each pixel was determined with $\sqrt{N_{\mathrm{Pixel}}}$.

Figure 4.16 gives an overview of the efficiency per pixel. For the final analysis it can not be averaged over all efficiencies. The difference between these pixels could be based on the rather strict selection of ΔE. In addition, the intrinsic calibration has not the same accuracy for every pixel and could thus contribute to these fluctuations. The number of counts should be corrected per pixel.

The results of the two methods shown in table 4.1 for determining the cross section agree within the uncertainties. The statistical uncertainties were determined with $\sqrt{N}$, for the integrated bin content. The systematic uncertainties include the systematic uncertainties of the luminosity measurement. Additionally, the uncertainties of the determination of the (p,γ) position and of the background fit were considered. In the case of ^{124}Xe, the results also agree within the uncertainties with the independent analysis of Laszlo Varga [37].

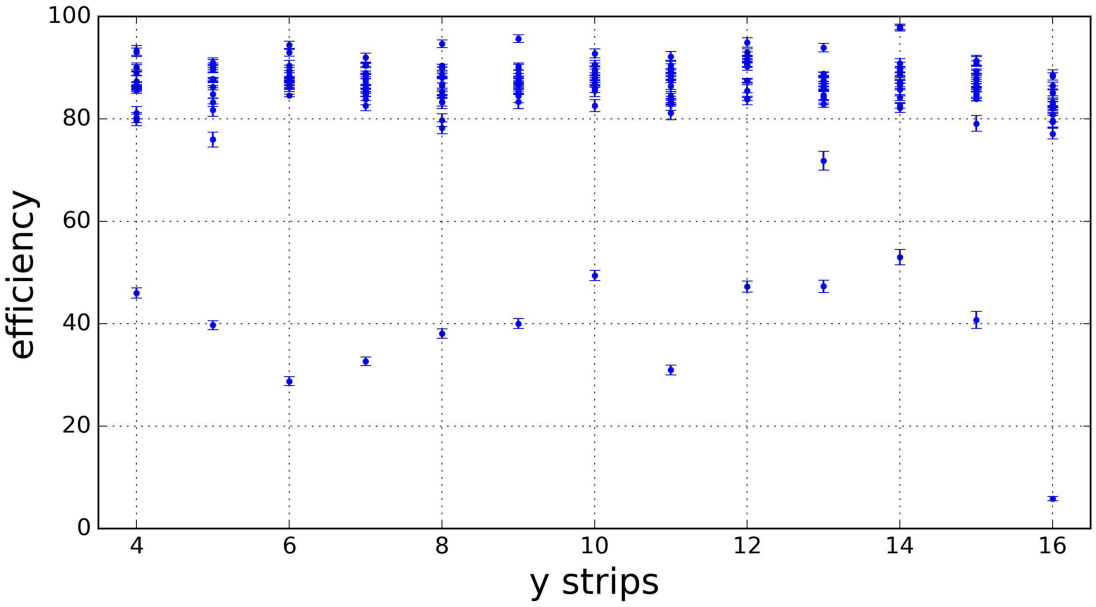

(a) Efficiency of the relation between single strip events and multi-strip events for all y strips.

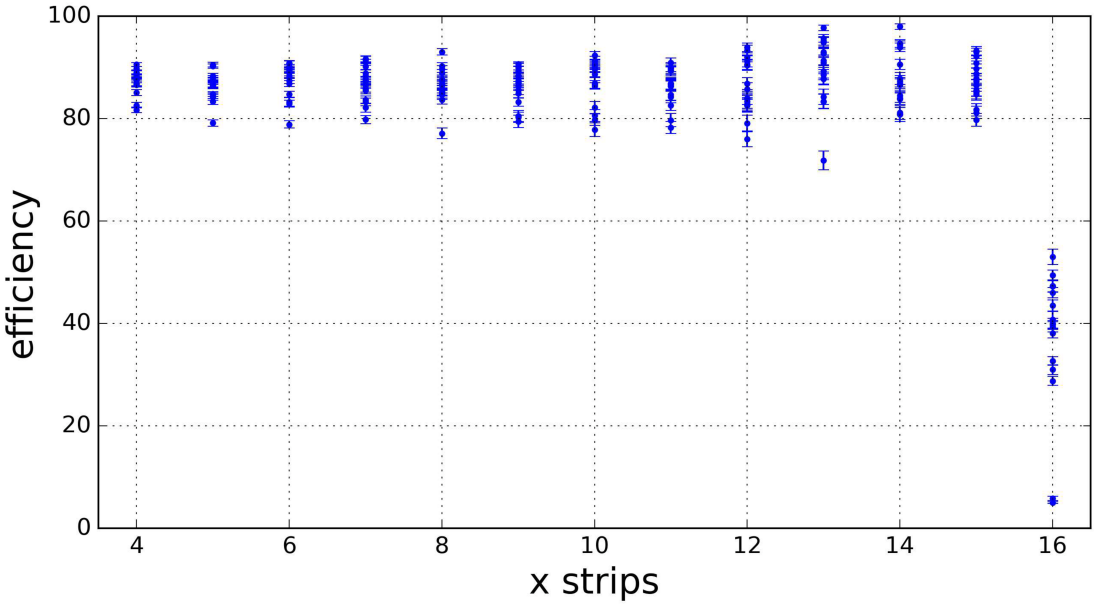

(b) Efficiency of the relation between single strip events and multi-strip events over the x strips in the region of the (p,γ) peak.

Figure 4.15: Efficiency of the relation between single strip events and multi-strip events.

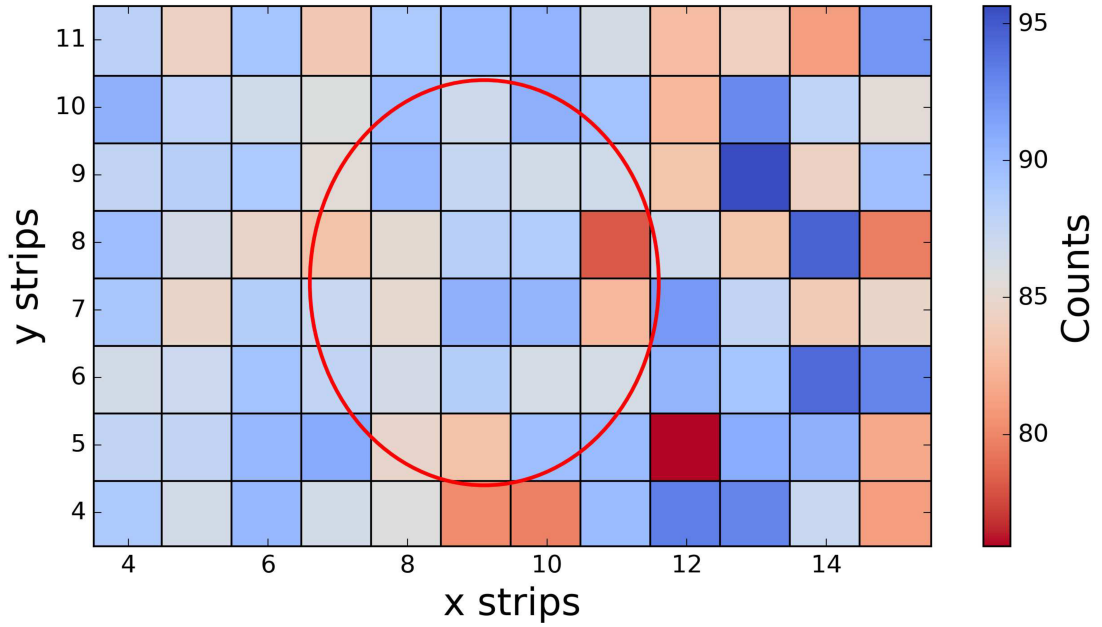

Figure 4.16: Efficiency of each pixel in the (p,γ) region. In red the expected region for the (p,γ) peak, determined with the MOCADI simulations, is marked.

4.4 Discussion

Figure 4.17a shows the final cross section determined within this work for ^{124}Xe at 7 MeV/u. For the final cross section the determination via the single strip events has been chosen. The results of this approach agree within the uncertainties with the analysis using all events. For the final cross section the result from the analysis using single strip events was chosen, as the first approach was purely phenomenological. The cross section of ^{124}Xe(p,γ) at 7 MeV was calulated within the framework of the PhD thesis of Laszlo Varga with a different approach [37]. The result of this approach also matches within the uncertainties of the results obtained in this analysis. This was used as an additional cross-check for this analysis. Thus, the same analysis method has been applied to the ^{118}Te data.

In addition to the experimental data Figure 4.17a shows theoretical determined cross sections. In black cross sections determined with NON-SMOKER are shown [51, 52]. In gray theoretical determined cross sections with TALYS [53] are shown. The NON-SMOKER database and TALYS provide theoretical reaction cross section based on Hauser-Feshbach calculations. The calculations can still differ as they include different data and nuclear models.

The experimental data agree with the theoretical predictions for smaller energies. Around 7 MeV the cross sections determined with NON-SMOKER seem to describe the experimental data better, although the data at 8 MeV can not be described by any of these. In the following chapter the TALYS code has been used to find a better theoretical prediction for the cross sections, that match the data.

Reaction	E [MeV]	σ_{fit} [mbarn]	σ_{eff} [mbarn]
$^{118}\text{Te}^{52+}(p,\gamma)$	6.044	$50\pm\ 9_{\text{stat}}\ \pm\ 6_{\text{sys}}$	$44\ \pm\ 9_{\text{stat}}\ \pm\ 5_{\text{sys}}$
	7.05	$79\pm\ 7_{\text{stat}}\ \pm\ 5_{\text{sys}}$	$71\ \pm\ 5_{\text{stat}}\ \pm\ 4_{\text{sys}}$
$^{124}\text{Xe}^{54+}(p,\gamma)$	7.05	$71\pm\ 7_{\text{stat}}\ \pm\ 5_{\text{sys}}$	$74\pm\ 7_{\text{stat}}\ \pm\ 2_{\text{sys}}$

Table 4.1: Final cross sections determined with two different methods. The cross section σ_{fit} has been determined by using the 2D Gaussian fit. For σ_{eff} every pixel has been corrected by its efficiency.

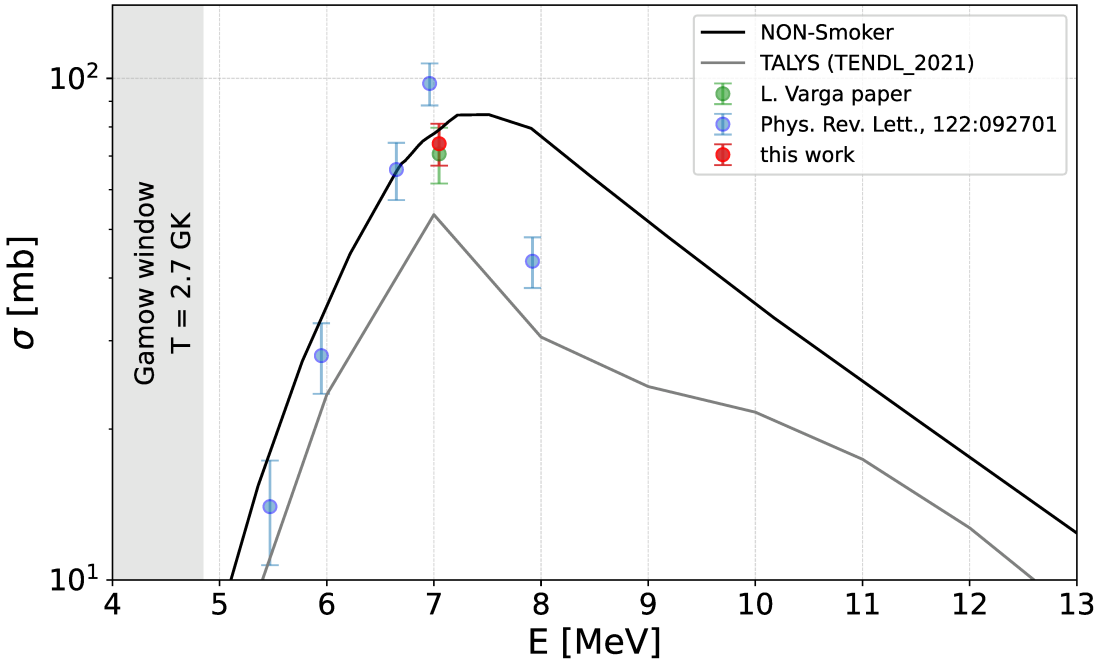

(a) Final cross section of ^{124}Xe(p,γ) at 7 MeV. The cross section is compared to the theoretical predictions and other measurements in this energy range.

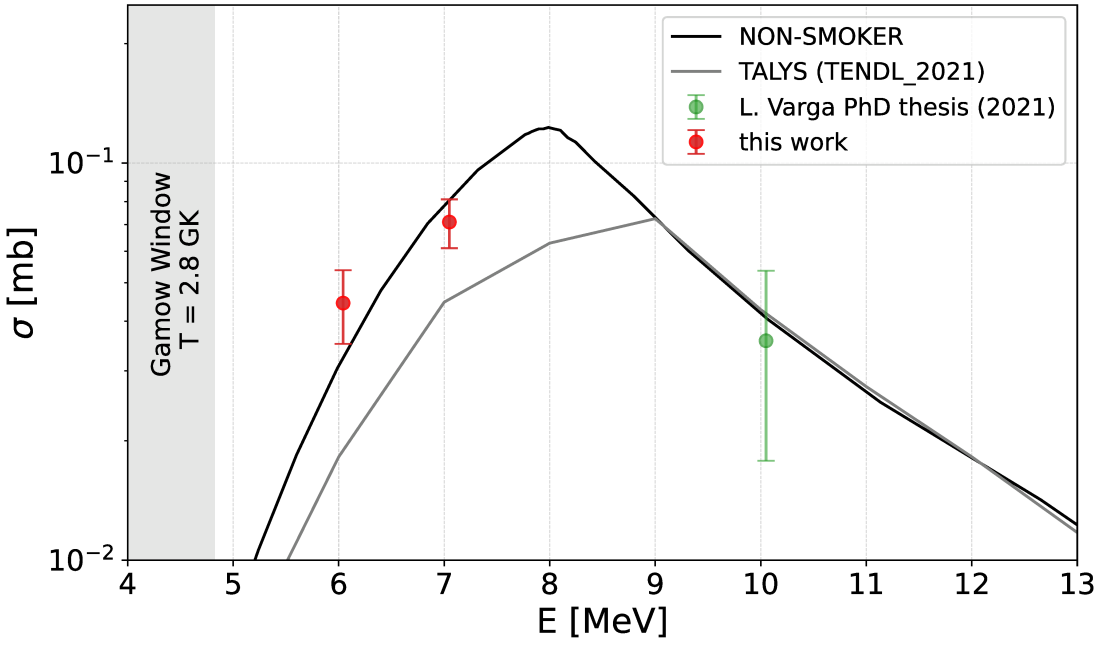

(b) Final cross section of ^{118}Te(p,γ) at 6 and 7 MeV. The cross section is compared to the theoretical predictions and one other measurement in this energy range.

Figure 4.17: Final cross sections for ^{124}Xe(p,γ) at 7 MeV and ^{118}Te(p,γ) at 6 and 7 MeV.

Figure 4.17b shows the final results for the cross section of ^{118}Te(p,γ) at 6 and 7 MeV/u. They have been determined by the same approach as the cross section for ^{124}Xe(p,γ). The data are shown in comparisson to the theoretical predictions by NON-SMOKER and TALYS. In this case NON-SMOKER gives predictions that agree within the uncertainties with the determined cross sections. Thus, it is not neccesary to use the TALYS code to find a better model.

The proton capture reaction on a radioactive isotope has thus been successfully measured. As motivated at the beginning of this work theoretical calculations and experimental data are closely linked in order to make the most accurate predictions possible. In the following chapter a short overview will be given of the implementation of the cross sections in post-processing nucleosynthesis codes.

5 Post-processing nucleosynthesis

One of the motivations of this measurement is the expected influence of an experimentally determined reaction rate on nucleosynthesis networks. Within the NuGrid (Nucleosynthesis Grid) research platform [3] post-processing nucleosynthesis (PPN) studies have been performed in this work. The PPN simulations for the p-process were performed for a core collapse supernova (CCSN) with an initial mass of 20 $M_\odot$ at solar metallicity [54]. The evolution of the isotopic abundances in different shells around the center of the supernova progenitor have been tracked. Once using the reaction rates currently implemented in the simulations and once using the newly determined reaction rates.

5.1 NuGrid

This part of the work was carried out within the NuGrid collaboration, using NuGrid post-processing codes. NuGrid offers a software framework for simulating nucleosynthesis in various astrophysical environments. It derives temperature and density profiles, referred to as "trajectories" from simulations of stellar evolution. The post-processing code, processes these trajectories and calculates stellar abundances, for example the budget of nuclear species produced in a certain stellar environment. Furthermore, the simulations use data sets from the JINA Reaclib Database [55].

Figure 5.1 shows the initial mass fractions for the PPN simulations for the used CCSN model with an initial mass of 20 $M_\odot$ at solar metallicity, relative to solar mass fraction. The initial mass fraction deviates strongly for some isotopes. The PPN simulation stores temperature, mass fractions and density profile for every set time step, in so-called 'trajectories'. The NuGrid collaboration provides a set of python tools (NuGridPy) to analyze the data. Additionally, exemplary codes were provided which were used as a basis for the visualizations in this work [56, 3].

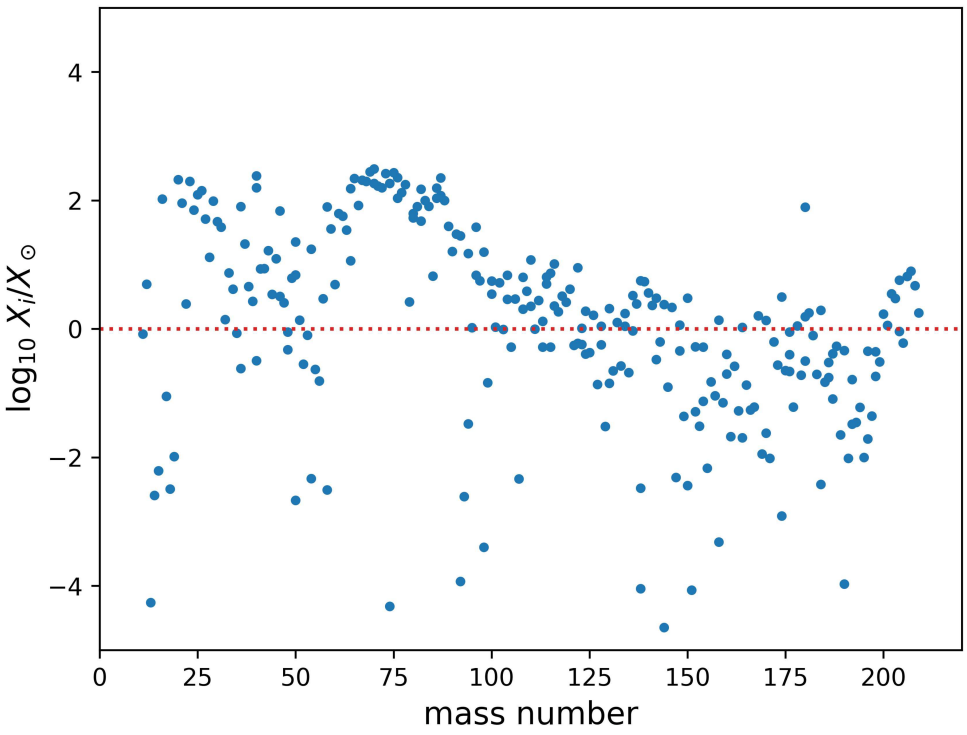

Figure 5.1: Initial abundances for the PPN simulations, relative to the solar abundances. The initial solar composition is given by [5].

The trajectories have been chosen, based on the mass fraction of the isotope of interest. The mass coordinate where the mass fraction of the isotope is at its maximum determines where the trajectory is extracted. The mass fraction of a given isotope i is the ratio of the mass of all nuclei of the isotope and the total mass of all isotopes.

$$X_i = \frac{m_i}{M_{tot}} \tag{5.1}$$

- X_i = mass fraction of the isotope i
- m_i = mass of all nuclei of the isotope i
- M_{tot} = total mass of all isotopes

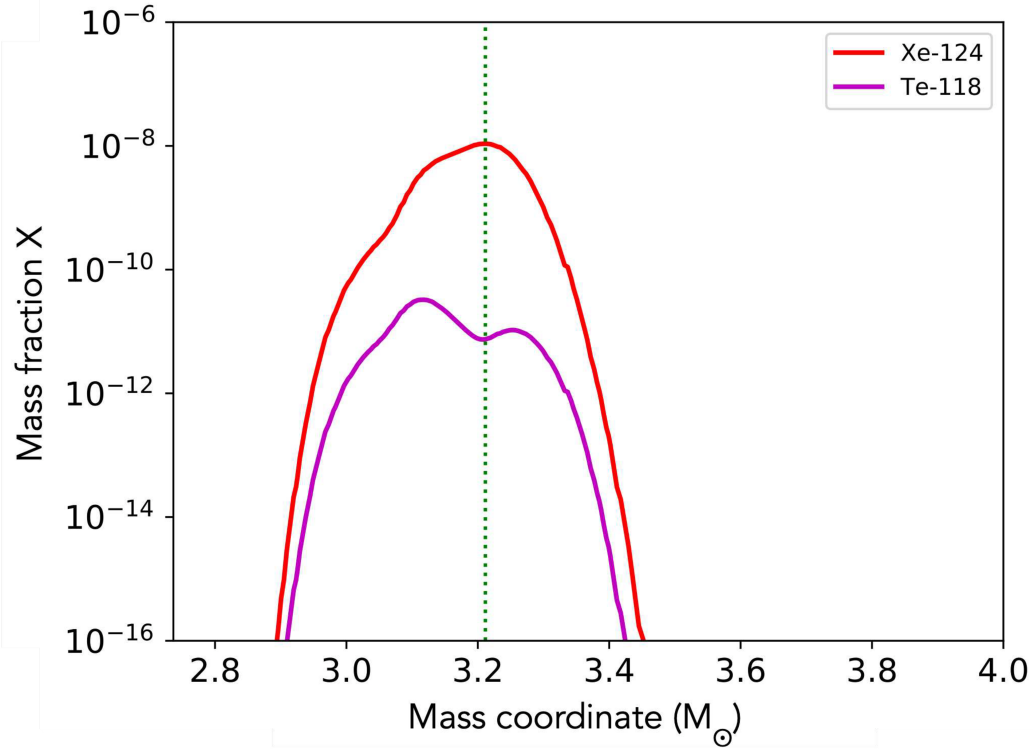

Figure 5.2: Final mass fractions of ^{118}Te and ^{124}Xe of the PPN simulations for the CCSN model, with M_{ini} = 20 $M_\odot$ and Z = 0.02, over the mass coordinate. The implemented reaction rates were used. With the green dashed line the maximum of the mass fraction of ^{124}Xe is labeled.

The summed mass fraction of all isotopes is normalized to 1.

Figure 5.2 shows the structure of the final mass fractions of ^{118}Te and ^{124}Xe of the PPN simulation over the mass coordinate. The other isotopes included in the simulations are not displayed for a better visibility of the isotopes of interest.

In Figure 5.2 this is exemplary shown for ^{124}Xe. The green dashed line is located at the maximum mass fraction of ^{124}Xe. The corresponding mass coordinate is 3.212 $M_\odot$. This is the mass coordinate in the model where the most ^{124}Xe is produced. Within the extracted trajectory at this position an analysis of the temporal evolution of ^{124}Xe and the produced ^{125}Cs was performed. The trajectory will be called *xenon trajectory*. For tellurium two trajectories have been chosen,

as the mass fraction shows two maxima. The trajectories will be called *tellurium trajectory one* and *two*.

5.1.1 Temperature and density evolution

Figure 5.3 shows the temperature and density profile for the *xenon trajectory*. The temperature and density profile describe the astrophysical environment for the chosen mass coordinate as a function of time. Both increase fast to their maximum values. The peak temperature for the *xenon trajectory* is at 2.7 GK.

At this temperature it is most likely that the most ^{124}Xe is produced, since the reaction rates are at their maximum values. This temperature has thus been used for the determination of the Gamow window as shown in the results in section 4.4. In Table 5.1 the values are given also for the tellurium trajectories.

The trajectories are only representative for the mass coordinate at which the most ^{124}Xe or ^{118}Te gets produced. To understand better the processes in this mass region two further trajectories were extracted. In between these mass coordinates more than 90% of xenon gets produced. These trajectories are at 2.9 and 3.5 $M_\odot$. The change of mass fraction over time, in relation to the temperature over time was analyzed.

Figure 5.4 shows the temporal evolution of the mass fraction of ^{124}Xe for the three different mass coordinates. In dotted lines the corresponding temperatures are shown. In red the results of the trajectory at the mass coordinate of 2.9 $M_\odot$ are displayed. The production takes place at a higher temperature compared to the other two trajectories. A high and fast increasing production rate is visible. It reaches fast the maximum, but it also get destroyed fast. This correlates with the high temperatures at this mass fraction, which enhances the destruction mecha-

Trajectory	Mass [$M_\odot$]	max. temperature [GK]	max. density [10^5 g cm^{-3}]
xenon	3.212	2.7	1.8
tellurium 1	3.118	2.8	2.1
tellurium 2	3.252	2.7	1.7

Table 5.1: Parameters of the *xenon* and *tellurium trajectory*: mass coordinate, maximum temperature and the maximum density.

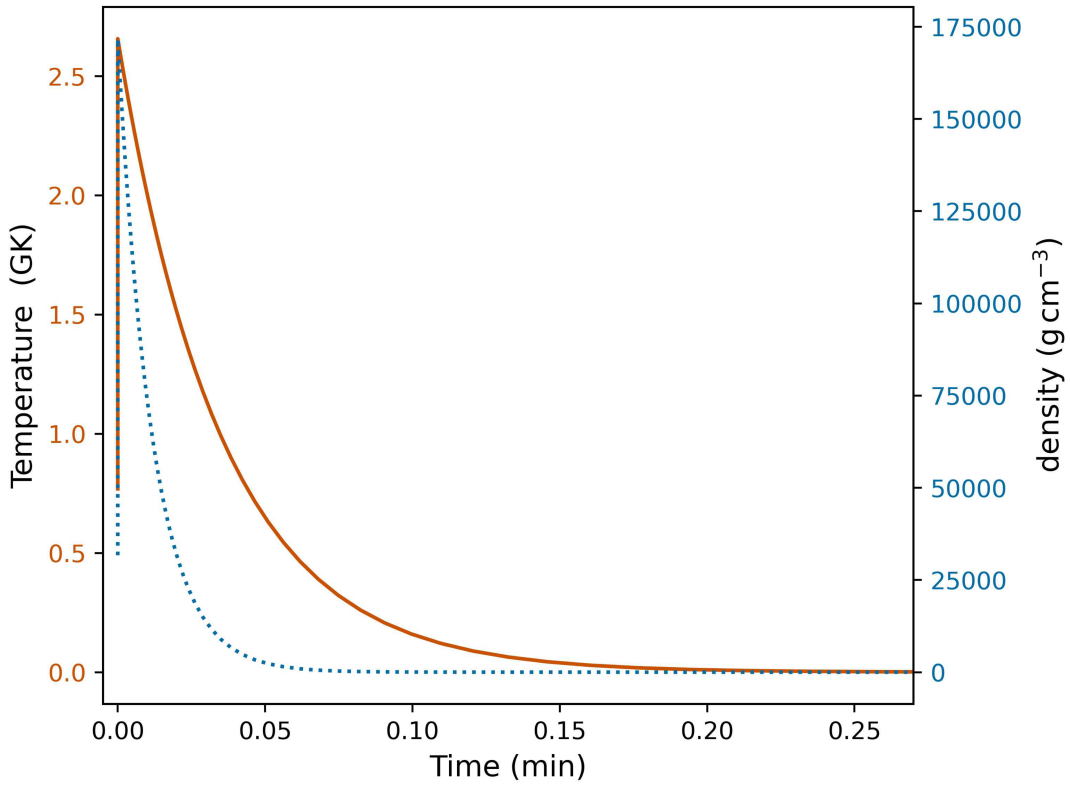

Figure 5.3: Temperature and density over time for the *xenon trajectory*.

nism. The main destruction process of ^{124}Xe is (γ,n) [57, 58]. In yellow the results of the trajectory at the mass coordinate of 3.5 $M_\odot$ are shown. The production takes place at lower temperatures and less ^{124}Xe is produced.

The highest final mass fraction, of ^{124}Xe is reached for the trajectory at the mass coordinate 2.212 $M_\odot$, which is the mass coordinate of the *xenon trajectory*. The destruction mechanisms do not take over, leading to this high production. This confirms the choice of the *xenon trajectory*, based on the highest production. For the following analysis this trajectory was used, and the possible construction and destruction mechanisms were analyzed.

5.1.2 Nucleosynthesis fluxes in the xenon and tellurium region

Figure 5.5 shows the mass flow in the region around the measured ^{118}Te and ^{124}Xe isotopes, that are emphasized with a red background. The order of magnitude

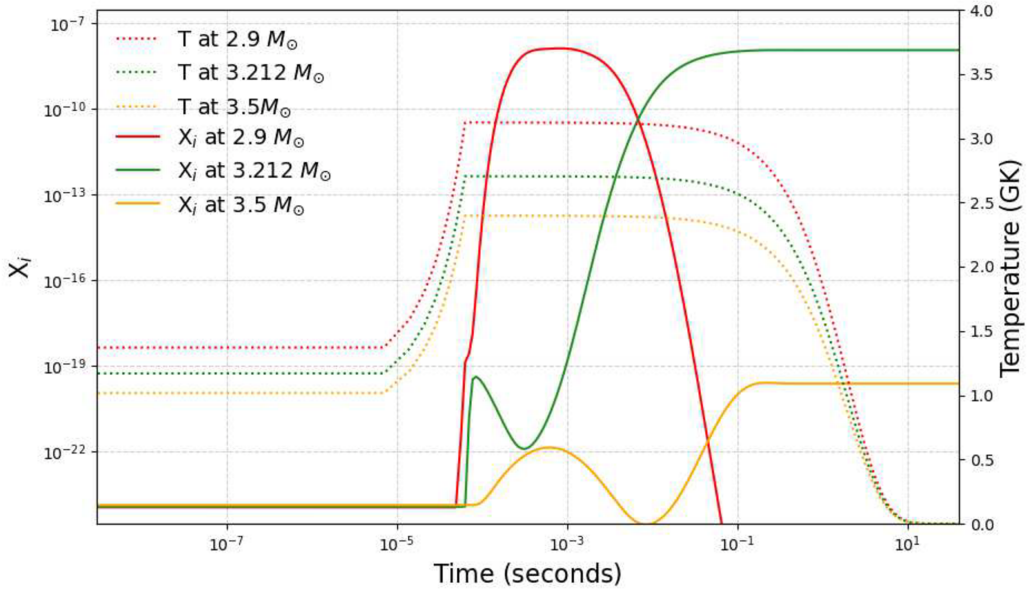

Figure 5.4: The evolution of the ^{124}Xe mass fraction (solid lines) is given at three different mass coordinates and the corresponding temperature (dotted lines). The green line corresponds to the *xenon trajectory*.

of the fluxes is indicated by the color bar and the thickness of the arrows, that scale linear with $\log_{10}$(flux). The competing mechanisms considered here are (n,γ), (γ,n), (γ,α), (p,γ) and (γ,p).

The main destruction mechanism for ^{119}I and ^{125}Cs are (γ,p) reactions. These are the time inverse reactions of the measured ^{118}Te(p,γ) and ^{124}Xe(p,γ). The effect of a reaction rate change on the mass fraction of the products of the time reversed reaction will be tested. In the case of xenon, the mass fraction of ^{125}Cs over time will be analyzed. For this, the reaction rates for every reaction included in this network can be changed individually.

As in this experiment no reaction rates but cross sections at specific energies have been determined, as a first step the reaction rates, have to be determined.

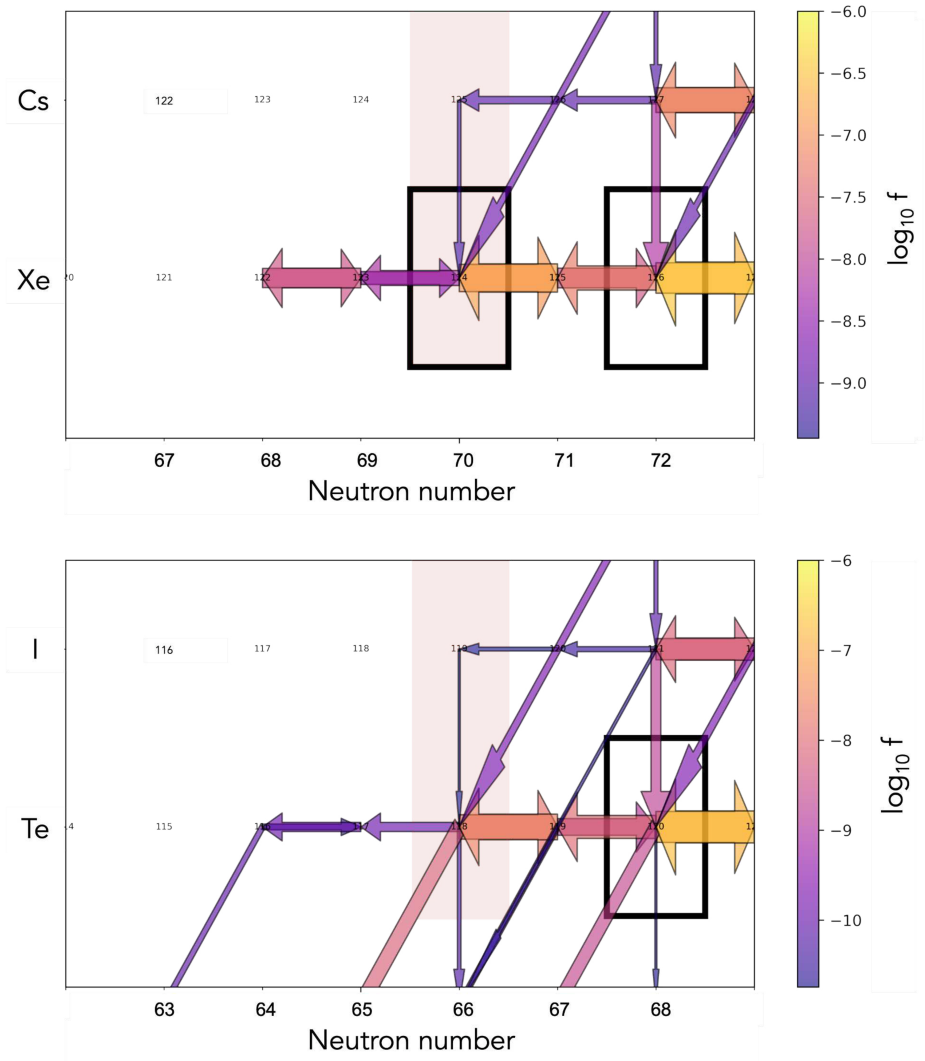

Figure 5.5: Integrated flux during the *xenon trajectory* and *tellurium 1 trajectory*. It is shown that for ^{125}Cs and ^{119}I the main destruction mechanism are (γ, p) reactions. The time inverse reaction of the ones measured during this experiment. The arrow thickness scales linearly with $\log_{10}$f.

5.1.3 Determination of the astrophysical reaction rates

For the PPN simulations reaction rates from the JINA Reaclib Database [55] are used. As discussed in the previous chapter the cross sections determined experimentally do not agree perfectly with the predictions from NON-SMOKER, which is the input for the JINA Reaclib Database for these reactions.

In order to determine the reaction rates cross sections over a wider energy range are necessary (equation 1.3). This can be estimated with TALYS [53]. TALYS applies different nuclear models in order to calculate cross sections over very large energy regimes. The implemented models can be changed to find the best prediction. In this work the TALYS-1.96/2.0 version was used.

The obtained ^{118}Te(p,γ) cross sections agree well with the theoretical predictions provided by NON-Smoker. Whereas the cross sections determined for ^{124}Xe(p,γ) differ from the predictions of NON-SMOKER, but also from TALYS. Especially the cross section at 8 MeV can not be described by any of the models.

With the help of TALYS a different model was found for the ^{124}Xe(p,γ) cross sections. The change compared to the standard input of TALYS was the use of a different model for the level density. In the standard input the phenomenological model of constant temperature and Fermi gas model is implemented [59]. The level density model used for the newly determined cross sections is based on Hartree-Fock calculations [60]. The decision for this model was based on the agreement with the experimental data. The improved model will be called *modelXe*.

The model has also been applied for the cross sections of ^{124}Xe(p,γ). Figure 5.6 shows the model in orange in comparison to the data. In Figure 5.7 it is shown in comparison to the experimental ^{118}Te(p,γ) data. It is visible that *modelXe* overestimates the ^{118}Te(p,γ) cross sections.

Thus, for the ^{118}Te data the model was further adjusted and will be called *modelTe*. In addition to *modelXe* the γ-strength function has been changed. The γ-strength function describes the interaction of photons and nuclei. The temperature-dependent RMF model by Daoutidis and Goriely was used [61]. The *modelTe* is shown in comparison to the ^{118}Te(p,γ) data in green in Figure 5.7. It shows an improvement of the description compared to *modelXe*. The approach was also compared to the ^{124}Xe(p,γ) data, visible in Figure 5.6, resulting in an underestimation of the cross sections.

For the determination of the astrophysical reaction rates *modelXe* was chosen for the ^{124}Xe(p,γ) data and *modelTe* for the ^{118}Te(p,γ). The goal was to test a possible influence of the experimental data. Considering the interest of describing

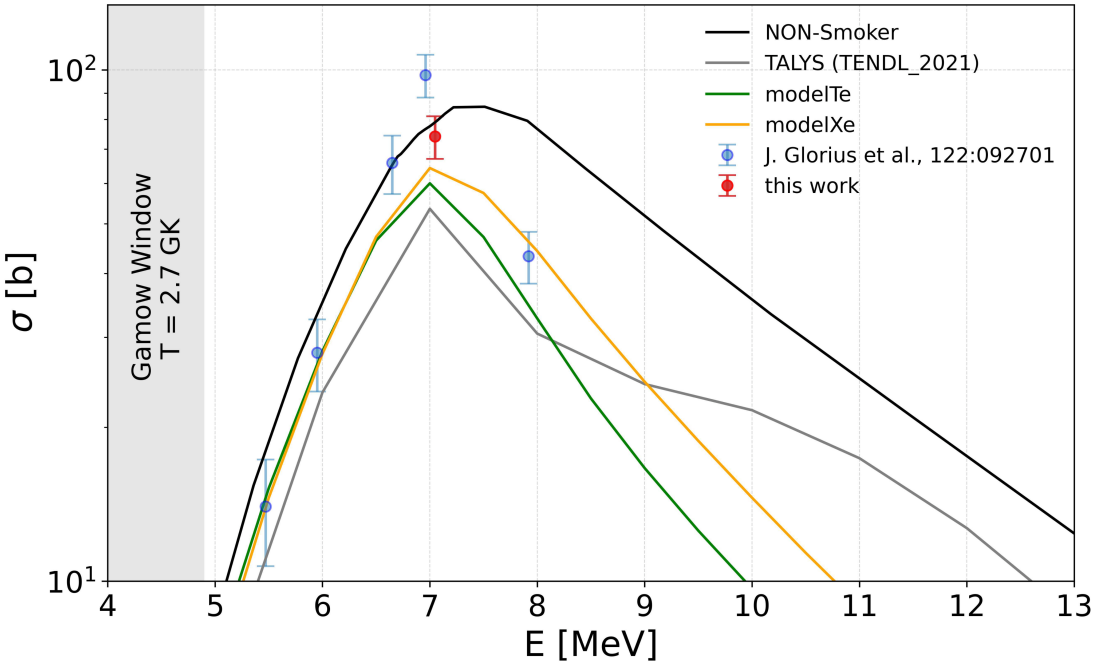

Figure 5.6: Experimental cross sections for the ^{124}Xe(p,γ) data, compared to theoretical predictions. In gray and black are the predictions from TALYS and NON-SMOKER, respectively based on the standard input parameter. In green the predictions of *modelTe* are shown and in orange of *modelXe*.

the nuclear structure accurately and with them determining the cross sections, it would be desirable to find one model that describes all nuclei in this region.

With the new reaction rates a ratio can be determined that describes how much the reaction rates implemented in the Nugrid post-processing codes differs from the ones determined with the TALYS calulations, that describe the experimental data. Table 5.2 shows the ratios for the different models. For ^{124}Xe(p,γ) the astrophysical reaction rates have been determined with the two different models determined before. The result at a temperature of 2.7 GK has been divided by the astrophysical reaction rate from NON-SMOKER at the same temperature. The results are displayed in Table 5.2. The same was done for the reaction rates of ^{118}Te(p,γ) at 2.8 GK.

The new determined reaction rates can be included into the post processing

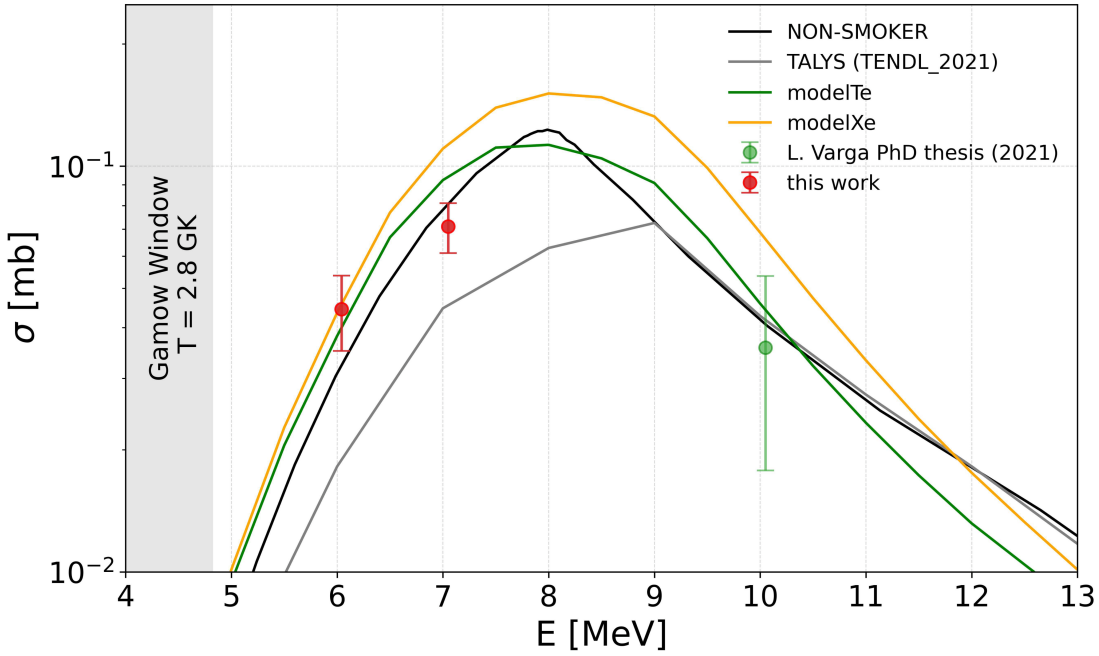

Figure 5.7: Experimental cross sections for the ^{118}Te(p,γ) data, compared to theoretical predictions. In gray and black are the predictions from TALYS and NON-SMOKER, respectively based on the standard input parameter. In orange the predictions of *model Xe* are shown and in green of *model Te*.

nucleosynthesis codes. The implementation was done by scaling the implemented reaction rates by the ratios determined in Table 5.2.

Reaction	Temperature [GK]	modelXe/NON-SMOKER	modelTe/NON-SMOKER
^{124}Xe(p,γ)	2.7	1.4	1.2
^{118}Te(p,γ)	2.8	1.7	1.64

Table 5.2: Ratios of the astrophysical reaction rates determined with the TALYS models and NON-SMOKER at the maximum temperature for the production of ^{124}Xe and ^{118}Te.

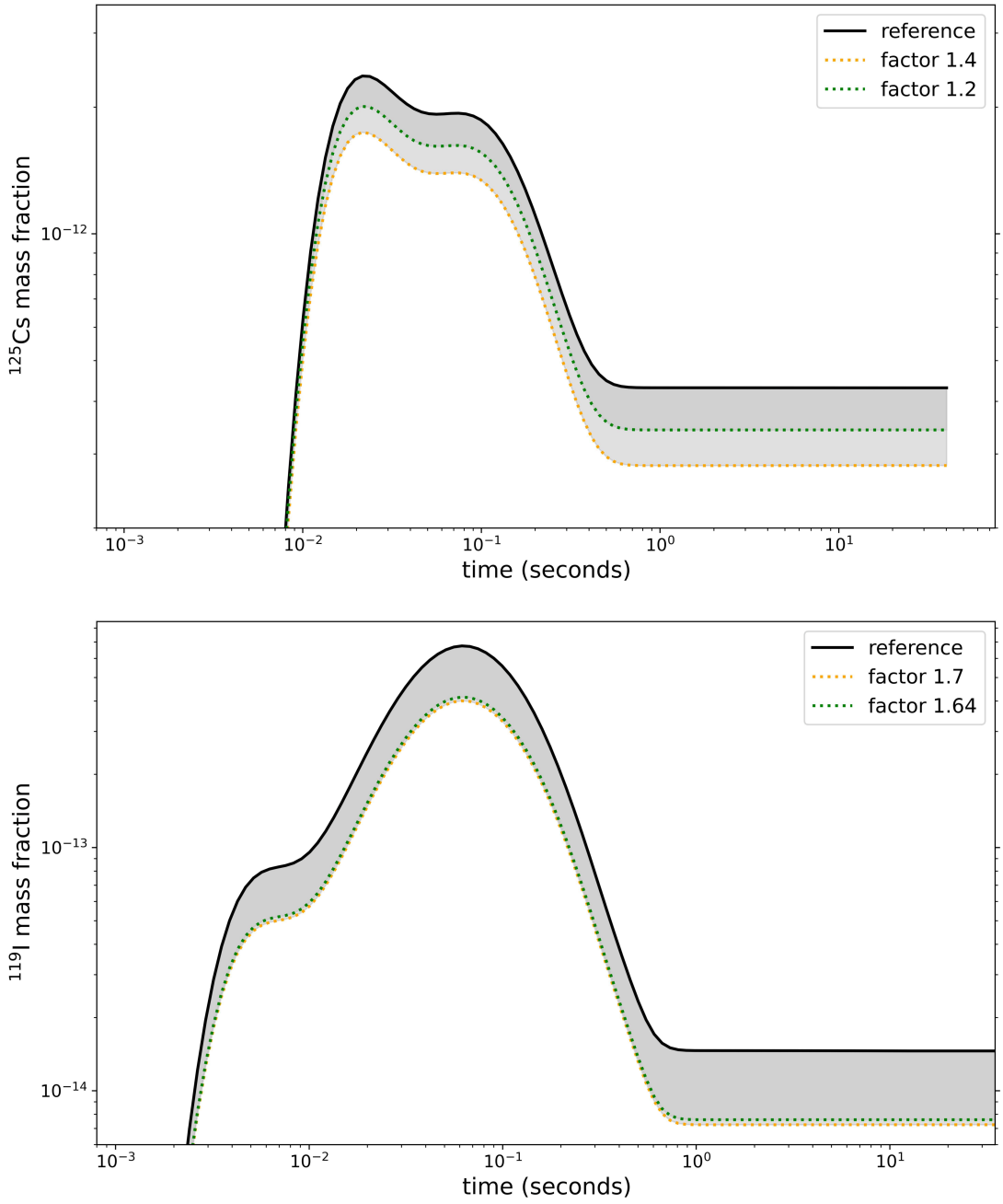

Figure 5.8: Temporal evolution of the mass fraction of ^{125}Cs and ^{119}I. In orange the evolution of the mass fraction is shown for the astrophysical reaction rates from *modelXe* and in green for *modelTe*.

The results of this will be shown by analyzing the temporal evolution of the mass fraction, once with the newly determined reaction rates and once with the implemented rates.

Figure 5.8 shows the temporal evolution of the mass fraction of ^{125}Cs and of ^{119}I. The black line, labeled as reference shows the evolution, when the astrophysical reaction rates implemented in the simulations are used. In green the evolution of the mass fraction is shown, with the reaction rates obtained from the model that describes the cross sections of ^{124}Xe the best. In orange the model describing the ^{118}Te(p,γ) data were used.

The change of the reaction rates leads in both cases to a lower mass fraction of the reaction product. Figure 5.9 shows the relation of the determined final mass fractions compared to the implemented rates. The final mass fractions have been determined with *modelXe* and *modelTe*. The relation of the mass fractions resulting from *modelXe* and *modelTe* to the mass fractions resulting from the implemented rates are plotted over the mass number A. The used colors correspond to the *modelXe* in green and *modelTe* in orange. For both images only the region around the mass of the reaction products as shown, as for the other isotopes no change was visible. This means that the ratio was 1.

The influence on the mass fraction of ^{125}Cs and ^{119}I show the highest effect of the changed reaction rates, as visible in Figure 5.8. Comparing this to the shown ratio in Figure 5.9 the influence seems very small. This can be explained by the low abundance of the p-nuclei. In Figure 5.9 isobars are shown, thus it sums all nuclei of the same mass number A, leading to a small influence of the change of reaction rates. The new determined reaction rates show only a considerable effect in a very small mass region on a few isotopes. For the remaining reaction network the impact is negligible.

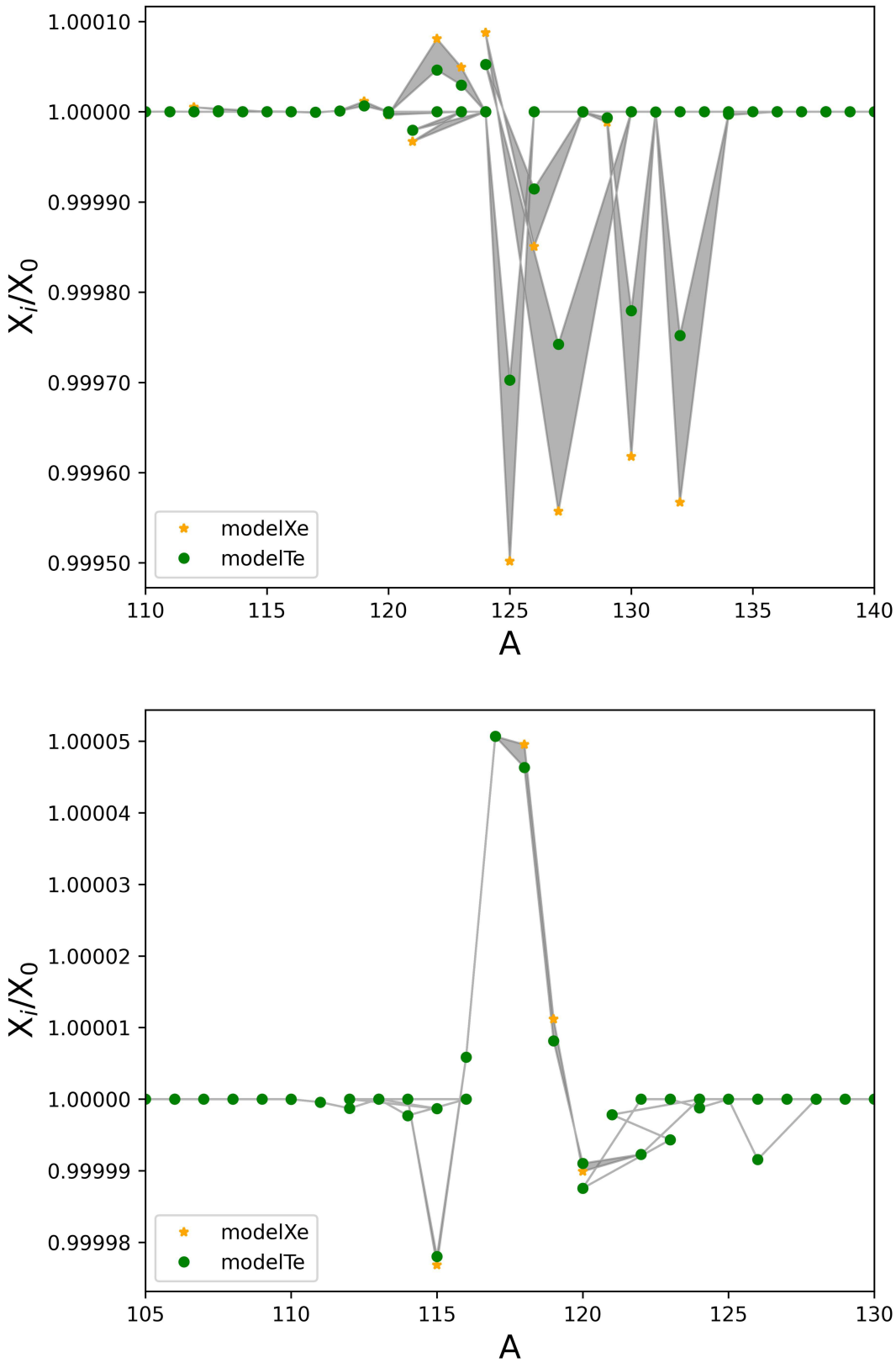

Figure 5.9: Relation of the final mass fraction after applying the new reaction rates X_i to the final mass fraction with the implemented reaction rates X_0.

6 Summary and future perspectives

Within this work astrophysically important nuclear proton-capture cross sections have been measured. The cross sections of the proton capture reaction of the radioactive isotope ^{118}Te at energies of 6 and 7 MeV/u and of the stable isotope ^{124}Xe at 7 MeV/u have successfully been measured. The (p,γ) reaction channel was analyzed with the spectra of the Double Sided Silicon Strip Detector.

The measurements were performed in inverse kinematics at the Experimental Storage Ring at GSI. The combination with the fragment separator enables a direct measurement of a proton capture reaction on stored radioactive ions, for the first time in astrophysical interesting energies. Additionally, a new setup has been included in the experiment that reduced the background and thus increased the sinsitivity of the technique [37].

The analysis of the experimental data was challenging due to unexpected background contributions. Thus, new approaches had to be developed to describe the shape of the background. In the first approach all events have been considered for the analysis. The background was described phenomenological with a two-dimensional Gaussian fit. In the second approach the data were reduced to single strip events. Single strip events are events in which both sides of the DSSSD detect the same energy. This condition enabled multiple cuts on the data, which lead to an improvement of the peak to background ratio.

The results have been compared to theoretical predictions. Furthermore, they have been implemented into NuGrid post-processing nucleosynthesis (PPN) studies [3]. The PPN simulations were performed for a core collapse supernova with an initial mass of 20 $M_\odot$ at solar metallicity [54].

Since this experiment successfully demonstrated the possibility of determining a proton capture cross section using stored radioactive isotopes in the low energy range, new experiments can be planned for the future, based on these developments. Other radioactive isotopes can be investigated, that have a high impact in

the nucleosynthesis networks.

There are three obvious directions of future experiments.

First more complicated cases could be approached. A proposal already submitted for this purpose aims at measuring the proton capture cross section of ^{91}Nb in the ESR [62]. The motivation behind measuring this is as for this experiment the origin of the p-nuclei. In this specific case the origin of ^{92}Mo. The models that simulate various scenarios of explosive nucleosynthesis fail to produce it in solar amounts. Measuring directly the proton-capture reaction cross-section on the ground state ($T_{1/2}$ = 680 a) and the isomeric state ($T_{1/2}$ = 61 d) of ^{91}Nb in order to constrain the production of ^{92}Mo in the γ-process.

Second, alpha induced reactions could be measured. For this approach a helium target could be used instead of a hydrogen target. With this, it might be possible to measure alpha gamma and also (α,n) reactions.

A third direction could be to perform experiments at lower energies. The described experiments have been performed at the upper end of the Gamow window. Measuring inside of the Gamow window is one of the future goals, for measuring proton capture reactions. The CRYRING@ESR storage ring, the low-energy extension of the ESR machine provides the possibility to perform proton capture measurements at lower energies [63, 64].

7 Zusammenfassung

Im Rahmen dieser Arbeit wurden zum weltweit ersten Mal Wirkungsquerschnitte für Protoneneinfänge an gespeicherten radioaktiven Kernen in inverser Kinematik im astrophysikalisch relevanten Bereich gemessen. Dabei wurden die Wirkungsquerschnitte für ^{118}Te(p,γ) bei 6 MeV/u und 7 MeV/u bestimmt. Darüber hinaus wurde der Wirkungsquerschnitt für das stabile Isotop ^{124}Xe(p,γ) bei 7 MeV/u gemessen. Das Experiment wurde an der GSI, Helmholtz-Zentrum für Schwerionenforschung durchgeführt. Durch die Kombination zweier außergewöhnlicher Anlagen, dem Fragmentseparator (FRS) und dem Experimentier-Speicherring (ESR), wurde dieses Experiment möglich. Diese Messungen folgten einem Proof-of Principle Experiment, welches zur Validierung der Methode an dem stabilen Isotop ^{124}Xe diente [65]. Das vorangegangene Experiment wurde mit einem neuen experimentellen Aufbau weiterentwickelt. Der neue Aufbau führte zu einer deutlichen Verringerung des Untergrunds, welcher durch Streuung verursacht wird [37].

Die Motivation zur Durchführung dieses Experimentes liegt darin, einen Beitrag zum Verständnis der Entstehung der Elemente zu leisten. Der Fokus liegt in diesem Fall auf der Entstehung der sogenannten p-Kerne. Es gibt ungefähr 35 protonenreiche Kerne, deren Produktion nicht über Prozesse erklärt werden kann, die die Mehrheit der anderen schweren Kerne produzieren. Sie können nicht durch Neutroneneinfänge erklärt werden [6]. Für ihre Entstehung stehen verschiedene Produktionsmechanismen unter Diskussion. Man geht davon aus, dass sie hauptsächlich über Protoneneinfänge und Photodisentegration in Kombination mit β^+ Zerfällen erzeugt werden. Die dafür notwendigen hohen Temperaturen, deuten daraufhin, dass für die Produktion explosive Bedingungen notwendig sind. Mögliche stellare Umgebungen der Produktion sind daher Kernkollaps Supernovae [8].

Aufgrund der großen Schwierigkeiten, diese Umgebungen experimentell zu reproduzieren, basieren die meisten Vorhersagen auf Simulationen. Diese Simulationen basieren auf Netzwerken, die tausende von Kernen mit mehreren zehntausenden Reaktionen verknüpfen. Diese Reaktionsraten fundieren aufgrund der fehlenden

experimentellen Daten auf theoretische bestimmten Daten und besitzen somit große Unsicherheiten. Die meisten Reaktionen, die Grundlage dieser Vorhersagen sind, sind Reaktionen mit radioaktiven Isotopen. Es ist somit besonders wichtig experimentelle Daten für die relevanten Reaktionen zu erhalten um Vorhersagen mit größerer Sicherheit machen zu können.

Die Reaktion ^{118}Te(p,γ), in diesem Experiment in inverser Kinematik gemessen, ist eine dieser Reaktionen. Es konnte zum aller ersten mal ein experimenteller Wert für diese Reaktion bei austrophysikalisch relevanten Energien bestimmt werden und ein Beitrag zum Verständnis der Entstehung der p-Kerne geleistet werden. Außerdem ist ^{118}Te das Produkt von ^{119}I(γ,p). Eine direkte Messung des Protoneneinfangs Querschnitts an ^{118}Te ermöglicht auch eine Aussage über den zeitinversen Reaktion.

Das Experiment wurde am Experimentellen Speicherring der GSI durchgeführt, da dieser außergwöhnlich präzise Bedingungen für die Untersuchung von Kernreaktionen in inverser Kinematik bietet. Die Messung in inverser Kinematik bietet die Möglichkeit radioaktive Isotope zu untersuchen, die frisch durch Fragmentationsreaktionen erzeugt wurden. Diese Isotope können mit einem sehr dünnen Wasserstoff-Target reagieren. Durch die Speicherung im Ring können, die gespeicherten Isotope immer wieder mit dem Wasserstoff reagieren. Dies ermöglicht sehr hohe Luminositäten. Dadurch ist es möglich auch sehr kleine Wirkungsquerschnitte zu messen. Aufgrund der präzise regulierbaren Energie des Ionenstrahls in Kombination mit dem dünnen Gastarget können präzise energiedifferenzierte Messungen der (p,γ) Wirkungsquerschnitte durchgeführt werden. Energieverluste in der Targetregion können mit Hilfe des Elektronenkühlers ausgeglichen werden.

Im Anschluss an das Wasserstoff-Target befindet sich im experimentellen Aufbau ein Dipolmagnet, Die Reaktionsprodukte, verändern durch den Einfang eines Protons ihre Ladung. Sie werden aufgrund ihrer veränderten Ladung, gegenüber den unreagierten Teilchen im anschließenden Dipolmagnet auf eine andere Bahn abgelenkt. Durch eine Positionierung eines Detektors, an der Stelle, an der die Reaktionsprodukte erwartet werden, können diese detektiert werden. Der in diesem Aufbau verwendete Detektor war ein doppelseitiger Siliziumstreifendetektor (DSSSD). Der DSSSD besitzt 16 horizontale Streifen auf der Vorderseite und 16 vertikale Streifen auf der Rückseite. Durch die Energiedeposition in Vorder- und Rückseite des Detektors, lässt sich die Position der Ereignisse bestimmen.

Zusätzlich zum DSSSD wurden High-Purity Germanium (HPGe) Detektoren verwendet. Die verwendeten HPGe Detektoren waren unter verschiedenen Winkeln

um das Target positioniert. Sie haben die ausgesendete Strahlung der Rekombination der Ionen und Elektronen aus dem Wasserstoff-Target gemessen. Diese Reaktion findet parallel zum Protoneneinfang statt. Die Wahrscheinlichkeit, dass diese Reaktion stattfindet, kann mit theoretischen Berechnungen mit einer Unsicherheit von nur 1% abgeschätzt werden. Sie konnte daher als Luminositätsmonitor verwendet werden [1]. Diese Bestimmung eines Wirkungsquerschnitts, parallel zu einem bekannten Prozess ermöglicht eine alternative Bestimmung des Wirkungsquerschnitts gegenüber des klassischen Ansatz. Bei einem klassischen Ansatz würde man den Wirkungsquerschnitt über die Targetdichte- und den Teilchenstrom bestimmen. Eine Bestimmung über diese Methode würde in diesem Fall zu größeren Unsicherheiten führen, weshalb die Alternative gewählt wurde. Die Unsicherheiten entstehen zum einen aufgrund der Schwierigkeit den Überlapp von Strahl und Wasserstoff-Target zu bestimmen. Zum anderen ist das Wasserstoff-Target nicht während des gesamten Messzeitraumes stabil. Diese Schwankungen müssten genau bestimmt und berücksichtigt werden.

Für ein besseres Verständnis der ablaufenden Prozesse während des Experiments wurden im Rahmen dieser Arbeit Simulationen durchgeführt. Für die Simulationen wurde ein an der GSI entwickelter Monte-Carlo-Code (MOCADI) verwendet [48, 47]. MOCADI kann die Trajektorien von Ionen in elektromagnetischen Feldern und Materie simulieren. Durch eine Erweiterung, die Zweikörperreaktionen reproduzieren kann, wurden die zu erwartenden Reaktionen simuliert. Mit Hilfe der Simulationen konnten Vorhersagen über die erwarteten Ereignisse auf dem Detektor gemacht werden.

Für die Auswertung wurden die Daten des DSSSD, sowie der HPGe-Detektoren verwendet. Es wurden verschiedene Ansätze zur Auswertung der Daten des DSSSD gewählt, um die Fehler der Methoden gering zu halten.

Die Daten zeigten einen Peak bei höheren Energien, als die aufgrund der Reaktionskinematik erwarteten. Außerdem war die Position der Ereignisse, die zu diesem Peak gehörten, versetzt. Der Peak wurde ausführlich analysiert und interpretiert. Im Rahmen dieser Arbeit konnte der Ursprung dieses Peaks dennoch nicht geklärt werden. Für die Bestimmung der Wirkungsquerschnitte konnte aber ein bedeutender Einfluss dieses Peaks ausgeschlossen werden. Er wurde daher für die finale Analyse über einen Energiecut ausgeschlossen.

Auch nach dem Energiecut zeigte der Untergrund eine unerwartete Struktur. Aufgrund des neuen Aufbaus in diesem Experiment war die Struktur der Daten auf dem Detektor grundsätzlich anders als in vorangegangenen Arbeiten. Der neue Aufbau in diesem Experiment beinhaltete einen sogenannten Scraper [37].

Dieser Scraper sollte den Untergrund im Bereich des Peaks reduzieren. Die vorangegangen MOCADI Simulationen zeigten sogar eine vollständige Entfernung des Hintergrunds.

Die experimentellen Daten zeigten eine Verbesserung des Peak zu Untergrundverhältnisses, aber keine vollständige Entfernung. Der Untergrund folgte somit weder der ohne Scraper bekannten, noch der simulierten Form. Mit Hilfe zweier verschiedener Ansätze konnte der Untergrund dennoch zufriedenstellend beschrieben werden. Die Ergebnisse beider Ansätze stimmen im Rahmen ihrer Unsicherheiten überein.

Bei dem ersten Ansatz handelt es sich um einen phänomenologischen Ansatz. Der Untergrund, sowie der peak wurde mit Hilfe eines zwei-dimensionalen Gauß Fits beschrieben. Die Auswertung der Residuen zwischen experimentellen Daten und Fits zeigt eine gute Übereinstimmung. Die Anzahl der Ereignisse konnte daraufhin über eine Integration des Peaks bestimmt werden, von dem der gefittete Untergrund abgezogen wurde.

Für den zweiten Ansatz wurden nicht alle detektierten Ereignisse verwendet. Die ausgewerteten Ereignisse wurden durch eine Bedingung auf die registrierte Energie eingeschränkt. Dabei musste die im vorderen und hinteren Streifen registrierte Energie, im Rahmen der Energieauflösung, übereinstimmen. Es werden somit nur Ereignisse gezählt, die eindeutig einem Streifen zugeordnet werden können. Dies ermöglichte eine eindeutige Zuordnung der Ursprünge der Counts. Dadurch konnten verschiedene Cuts auf die Daten angewendet werden. Das Verhältnis zwischen Untergrund und Peak konnte deutlich verbessert werden. Über eine Projektion der Daten auf die X-Achse konnte der Untergrund mit einem eindimensionalen fit beschrieben werden. Die durch die Einschränkung veränderte Anzahl an Ereignissen konnte im Anschluss durch eine Effizienzkorrektur ausgeglichen werden.

Die Ergebnisse beider Ansätze stimmen innerhalb ihrer Unsicherheiten überein. Der zweite Ansatz führt in der Analyse zu einem besseren Peak zu Untergrund Verhältnis. Aufgrund der daraus resultierenden geringen Unsicherheiten wurden die Ergebnisse des zweiten Ansatzes für die weitere Diskussion ausgewählt

Die Wirkungsquerschnitte für ^{118}Te(p,γ) und ^{124}Xe(p,γ) wurden mit den theoretischen Vorhersagen zweier Datenbanken verglichen. Zum einen die Ergebnisse, die durch die theoretischen Modelle von NON-SMOKER erzeugt werden [51, 52]. Zum anderen mit den Vorhersagen von TALYS [53]. Die beiden theoretischen Vorhersagen unterscheiden sich voneinander, aufgrund der verschiedenen Modelle, die implementiert wurden um die Eigenschaften der Kerne zu beschreiben. Die Wirkungsquerschnitte für die Reaktion ^{118}Te(p,γ) folgen dem Verlauf theoretis-

cher Vorhersagen von NON-SMOKER. Von den Vorhersagen von TALYS weichen sie ab. Die Wirkungsquerschnitte für ^{124}Xe(p,γ) hingegen zeigen Abweichungen von beiden Modellen. Besonders der Wirkungsquerschnitt bei 8 MeV/u, der in einem vorherigen Experiment gemessen wurde zeigt starke Abweichungen [65].

Mit Hilfe von TALYS konnten die zugrunde liegenden kernphysikalischen Modelle angepasst werden, um eine Vorhersage zu finden, die die experimentellen Werte reproduziert. Für die ^{124}Xe(p,γ) Wirkungsquerschnitte wurden dabei andere Parameter verwendet, als für die ^{118}Te(p,γ) Wirkungsquerschnitte. Die Standardparameter für diese Modelle beschreiben die Wirkungsquerschnitte für diese Kerne innerhalb von 30% Wenn man die Modelle individuel anpasst kann man eine Beschreibung machen, die besser als 10% Prozent ist. Innerhalb dieser Arbeit wurde kein Modell gefunden, dass beide Kerne innerhalb von 10% beschreibt. Für die Untersuchung des Einflusses der neuen Ergebnisse auf die Nukleosynthese Netzwerke, wurden beide Ansätze überprüft.

Auf Grundlage dieser Vorhersagen konnten mit TALYS ebenfalls die astrophysikalischen Reaktionsraten bestimmt werden, um den Einfluss der Messung im Rahmen von post processing Nucleosynthese (PPN) Simulationen zu analysieren. Die PPN Simulationen wurden im Rahmen der NuGrid (Nucleosynthesis Grid) Plattform durchgeführt [3]. Sie wurden für ein Kernkollaps Supernova Model, mit einer Anfangsmasse von 20 Sonnenmassen durchgeführt [54]. Die Simulationen speichern Informationen über den Verlauf von Temperatur, Dichte und Massenanteil der jeweiligen Isotope über die Zeit, in sogenannten Trajektorien.

Im Rahmen dieser Arbeit wurden Trajektorien bei verschiedenen Massenkoordinaten des modelierten Sterns analysiert. Die Massenkoordinaten wurden dabei danach ausgesucht, wo am meisten ^{124}Xe oder ^{118}Te produziert wird. Die hierbei bestimmte maximale Temperatur bestimmte dabei auch die Wahl der Temperatur, für die das Gamow Fenster angegeben wurde. Über die erzeugten Massenflussprofile in der Region um ^{124}Xe und ^{118}Te konnte bestätigt werden, dass der Hauptprozess für die Zerstörung von ^{125}Cs der zeitinvertierte (γ,p) Prozess ist. Ebenso gilt dies für ^{119}I. Es wurde daher der Verlauf des Massenanteils der beiden Reaktionsprodukte aus den gemessenen Reaktionsprodukten angeschaut. Dieser Verlauf wurde verglichen mit dem Verlauf, wenn die neu bestimmten Reaktionsraten implementiert wurden.

Für die einzelnen Isotope ist ein leichter Einfluss auf die Produktion erkennbar. Im Vergleich der Massenanteile zwischen dem implementierten Model und den veränderten Reaktionsraten lassen sich aber außerhalb eines schmalen Massebereichs keine Einflüsse erkennen.

Es wäre interessant weitere Reaktionen zu messen, für die ein großer Einfluss auf die Nukleosynthese Netzwerke erwartet wird.

Die Ergebnisse dieser Arbeit geben Motivation für weitere Experimente mit radioaktiven Isotopen an Speicheringen, deren Reaktionen noch größere Unsicherheiten aufweisen. Es konnten erfolgreich Wirkungsquerschnitte bei astrophysikalisch relevanten Energien bestimmt werden.

Appendix A

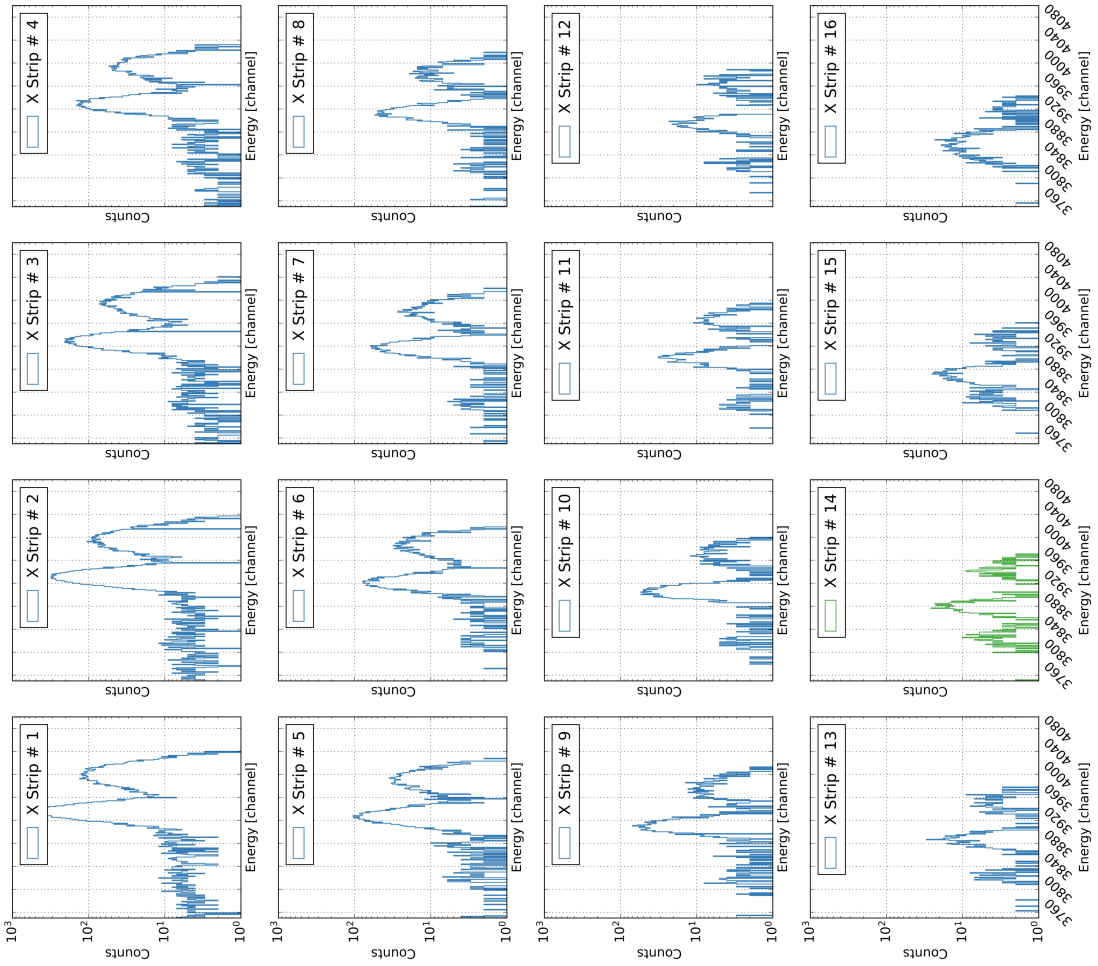

Figure 7.1: Spectra of the 16 x strips of the DSSSD for the recorded xenon data. Strip number 14, marked in green shows the three distinct peaks.

8 Bibliography

[1] J. Eichler and T. Stöhlker, "Radiative electron capture in relativistic ion–atom collisions and the photoelectric effect in hydrogen-like high-z systems," *Physics Reports*, vol. 439, no. 1, pp. 1–99, 2007.

[2] J. Glorius, C. Langer, Z. Slavkovská, L. Bott, C. Brandau, B. Brückner, K. Blaum, X. Chen, S. Dababneh, T. Davinson, P. Erbacher, S. Fiebiger, T. Gaßner, K. Göbel, M. Groothuis, A. Gumberidze, G. Gyürky, M. Heil, R. Hess, R. Hensch, P. Hillmann, P. M. Hillenbrand, O. Hinrichs, B. Jurado, T. Kausch, A. Khodaparast, T. Kisselbach, N. Klapper, C. Kozhuharov, D. Kurtulgil, G. Lane, C. Lederer-Woods, M. Lestinsky, S. Litvinov, Y. A. Litvinov, B. Löher, F. Nolden, N. Petridis, U. Popp, T. Rauscher, M. Reed, R. Reifarth, M. S. Sanjari, D. Savran, H. Simon, U. Spillmann, M. Steck, T. Stöhlker, J. Stumm, A. Surzhykov, T. Szücs, T. T. Nguyen, A. Taremi Zadeh, B. Thomas, S. Y. Torilov, H. Törnqvist, M. Träger, C. Trageser, S. Trotsenko, L. Varga, M. Volknandt, H. Weick, M. Weigand, C. Wolf, P. J. Woods, and Y. M. Xing, "Approaching the Gamow Window with Stored Ions: Direct Measurement of ^{124}Xe (p ,γ) in the ESR Storage Ring," *Phys. Rev. Lett.*, vol. 122, p. 092701, Mar. 2019.

[3] M. Pignatari and F. Herwig, "The nugrid research platform: A comprehensive simulation approach for nuclear astrophysics," *Nuclear Physics News*, vol. 22, no. 4, pp. 18–23, 2012.

[4] K. Lodders, "Abundances and Condensation Temperatures of the Elements," *Meteoritics and Planetary Science Supplement*, vol. 38, p. 5272, July 2003.

[5] E. Anders and N. Grevesse, "Abundances of the elements: Meteoritic and solar," *Geochimica et Cosmochimica Acta*, vol. 53, no. 1, pp. 197–214, 1989.

[6] E. M. Burbidge, G. R. Burbidge, W. A. Fowler, and F. Hoyle, "Synthesis of the elements in stars," *Rev. Mod. Phys.*, vol. 29, pp. 547–650, Oct 1957.

[7] F.-K. Thielemann, C. Fröhlich, R. Hirschi, M. Liebendörfer, I. Dillmann, D. Mocelj, T. Rauscher, G. Martinez-Pinedo, K. Langanke, K. Farouqi, K.-L. Kratz, B. Pfeiffer, I. Panov, D. K. Nadyozhin, S. Blinnikov, E. Bravo, W. R. Hix, P. Höflich, and N. T. Zinner, "Production of intermediate-mass and heavy nuclei," *Progress in Particle and Nuclear Physics*, vol. 59, pp. 74–93, July 2007.

[8] M. Pignatari, K. Göbel, R. Reifarth, and C. Travaglio, "The production of proton-rich isotopes beyond iron: The γ-process in stars," *International Journal of Modern Physics E*, vol. 25, no. 4, p. 1630003, 2016.

[9] P. J. E. Peebles, "Primordial Helium Abundance and the Primordial Fireball. II," *Astrophysical Journal*, vol. 146, p. 542, Nov. 1966.

[10] R. V. Wagoner, W. A. Fowler, and F. Hoyle, "On the Synthesis of Elements at Very High Temperatures," *Astrophysical Journal*, vol. 148, p. 3, Apr. 1967.

[11] E. W. Kolb and M. S. Turner, *The Early Universe*, vol. 69. 1990.

[12] G. Wallerstein, I. Iben Jr., P. Parker, A. Boesgaard, G. Hale, A. Champagne, C. Barnes, F. Käppeler, V. Smith, C. Sneden, R. Boyd, B. Meyer, and D. Lambert, "Synthesis of the elements in stars: forty years of progress," *Rev. Mod. Phys.*, vol. 69, pp. 995 – 1084, 1997.

[13] F. Käppeler, R. Gallino, S. Bisterzo, and W. Aoki, "The s process: Nuclear physics, stellar models, and observations," *Reviews of Modern Physics*, vol. 83, pp. 157–194, Jan. 2011.

[14] J. Cowan, F.-K. Thielemann, and J. Truran, "r-process," *Phys. Rep.*, vol. 208, p. 267, 1991.

[15] A. Cameron, "Stellar evolution,nuclear astrophysics, and nucleogenesis, chalk river report crl–41," tech. rep., A.E.C.L. Chalk River, Canada, 1957.

[16] P. Seeger, W. Fowler, and D. Clayton, "Nucleosynthesis of heavy elements by neutron capture.," *The Astrophysical Journal Supplement Series*, vol. 11, p. 121, 01 1965.

[17] Y.-Z. Qian, W. Haxton, K. Langanke, and P. Vogel, "Neutrino-induced neutron spallation and supernova r-process nucleosynthesis," *Phys. Rev. C*, vol. 55, pp. 1532 – 1544, 1997.

[18] M. Arnould, S. Goriely, and M. Rayet, "The p-process in type ii supernovae," in *Nuclear Astrophysics* (M. Buballa, W. Nörenberg, J. Wambach, and A. Wirzba, eds.), (Darmstadt), pp. 279 – 287, GSI, 1998.

[19] M. Arnould and S. Goriely, "The p-process of stellar nucleosynthesis: astrophysics and nuclear physics status," *Physics Reports*, vol. 384, pp. 1–84, 2003.

[20] C. Travaglio, F. K. Röpke, R. Gallino, and W. Hillebrandt, "Type Ia Supernovae as Sites of the p-process: Two-dimensional Models Coupled to Nucleosynthesis," *Astrophysical Journal*, vol. 739, p. 93, Oct. 2011.

[21] C. Travaglio, T. Rauscher, A. Heger, M. Pignatari, and C. West, "Role of Core-collapse Supernovae in Explaining Solar System Abundances of p Nuclides," *Astrophysical Journal*, vol. 854, p. 18, Feb. 2018.

[22] S. Woosley and W. Howard, "p-process," *Astrophysical Journal Suppl.*, vol. 36, p. 285, 1978.

[23] H. Schatz and K. E. Rehm, "X-ray binaries," *Nuclear Physics A*, vol. 777, pp. 601–622, Oct. 2006.

[24] K. Göbel, J. Glorius, A. Koloczek, M. Pignatari, R. Reifarth, R. Schach, and K. Sonnabend, "Nucleosynthesis simulations for the production of the p-nuclei ^{92}Mo and ^{94}Mo in a Supernova type II model," *EPJ Web of Conferences*, vol. 93, p. 03006, 2015.

[25] C. E. Rolfs, *Cauldrons in the cosmos*. University of Chicago Press, 1988.

[26] J. Glorius, Y. A. Litvinov, M. Aliotta, F. Amjad, B. Brückner, C. Bruno, R. Chen, T. Davinson, S. Dellmann, T. Dickel, I. Dillmann, P. Erbacher, O. Forstner, H. Geissel, C. Griffin, R. Grisenti, A. Gumberidze, E. Haettner, R. Hess, P.-M. Hillenbrand, C. Hornung, R. Joseph, B. Jurado, E. Kazanseva, R. Knöbel, D. Kostyleva, C. Kozhuharov, N. Kuzminchuk, C. Langer, G. Leckenby, C. Lederer-Woods, M. Lestinsky, S. Litvinov, B. Löher, B. Lorenz, E. Lorenz, J. Marsh, E. Menz, T. Morgenroth, I. Mukha, N. Petridis, U. Popp, A. Psaltis, S. Purushothaman, R. Reifarth, E. Rocco, P. Roy, M. Sanjari, C. Scheidenberger, M. Sguazzin, R. Sidhu, U. Spillmann, M. Steck, T. Stöhlker, J. Swartz, Y. Tanaka, H. Törnqvist, L. Varga, D. Vescovi, H. Weick, M. Weigand, P. Woods, T. Yamaguchi, and J. Zhao, "Storage, accumulation and deceleration of secondary beams for nuclear astrophysics," *Nuclear Instruments and Methods in Physics Research Section B: Beam Interactions with Materials and Atoms*, vol. 541, pp. 190–193, 2023.

[27] H. Geissel, P. Armbruster, K. H. Behr, A. Brünle, K. Burkard, M. Chen, H. Folger, B. Franczak, H. Keller, O. Klepper, B. Langenbeck, F. Nickel, E. Pfeng, M. Pfützner, E. Roeckl, K. Rykaczewski, I. Schall, D. Schardt,

C. Scheidenberger, K.-H. Schmidt, A. Schröter, T. Schwab, K. Sümmerer, M. Weber, G. Münzenberg, T. Brohm, H.-G. Clerc, M. Fauerbach, J.-J. Gaimard, A. Grewe, E. Hanelt, B. Knödler, M. Steiner, B. Voss, J. Weckenmann, C. Ziegler, A. Magel, H. Wollnik, J. P. Dufour, Y. Fujita, D. J. Vieira, and B. Sherrill, "The GSI projectile fragment separator (FRS): a versatile magnetic system for relativistic heavy ions," *Nuclear Instruments and Methods in Physics Research B*, vol. 70, pp. 286–297, 1992.

[28] B. Franzke, "The heavy ion storage and cooler ring project ESR at GSI," *Nucl. Instr. Meth. B*, vol. 24/25, pp. 18–22, 1987.

[29] A. online at, "https://www.gsi.de/en/researchaccelerators/accelerator_facility /ion_sources/starting_point_of_the_gsi_accelerator_facility_ion_sources." [Accessed: 3.10.2023].

[30] A. online at, "https://www.gsi.de/en/researchaccelerators/accelerator_facility /linear_accelerator." [Accessed: 3.10.2023].

[31] A. online at, "https://www.gsi.de/en/researchaccelerators/accelerator_facility /ring_accelerator." [Accessed: 3.10.2023].

[32] A. online at, ""https://www.gsi.de/en/researchaccelerators/accelerator_facility /fragment_separator"." [Accessed: 3.10.2023].

[33] A. online at, "https://www.gsi.de/forschungbeschleuniger /beschleunigeranlage." [Accessed: 3.10.2023].

[34] F. Nolden, K. Beckert, F. Caspers, B. Franczak, B. Franzke, R. Menges, A. Schwinn, and M. Steck, "Stochastic cooling at the ESR," *Nuclear Instruments and Methods in Physics Research Section A: Accelerators, Spectrometers, Detectors and Associated Equipment*, vol. 441, pp. 219–222, feb 2000.

[35] M. Steck and Y. A. Litvinov, "Heavy-ion storage rings and their use in precision experiments with highly charged ions," *Progress in Particle and Nuclear Physics*, vol. 115, p. 103811, 2020.

[36] I. Meshkov, "Electron cooling — recent developments and trends," *Nuclear Physics A*, vol. 626, pp. 459–471, nov 1997.

[37] L. Varga. PhD thesis, University of Heidelberg, 2021.

[38] H. Kolanoski and N. Wermes, *8 Halbleiterdetektoren*, pp. 269–383. Berlin, Heidelberg: Springer Berlin Heidelberg, 2016.

[39] A. N. Artemyev, A. Surzhykov, S. Fritzsche, B. Najjari, and A. B. Voitkiv, "Target effects on the linear polarization of photons emitted in radiative electron capture by heavy ions," *Phys. Rev. A*, vol. 82, p. 022716, Aug. 2010.

[40] C. Brandau, *Messungen zur Photorekombination hochgeladener lithium aehnlicher Ionen*. PhD thesis, Justus-Liebig-Universitaet, Otto-Behaghel-Str. 8, 35394 Giessen, 2000.

[41] G. Audi, M. Wang, A. Wapstra, F. Kondev, M. MacCormick, X. Xu, and B. Pfeiffer, "The ame2012 atomic mass evaluation," *Chinese Physics C*, vol. 36, pp. 1287–1602, dec 2012.

[42] A. Surzhykov. personal communication.

[43] J. Glorius. personal communication, November 2023.

[44] B. Mei, T. Aumann, S. Bishop, K. Blaum, K. Boretzky, F. Bosch, C. Brandau, H. Bräuning, T. Davinson, I. Dillmann, C. Dimopoulou, O. Ershova, Z. Fülöp, H. Geissel, J. Glorius, G. Gyürky, M. Heil, F. Käppeler, A. Kelic-Heil, C. Kozhuharov, C. Langer, T. Le Bleis, Y. Litvinov, G. Lotay, J. Marganiec, G. Münzenberg, F. Nolden, N. Petridis, R. Plag, U. Popp, G. Rastrepina, R. Reifarth, B. Riese, C. Rigollet, C. Scheidenberger, H. Simon, K. Sonnabend, M. Steck, T. Stöhlker, T. Szücs, K. Sümmerer, G. Weber, H. Weick, D. Winters, N. Winters, P. Woods, and Q. Zhong, "First measurement of the $^{96}\mathrm{Ru}(p,\gamma)^{97}\mathrm{Rh}$ cross section for the p process with a storage ring," *Phys. Rev. C*, vol. 92, p. 035803, 2015.

[45] S. Slavkovska. PhD thesis, Johann Wolfgang Goethe University Frankfurt, 2020.

[46] Y. M. Xing, J. Glorius, L. Varga, L. Bott, C. Brandau, B. Brückner, R. J. Chen, X. Chen, S. Dababneh, T. Davinson, P. Erbacher, S. Fiebiger, T. Gaßner, K. Göbel, M. Groothuis, A. Gumberidze, G. Gyürky, M. Heil, R. Hess, R. Hensch, P. Hillmann, P. M. Hillenbrand, O. Hinrichs, B. Jurado, T. Kausch, A. Khodaparast, T. Kisselbach, N. Klapper, C. Kozhuharov, D. Kurtulgil, G. Lane, C. Langer, C. Lederer-Woods, M. Lestinsky, S. Litvinov, Y. A. Litvinov, B. Löher, N. Petridis, U. Popp, M. Reed, R. Reifarth, M. S. Sanjari, H. Simon, Z. Slavkovská, U. Spillmann, M. Steck, T. Stöhlker, J. Stumm, T. Szücs, T. T. Nguyen, A. T. Zadeh, B. Thomas, S. Y. Torilov, H. Törnqvist, C. Trageser, S. Trotsenko, M. Volknandt, M. Wang, M. Weigand, C. Wolf, P. J. Woods, Y. H. Zhang, and X. H. Zhou, "Determination of luminosity for in-ring reactions: A new approach for the low-energy

domain," *Nuclear Instruments and Methods in Physics Research A*, vol. 982, p. 164367, Dec. 2020.

[47] M. Mazzocco, D. Ackermann, M. Block, H. Geissel, F. P. Heßberger, S. Hofmann, N. Iwasa, K. Nishio, W. R. Plaß, C. Scheidenberger, H. Weick, and M. Winkler, "Extension of the monte-carlo code MOCADI to fusion-evaporation reactions," *The European Physical Journal Special Topics*, vol. 150, pp. 363–364, nov 2007.

[48] "Mocadi 4.2." `http://web-docs.gsi.de/~weick/mocadi/mocadi-manual.html`. [Accessed: 11.08.2023].

[49] M. Reese, J. Gerl, P. Golubev, and N. Pietralla, "Automatic intrinsic calibration of double-sided silicon strip detectors," *Nuclear Instruments and Methods in Physics Research Section A: Accelerators, Spectrometers, Detectors and Associated Equipment*, vol. 779, pp. 63–68, 2015.

[50] A. online at, "https://www.gsi.de/work/beschleunigerbetrieb/beschleuniger/esr/esr_maschine/mas
[Accessed: 29.11.2023].

[51] T. Rauscher and F.-K. Thielemann, "Astrophysical Reaction Rates From Statistical Model Calculations," *Atomic Data Nucl. Data Tables*, vol. 75, p. 1, 2000.

[52] T. Rauscher and F.-K. Thielemann, "Tables of nuclear cross sections and reaction rates: An addendum to the paper :astrophysical reaction rates from statistical model calculations," *Atomic Data Nucl. Data Tables*, vol. 79, p. 47, 2001.

[53] A. J. Koning, S. Hilaire, and M. C. Duijvestijn, "Talys-1.0," in *ND2007*, EDP Sciences, 2007.

[54] C. Ritter, F. Herwig, S. Jones, M. Pignatari, C. Fryer, and R. Hirschi, "Nugrid stellar data set. ii. stellar yields from h to bi for stellar models with mzams = 1 to 25msun and z = 0.0001 to 0.02," 2017.

[55] R. H. Cyburt, A. M. Amthor, R. Ferguson, Z. Meisel, K. Smith, S. Warren, A. Heger, R. D. Hoffman, T. Rauscher, A. Sakharuk, H. Schatz, F. K. Thielemann, and M. Wiescher, "The jina reaclib database: Its recent updates and impact on type-i x-ray bursts," *The Astrophysical Journal Supplement Series*, vol. 189, pp. 240–252, June 2010.

[56] L. Roberti. ,personal communication, May 2023.

[57] W. Rapp, J. Gorres, M. Wiescher, H. Schatz, and F. Kappeler, "Sensitivity of p-process nucleosynthesis to nuclear reaction rates in a 25m$_\odot$supernova model," *The Astrophysical Journal*, vol. 653, pp. 474–489, Dec. 2006.

[58] K. Göbel, J. Glorius, A. Koloczek, M. Pignatari, R. Reifarth, R. Schach, and K. Sonnabend, "Nucleosynthesis simulations for the production of the p-nuclei92mo and94mo in a supernova type ii model," *EPJ Web of Conferences*, vol. 93, p. 03006, 2015.

[59] A. Gilbert and A. Cameron *Can. J. Phys.*, vol. 43, p. 1446, 1965.

[60] S. Hilaire, M. Girod, S. Goriely, and A. J. Koning, "Temperature-dependent combinatorial level densities with the d1m gogny force," *Physical Review C*, vol. 86, p. 064317, Dec. 2012.

[61] I. Daoutidis and S. Goriely, "Large-scale continuum random-phase approximation predictions of dipole strength for astrophysical applications," *Physical Review C*, vol. 86, p. 034328, Sept. 2012.

[62] J. Glorius, C. Berthelot, K. Blaum, C. Brandau, C. Bruno, X. Chen, T. Davinson, S. F. Dellmann, I. Dillmann, P. Erbacher, D. Freire Fernandez, C. J. Griffin, A. Gumberidze, M. Heil, R. Hess, P. M. Hillenbrand, B. Jurado, C. Langer, G. Leckenby, M. Lestinsky, S. Litvinov, Y. A. Litvinov, B. A. Lorentz, M. Lugaro, B. Löher, J. Marsh, N. Petridis, J. Pibernat, M. Pignatari, R. Reifarth, M. S. Sanjari, M. Sguazzin, R. S. Sidhu, H. Simon, U. Spillmann, M. Steck, T. Stöhlker, J. A. Swartz, H. Törnqvist, and P. J. Woods, "Proton-capture on ^{91}nb - a key to the explosive nucleosynthesis of the p nuclei," 2022. GSI Research Proposal.

[63] M. Lestinsky, V. Andrianov, B. Aurand, V. Bagnoud, D. Bernhardt, H. Beyer, S. Bishop, K. Blaum, A. Bleile, A. Borovik, F. Bosch, C. Bostock, C. Brandau, A. Bräuning-Demian, I. Bray, T. Davinson, B. Ebinger, A. Echler, P. Egelhof, A. Ehresmann, M. Engström, C. Enss, N. Ferreira, D. Fischer, A. Fleischmann, E. Förster, S. Fritzsche, R. Geithner, S. Geyer, J. Glorius, K. Göbel, O. Gorda, J. Goullon, P. Grabitz, R. Grisenti, A. Gumberidze, S. Hagmann, M. Heil, A. Heinz, F. Herfurth, R. Heß, P.-M. Hillenbrand, R. Hubele, P. Indelicato, A. Källberg, O. Kester, O. Kiselev, A. Knie, C. Kozhuharov, S. Kraft-Bermuth, T. Kühl, G. Lane, Y. Litvinov, D. Liesen, X. Ma, R. Märtin, R. Moshammer, A. Müller, S. Namba, P. Neumeyer, T. Nilsson, W. Nörtershäuser, G. Paulus, N. Petridis, M. Reed, R. Reifarth, P. Reiß, J. Rothhardt, R. Sanchez, M. Sanjari, S. Schippers, H. Schmidt, D. Schneider, P. Scholz, R. Schuch, M. Schulz, V. Shabaev, A. Simonsson, J. Sjöholm, Ö. Skeppstedt, K. Sonnabend, U. Spillmann,

K. Stiebing, M. Steck, T. Stöhlker, A. Surzhykov, S. Torilov, E. Träbert, M. Trassinelli, S. Trotsenko, X. Tu, I. Uschmann, P. Walker, G. Weber, D. Winters, P. Woods, H. Zhao, and Y. Zhang, "Physics book: Cryring@esr," *The European Physical Journal Special Topics*, vol. 225, no. 5, pp. 797–882, 2016.

[64] M. Lestinsky, A. Bräuning-Demian, H. Danared, M. Engström, W. Enders, S. Fedotova, B. Franzke, A. Heinz, F. Herfurth, A. Källberg, O. Kester, Y. Litvinov, M. Steck, D. Reistad, A. Simonsson, O. Skeppstedt, T. Stöhlker, and G. Vorobjev, "Cryring@esr: present status and future research," *Physica Scripta*, vol. T166, p. 014075, Nov. 2015.

[65] J. Glorius, C. Langer, Z. Slavkovská, L. Bott, C. Brandau, B. Brückner, K. Blaum, X. Chen, S. Dababneh, T. Davinson, P. Erbacher, S. Fiebiger, T. Gaßner, K. Göbel, M. Groothuis, A. Gumberidze, G. Gyürky, M. Heil, R. Hess, R. Hensch, P. Hillmann, P.-M. Hillenbrand, O. Hinrichs, B. Jurado, T. Kausch, A. Khodaparast, T. Kisselbach, N. Klapper, C. Kozhuharov, D. Kurtulgil, G. Lane, C. Lederer-Woods, M. Lestinsky, S. Litvinov, Y. A. Litvinov, B. Löher, F. Nolden, N. Petridis, U. Popp, T. Rauscher, M. Reed, R. Reifarth, M. S. Sanjari, D. Savran, H. Simon, U. Spillmann, M. Steck, T. Stöhlker, J. Stumm, A. Surzhykov, T. Szücs, T. T. Nguyen, A. Taremi Zadeh, B. Thomas, S. Y. Torilov, H. Törnqvist, M. Träger, C. Trageser, S. Trotsenko, L. Varga, M. Volknandt, H. Weick, M. Weigand, C. Wolf, P. J. Woods, and Y. M. Xing, "Approaching the gamow window with stored ions: Direct measurement of ^{124}xe(p,γ) in the esr storage ring," *Phys. Rev. Lett.*, vol. 122, p. 092701, Mar 2019.

List of Figures

List of Tables